# Investigating Future Changes in Southern China Precipitation Characteristics Based on Dynamically Downscaled CMIP5 Climate Projections

**LIU, Ying Lung**

A Thesis Submitted in Partial Fulfilment

of the Requirements for the Degree of

Master of Philosophy

in

Earth and Atmospheric Sciences

The Chinese University of Hong Kong

August 2020

# Thesis Assessment Committee

Professor CHAN, Man Nin (Chair)

Professor TAM, Chi Yung Francis (Thesis Supervisor)

Professor TAI, Pui Kuen Amos (Committee Member)

Doctor CHEUNG, Kei Wai Kevin (External Examiner)

Abstract of thesis entitled:

**Investigating Future Changes in Southern China Precipitation Characteristics Based on Dynamically Downscaled CMIP5 Climate Projections**

Submitted by **LIU, Ying Lung**

for the Degree of **Master of Philosophy in Earth and Atmospheric Sciences**

at The Chinese University of Hong Kong in **August 2020**

# Abstract

In this study, atmosphere-ocean coupled general circulation model (GCM) products were dynamically downscaled using the Regional Climate Model system version 4 (RegCM4), in order to study changes in the hydrological cycle - including extreme events - due to a warmer climate by the end of the 21$^{st}$ century over Southern China. The performance of 22 GCMs participating in the Coupled Model Intercomparison Project Phase 5 (CMIP5) in simulating the climate over the East Asian- western north Pacific region was first evaluated. It was found that MPI-ESM-MR, CNRM-CM5, ACCESS1-3, and GFDL-CM3 can reasonably reproduce the seasonal mean atmospheric circulation in that region, as well as its interannual variability. Outputs from these GCMs were subsequently downscaled, using the RegCM4, to a horizontal resolution of 25 km × 25km, for the period of 1979 to 2003, and also from 2050 to 2099, with the latter based on GCM projections according to the RCP8.5 scenario.

Results show that the whole domain would undergo warming in the lower troposphere by 3 – 4 °C over inland China and by ~2 °C over the ocean and low-latitude locations. Compared to the 1979-2003 era, during 2050-2099 boreal summer, the mean precipitation is projected to increase by 0.5 – 1.5 mm/day over coastal Southern China. The interannual variability of precipitation is also significantly enhanced in the same season. In boreal

spring, similar increases in both the seasonal mean and also its year-to-year variation are also found, over more inland locations north of 25°N. Extreme daily precipitation is projected to become more intense, based on analyses of the 95th percentile for these seasons. On the other hand, it will be significantly drier during autumn over a broad area in Southern China: the mean rainfall is projected to decrease by 15 – 20%. In addition, changes in the annual number of maximum consecutive dry days (CDD) was found to increase by ~3 – 5 days over locations south of 32°N as well. This implies that the dry season will be lengthened in the region. The potential impact of global warming on sub-daily rainfall was also examined. For the rainfall diurnal cycle (DC), there is no significant change in both its spatial and temporal patterns.

Moisture budget analyses were also carried out, in order to ascertain the importance of changes in background moisture, versus those in wind circulation, on the intensification of MAM and JJA mean rainfall and their variability. Results suggest that the alteration of mean precipitation is consistent with changes in vertically integrated moisture flux convergence. The decomposition of vertically integrated moisture flux convergence shows that changes in mean background humidity (anomalous wind convergence) is responsible for the increase in the interannual precipitation variability in MAM (JJA). Changes in large-scale background circulation during SON, based on the parent GCM results, were examined. Results indicate that strengthened northerlies induced by an anomalous low-level cyclone over East Asia and the western North Pacific are responsible for the drier SON in Southern China.

# 摘要

本研究使用 RegCM4 將全球氣候模型（GCM）動力降尺度，以研究在全球暖化下二十一世紀末華南地區水文循環及相關極端天氣事件的變化。研究首先評核 22 個參與 CMIP5 的 GCM 對東亞—西太平洋地區氣候的模擬表現，當中 MPI-ESM-MR、CNRM-CM5、ACCESS1-3 及 GFDL-CM3 在模擬該區的季節平均大氣循環及年際變異度的表現良好。隨後，這四個 GCM 的氣候模擬結果經由 RegCM4 降尺度，以 25 公里×25 公里的水平解析度進行在 1997 – 2003 年，及在 RCP8.5 情境下 2050 – 2099 年氣候推估的兩組積分。

模擬結果顯示整個研究區域的低層對流層將會變暖，中國內陸的溫度會上升 3 – 4°C，而海洋及低緯度地區則會上升大約 2°C。相較 1979 – 2003 年間，預計華南沿岸地區的夏季日平均雨量會在 2050 – 2099 年間上升 0.5 – 1.5 毫米，同時夏季雨量的年際異變度也會變得更為劇烈。在北半球春季，北緯 25°以北較為內陸的地區，季平均雨量及其年際變異度亦有類似變化。分析日雨量的第 95 個百分位顯示這兩季的極端降雨也預計將會加劇。另一方面，秋季的氣候會變得更加乾旱，平均雨量將會下降 15 – 20%。此外，分析全年最長乾期日數的變化後，發現較北緯 32°以南的地區乾期將會延長約 3 – 5 日，代表該區的乾季將會變長。而全球暖化對日以下尺度的降雨的潛在影響經過分析後，顯示降雨的晝夜循環在時間、空間上並沒有明顯轉變。

本研究亦有分析水汽收支，比較背景水汽和大氣環流變化對春夏平均雨量及其年際變異度的重要程度。分析結果指出垂直積分水汽通量幅合是造成季平均雨量改變的主因。在拆解其年際變異度後，發現平均背景濕度（風場幅合異常）的改變，是讓春季（夏季）雨量的年際變異率上升的成因。同時，我們亦檢視過 GCM 中大尺度背景大氣循環在秋季的轉變，發現在東亞及西北太平洋低層的異常氣旋引發了該區更強的北風，導致華南秋季變得更加乾旱。

# Acknowledgment

I would like to express my sincere gratefulness to my thesis supervisor, Professor Francis Tam. He was also my academic advisor and teacher who introduced me to atmospheric sciences during my undergraduate study in CUHK. Under his supervision, I learned a lot of research skills and felt supported in handling scientific research myself for the first time. His skillful and patient guidance has helped me greatly in tackling different problems in these two years. Without his enlightenment, I would not even pursue my passion for atmospheric sciences.

I appreciate the cooperative support from the Hong Kong Observatory, especially Mr. Lee Sai Ming, for sharing CMIP5 model results and discussing the research plan with us as well. Suggestion from Mr. Wong Hong Wai and Mr. Tang Shu Yan is very helpful in the installation and modification of RegCM4. Mr. Lui Yuk Sing also gave me useful advice in handling climate models. Their support speeded up my research effectively.

I am grateful to Professor Chan, Professor Tai, and Doctor Cheung who spent their pleasant time to review my thesis. Lastly, I would like to thank all staff in Earth and Atmospheric Science Programme in CUHK and members in Professor Tam's and Professor Tai's research groups. Their assistance allows me to get through different unexpected events in these two years.

## Table of Contents

**Abstract** ..... **i**

**摘要** ..... **iii**

**Acknowledgment** ..... **iv**

**List of Figures** ..... **viii**

**List of Tables** ..... **xvi**

**1 Introduction** ..... **1**

1.1 Mean climate of Southern China and its variability ..... 1

1.2 Precipitation variability in Southern China ..... 2

1.3 Precipitation characteristics in Southern China under the warming climate ..... 8

1.4 Climate model and dynamical downscaling ..... 11

1.5 Research objectives and thesis outline ..... 15

**2 Data and Methodology** ..... **17**

2.1 CMIP5 GCM selection ..... 17

2.1.1 Summer and winter monsoon ..... 20

2.1.2 Summer and winter temperature ..... 22

2.1.3 Summer precipitation ..... 23

2.1.4 ENSO variability ..... 25

2.1.5 Summer monsoon variability ..... 27

2.1.6 Winter monsoon variability ..... 29

2.1.7 Selection results ..... 30

2.2 Regional climate model configuration ..... 31

2.3 Experiment design ..... 32

2.4 Moisture budget analysis ..... 33

**3 Performance of RegCM4 and Dynamical Downscaling** ..... **36**

3.1 RegCM4 performance ..... 36

3.1.2 Precipitation ..... 38

3.1.3 Maximum consecutive dry days ..... 40

3.1.4 Diurnal rainfall ..... 41
3.2 Performance of dynamical downscaling using RegCM4 ..... 43
3.2.1 Low-level temperature and wind ..... 43
3.2.2 Precipitation ..... 49
3.2.3 Summarized dynamical downscaling results ..... 53
**4 Seasonal Mean Climate Projection ..... 55**
4.1 Changes in mean state climate ..... 55
4.2 Moisture budget analysis on seasonal mean state precipitation change ..... 58
4.4 Changes in dry season ..... 59
4.4.1 Maximum consecutive dry days ..... 59
4.4.2 Circulation changes associated with drier SON ..... 62
**5 Interannual Variability of Seasonal Precipitation ..... 65**
**6 Daily to Sub-daily Precipitation ..... 74**
6.1 Daily precipitation ..... 74
6.1.1 Daily precipitation probability density functions ..... 74
6.1.2 Daily precipitation extreme ..... 76
6.2 Sub-daily precipitation ..... 82
6.2.1 Summertime diurnal rainfall cycle ..... 82
6.2.2 3-hourly Precipitation Probability Density Functions ..... 87
**7 Discussions and Conclusion ..... 89**
7.1 Discussions ..... 89
7.1.1 Review of GCM selection and dynamical downscaling ..... 89
7.1.2 Changes in precipitation characteristics in SON ..... 92
7.1.3 Issues related to precipitation extremes ..... 92
7.1.4 Future investigations with improved models ..... 95
7.2 Conclusion ..... 96
**Appendix ..... 99**
1 CMIP5 model selection details ..... 99

1.1 Summer mean precipitation ..... 99
1.2 ENSO-related variability (DJF) ..... 100
1.3 ENSO-related variability (MAM) ..... 101
1.4 East Asian summer monsoon variability ..... 102
1.5 East Asian winter monsoon variability ..... 103
2 Results of simulated variables in multi-model ensemble averages ..... 105
2.1 Mean 850hPa temperature and wind ..... 105
2.2 Mean precipitation, evaporation and vertically integrated moisture flux convergence ..... 106
3 Consecutive dry days in GCMs ..... 111
4 Calculation of vertically integrated moisture flux convergence for interannual precipitation variability ..... 113
**Bibliography ..... 115**

# List of Figures

**Figure 1.1** Surface elevation (unit: m) within domain of interest (1°S – 40°N, 105 – 135°E). ..... 2

**Figure 1.2** (left) June-to-August (JJA) and (right) December-to-February (DJF) 925hPa geopotential height (shading, units: m) and wind (arrows, units: $ms^{-1}$) from the ERA-Interim Reanalysis dataset (1979 – 2005). ..... 3

**Figure 1.3** Monthly averaged (left, blue bars) precipitation from APHRODITE (1979 – 2003), (left, red line) 1000hPa temperature and (right, southerly as positive) meridional wind from the ERA-Interim Reanalysis dataset (1979 – 2003) over the continental area in 20 – 30°N, 110 – 120°E. ..... 4

**Figure 1.4** (Grey) Historical, (light blue) RCP4.5, and (red) RCP8.5 simulated time-series of summer monsoon indices over (a) East Asia, (b) South Asia, (c) western North Pacific, and (d) Australia. Reprinted from the IPCC AR5 WGI Figure 14.5 (Christensen et al. 2013). ..... 9

**Figure 1.5** Schematic depiction of regional climate modeling and application. Reprinted from Giorgi 2019. ..... 14

**Figure 2.1** (left) JJA and (right) DJF mean 850hPa wind (arrows, units: $ms^{-1}$) and 850hPa temperature (shading, units: K) calculated from ERA-interim dataset with the period (1979 – 2005). The red box in both plots indicates the region where the monsoon pattern can be indicated. ..... 21

**Figure 2.2** Taylor diagrams for (left) JJA 850hPa zonal wind and (right) DJF 850hPa meridional wind based on values over the domains outlined in **Figure 2.1**. The angular axis and the radial axis indicate the pattern correlation and the standardized deviation respectively. The distance between a point and REF indicates the root mean square error of the corresponding model. ..... 22

**Figure 2.3** Same as **Figure 2.2**, but for (left) JJA 850hPa temperature and (right) DJF 850hPa temperature over (6°S – 45°N, 100 – 140°E). ..... 23

**Figure 2.4** The JJA mean precipitation (units: mm/day) of the reference data (top-left) and models 1 – 11 in **Table 2.1**. ..... 24

**Figure 2.5** Same as **Figure 2.4** but for models 12 – 23. ..... 25

**Figure 2.6** (left) Regressed DJF 850hPa wind (arrows, unit: $ms^{-1}$) and sea-surface temperature (shading, unit: K) and (right) the regressed 850hPa wind (arrows, unit: $ms^{-1}$) and 850hPa stream function (shading, unit: $m^2s^{-1}$) over the western Pacific and southeastern Asia of the reference data onto the Niño3.4 index. ... 26

**Figure 2.7** Same as **Figure 2.2**, but for (left) DJF and (right) MAM regressed sea-surface temperature on Niño3.4 index over (15°S – 15°N, 150°E – 95°W)..... 27

**Figure 2.8** (left) Regressed 850hPa wind (arrows, unit: $ms^{-1}$) and precipitation (shading, unit: mm/day) and (right) the Taylor diagram of 850hPa zonal wind and precipitation flux over the enclosed region by a red rectangle in (left). ..... 28

**Figure 2.9** (left) DJF 850hPa wind (arrows, unit: $ms^{-1}$) 850hPa temperature (shading, unit: K) regressed on EAWM index and (right) the Taylor diagram of 850hPa regressed meridional wind and temperature over the enclosed region by a red rectangle in (left) (0 – 50°N, 90 – 150°E). ..... 29

**Figure 2.10** Simulated time-series of area-averaged anomalous (a) precipitation, (b) evaporation, (c) vertically integrated moisture flux convergence (below 500hPa) and (d) wind convergence based on CMIP5 models in historical climate (grey), and under climate scenarios RCP2.6 (dark blue), RCP4.5 (light blue), RCP6.0 (orange) and RCP8.5 (red) over monsoon region. Reprinted from the IPCC AR5 WGI Figure 14.2 (Christensen et al. 2013). ..... 35

**Figure 3.1** JJA mean 850hPa wind (arrows, units: $ms^{-1}$) and temperature (shading, units: K) from (left) ERA-interim, (middle) RegCM4_EA and (right) RegCM4_EA

minus ERA-interim during 1979 – 2003 respectively. ..... 36

**Figure 3.2** Same as **Figure 3.1** but for DJF. ..... 37

**Figure 3.3** JJA mean precipitation (units: mm/day) from (left) TRMM 3B42 (1998 – 2018), (middle) APHRODITE (1979 – 2003) and (right) RegCM4_EA. ..... 38

**Figure 3.4** Same as **Figure 3.3** but for DJF. ..... 39

**Figure 3.5** Mean annual maximum consecutive dry days (units: days) for (left) TRMM, (middle) APHRODITE and (right) RegCM4_EA. ..... 41

**Figure 3.6** 3-hourly JJA precipitation deviation from the daily mean (units: mm/day) from TRMM with the period 1998 – 2017. The local time (UTC +8) is indicated at the top-left of each panel.. ..... 42

**Figure 3.7** Same as **Figure 3.6** but for RegCM4_EA. The 3-hourly data is computed by averaging the values from the adjacent two hours of the plotted LT. ..... 43

**Figure 3.8** Taylor diagrams examining the performance of dynamical downscaling for MAM mean 850hPa (green) temperature, meridional component (blue) and zonal component (red) of wind for (left) historical (1979 – 2003) and (right) RCP8.5 (2050 – 2099) simulation. Number on colored circles represents the RegCM4 downscaled products, with 1: ACCESS1-3, 2: CNRM-CM3, 3: GFDL-CM3, and 4: MPI-ESM-MR. REF refers to the corresponding raw GCMs products. See text for details. ..... 44

**Figure 3.9** Same as **Figure 3.8** but for JJA. ..... 45

**Figure 3.10** Same as **Figure 3.8** but for SON. ..... 45

**Figure 3.11** Same as **Figure 3.8** but for DJF. ..... 46

**Figure 3.12** JJA historical mean (1979 – 2003) 850hPa temperature (shading, units: K) and wind (arrows, units: ms-1) from (left panel) RegCM4 downscaling and (right panel) raw GCMs. ..... 46

**Figure 3.13** Same as **Figure 3.10** but for SON. ..... 48

**Figure 3.14** Same as **Figure 3.12** but for MAM precipitation (units: mm/day). ..... 49

**Figure 3.15** Same as **Figure 3.14** but for JJA. ..... 50

**Figure 3.16** Same as **Figure 3.14** but for SON. ..... 51

**Figure 3.17** Same as **Figure 3.14** but for DJF. ..... 52

**Figure 4.1** MME_RCP8.5 minus MME_HIST mean 850hPa temperature (shading, units: K) and wind (arrows, units: $ms^{-1}$) in (a) MAM, (b) JJA, (c) SON, and (d) DJF. RegCM4_GF(RegCM4_AC) is excluded for JJA(SON). ..... 56

**Figure 4.2** Difference of seasonal mean (a, d, g, j) precipitation, (b, e, h, k) evaporation, and (c, f, i, l) vertically integrated moisture flux convergence between MME_HIST and MME_RCP8.5 for (a, b, c) MAM, (d, e, f) JJA, (g, h, i) SON, and (j, k, l) DJF. Only the continental region is plotted. RegCM4_GF(RegCM4_AC) is excluded for JJA(SON). The maps of the variables simulated in two MMEs are included in **Appendix 2.2**. ..... 57

**Figure 4.8** Mean annual maximum consecutive dry days (units: days) for (left) MME_HIST, (middle) MME_RCP8.5, and (right) their difference. ..... 60

**Figure 4.9** Mean start date of the annual maximum consecutive dry days (units: days after 1st September) for (left) MME_HIST, (middle) MME_RCP8.5, and (right) their difference. ..... 61

**Figure 4.10** Same as **Figure 4.9** but for the end date. ..... 62

**Figure 4.11** Percentage changes in vertically averaged relative (shading, units: %) and specific (contours, units: %) humidity between MME_HIST and MME_RCP8.5 in (a) MAM, (b) JJA, (c) SON and (d) DJF. All four downscaled models are included in the MME. ..... 63

**Figure 4.12** Monthly mean precipitation (shading, units: mm/day) and 850hPa wind (arrows, units: ms-1) difference between MME_HIST and MME_RCP8.5 for the period from (a) September to (d) December. ..... 63

**Figure 4.13** Monthly plots of sea-level pressure deviated from area mean (shading, units: hPa) and 850hPa wind (arrows, units: $ms^{-1}$) from the MME of four selected raw GCMs for (left column) historical and (middle column) future simulations and (right column) their difference in (top row) September, (second row) October, (third row) November and (bottom row) December. ..... 64

**Figure 5.1** MME_HIST interannual seasonal precipitation variance (upper, units: $(mm/day)^2$) and the difference from MME_RCP8.5 in (a, e) MAM, (b, f) JJA, (c, g) SON, and (d, h) DJF. RegCM4_GF(RegCM4_AC) is excluded for JJA(SON). ..... 66

**Figure 5.2** Modified moisture budget for interannual variability in MAM, with all units converted into mm/day. The rows are the three terms with (top row) $\overline{|\mathrm{P}'|}$, (middle row) $\overline{\widehat{\mathrm{P}}'\mathrm{E}'}$, and (bottom row) $-\overline{\widehat{\mathrm{P}}'\left(\frac{1}{\mathrm{g}}\nabla\cdot\int_0^{\mathrm{p_s}}\mathrm{qVdp}\right)'}$ respectively. The columns stand for results from (left column) MME_HIST, (middle column) MME_RCP8.5, and (right column) their differences. Please refer to the text for details..... 68

**Figure 5.3** Same as Figure 5.2 but for JJA. RegCM4_GF is excluded. ..... 69

**Figure 5.4** Decomposed $-\overline{\widehat{P}'\left(\frac{1}{g}\nabla\cdot\int_{p_s}^{p_{top}}qVdp\right)'}$ in moisture budget for interannual variability for MAM, with all units converted into mm/day. The top panel is the dynamical term and the bottom panel is the thermodynamic term. The columns stand for results from (left column) MME_HIST, (middle column) MME_RCP8.5, and (right column) their differences. Please refer to **Appendix 4** for details. ..... 71

**Figure 5.5** Same as **Figure 5.4** but for JJA. RegCM4_GF is excluded. ..... 72

**Figure 5.6** Decomposed dynamical term explaining the contribution from change in (left) mean specific humidity ($\Delta q$), (middle) moisture advection ($\Delta(V'\cdot\nabla\bar{q})$), and

(right) anomalous wind convergence ($\Delta(\nabla \cdot V')$) for MAM. Please refer to **Appendix 4** for details. ..... 73

**Figure 5.7** Same as **Figure 5.9** but for JJA. RegCM4_GF is excluded. ..... 73

**Figure 6.1** (i) PDF (units: %) of (a) MAM, (b) JJA, (c) SON, and (d) DJF daily rainfall for TRMM, APHRODITE, MME_HIST, and MME_RCP8.5 with respect to different intensities over an area (22 – 32°N, 110 – 120°E). The y-axis is on a log-scale. The bottom plots (ii) are the ratio of the PDFs of MME_RCP8.5 to MME_HIST. The bin width is 1mm/day. RegCM4_GF (RegCM4_AC) is excluded in JJA (SON). ..... 75

**Figure 6.2** The 95th percentile of daily precipitation (units: mm/day) in wet days during MAM for each model or reference data. The left panel shows the results from historical simulations or reference data while the right panel shows the future simulations. The name of the dataset is labeled on the top-left corner of each plot. ..... 77

**Figure 6.3** Same as **Figure 6.2** but for JJA. Results from RegCM4_GF are also shown for a reference only without any further interpretation. ..... 78

**Figure 6.4** Same as **Figure 6.2** but for SON. Results from RegCM4_AC are also shown for a reference only without any further interpretation. ..... 77

**Figure 6.5** Same as **Figure 6.2** but for DJF. ..... 79

**Figure 6.6** (left panel) Changes in 95PC per degree rise in 850hPa temperature (units: % per K) in MAM for the downscaled models and (right) the corresponding PDFs (units: %) over the area (22 – 32°N, 110 – 120°E). The expected value from CC relation (7% per K) is represented by the dotted line. The bin width is 1.5 % per K. ..... 81

**Figure 6.7** Same as **Figure 6.6** but for JJA. RegCM4_GF is excluded in the MME mean PDF. ..... 82

**Figure 6.8** 3-hourly JJA precipitation deviation from the daily mean (units: mm/day) from MME_HIST. The local time (UTC +8) is labeled on the top-land corner of each plot. RegCM4_GF is excluded. ..... 83

**Figure 6.9** Same as **Figure 6.8** but for MME_RCP8.5. ..... 84

**Figure 6.10** The first-leading EOF of JJA climatological hourly precipitation for (left panel) the spatial patterns (units: mm/day) and (right) the associated PCs. The percentages of variance explained by the PC are labeled on the top-right hand corner of the maps. Blue (Red-dotted) curve represents the time-series for MME_HIST (MME_RCP8.5). RegCM4_GF is excluded. ..... 85

**Figure 6.11** Same as **Figure 6.10** but for the second-leading EOF. ..... 86

**Figure 6.12** The JJA diurnal range (units: mm/day) for (left) MME_HIST, (middle) MME_RCP8.5 and (right) their difference. RegCM4_GF is excluded..... 86

**Figure 6.13** Same as Figure 6.1 but for 3-hourly rainfalls. RegCM4_GF (RegCM4_AC) is excluded in JJA (SON). ..... 88

**Figure 7.1** Difference of area mean (a – d) 850hPa temperature and (e – h) precipitation over 22 – 30°N, 110 – 120°E between historical and RCP8.5 simulations for (yellow and green bars) the selected GCMs and (orange and blue bars) their downscaled products using RegCM4 for (a, e) MAM, (b, f) JJA, (c, g) SON, and (d, h) DJF. GFDL-CM3 (ACCESS1-3) is excluded from the MME in JJA (SON). ..... 89

**Figure 7.2** Monthly mean of (left) area-averaged 850hPa meridional wind (southerly as positive; units: ms-1) over Southern China (20 – 35°N, 115 – 125°E) and (right) latitude with maximum zonally averaged SLP* over the western and central North Pacific (20 – 40°, 150°E – 150°W) from MME mean of GCMs for (solid blue line) historical and (dash red line) RCP8.5. ..... 92

**Figure 7.3** Monthly mean longitudinally averaged 1000hPa zonal wind (positive: westerly)

over 150°E – 150°W from MME mean of GCMs for (solid blue line) historical and (dash red line) RCP8.5.....93

# List of Tables

**Table 2.1** CMIP5 models with their corresponding model number and also the reference datasets. Most reference variables are from the reanalysis data from ERA-interim (1979 – 2005), except for precipitation which is taken from TRMM (1998 – 2013) and GPCP (1979 – 2005), and the sea surface temperature from HadISST (1979 – 2005). Selected models for the dynamical downscaling are highlight by blue color. ..... 17

**Table 2.2** The summary of eight variables examined in CMIP5 models and the corresponding testing methods. ..... 19

**Table 2.3** The result of the model selection of CMIP5 models. The color boxes indicate the scores of models, with the highest (green) equals 4 and the lowest (red) equals 1. The overall scores are list in the second last column and the last column shows the ranking of models.. ..... 30

**Table 2.4** RegCM4 configuration used in this study.. ..... 31

**Table 2.5** The short name, ICBC, and simulation period of all RegCM4 simulations conducted in this project..... 33

# 1 Introduction

## 1.1 Mean climate of Southern China and its variability

This research focuses on climate change impacts over Southern China (***Figure 1.1***). With diverse terrain, including valleys, mountains and coastline, the regional precipitation, especially on the daily or sub-daily timescale, exhibits a complex pattern (Chen et al. 2009; Dai 2001; Hirose and Nakamura 2005). To its south is the South China Sea (SCS), which is surrounded by Vietnam, the Philippines, and Borneo. The local evaporation over SCS contributes a lot in providing moisture to Southern China via the summertime prevailing southwesterly in the low levels, while there is also prominent sub-daily land-sea breeze due to land-sea temperature contrast (Chen et al. 2016; Zhou and Yu 2005). This environment provides a favorable condition for precipitation extremes, and also strong diurnal rainfall in summer over the region.

Several large-scale circulations systems are controlling the Southern China climate. The western North Pacific high and monsoons dominate the climatological circulations by determining the low-level background wind, leading to heat and moisture transport towards the region. The onset of the Asian summer monsoon induces intense and frequent rainfall over southern coastal Asia (Wang and LinHo 2001). El Niño–Southern Oscillation (ENSO) contributes to the interannual variation through teleconnection effects on the regional monsoon flow (Eopelewski and Halpert 1987; Wang et al. 2000). For extreme rainfall on a shorter time scale, tropical cyclones (TCs) play an important role. From the records of the Hong Kong Observatory, there are on average 15.8 TCs leading to warning signals, developed in the western Pacific and skimmed Hong Kong per year in the period 1956 – 2018; these systems contribute to more than one-fourth of the total rainfall in Hong Kong (HKO 2019, Lam et al.

2012). During autumn, which is the transitional season from the summer to winter monsoon, Southern China experiences a dry climate. Severe drought events caused serious losses in agricultural productivity (e.g. Zhang et al. 2013). Meanwhile, TC seasons can last until the mid-autumn in the western North Pacific; hence TCs can act as a drought breaker which regulates the regional water supply (Lam et al. 2012).

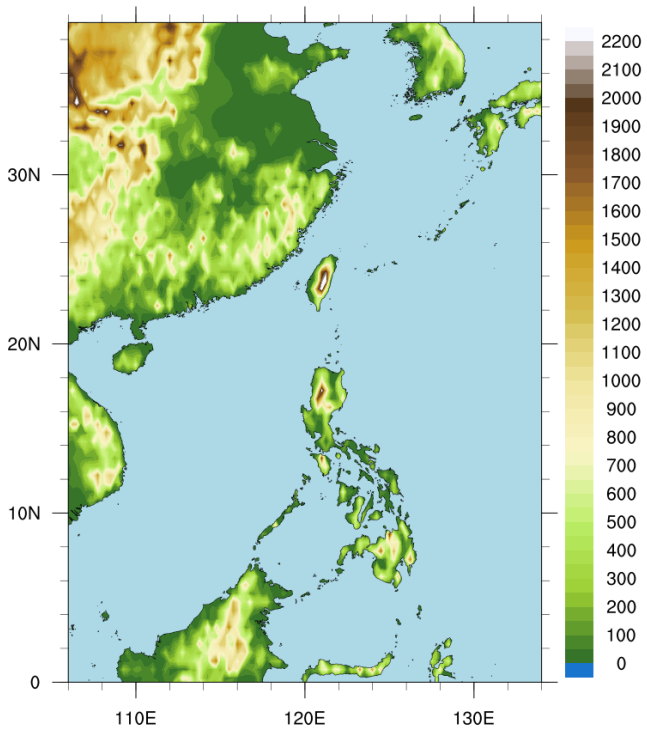


***Figure 1.1*** *Surface elevation (unit: m) within domain of interest (1°S – 40°N, 105 – 135°E).*

## 1.2 Precipitation variability in Southern China

Strong seasonality and dominant land-sea breeze make seasonal, daily and sub-daily scale rainfall important contributors to total rainfall over Southern China. For the regional hydrological cycle, the average annual precipitation can reach 1500 mm, and can even exceed 2000 mm in some coastal locations such as Hong Kong (Zhang and Cong 2014). Such a large amount of rainfall has important consequences on water

resource management, agriculture, and hazard mitigation in this region, which has a dense population. Precipitation at different time scales all leads to significant impacts in this area. For example, the seasonal to interannual rainfall variations control the productivity and types of agriculture (Tao et al. 2004). Rainfalls with shorter scales can be very intense and cause hazards like flooding and landslides in the wet seasons (Lyu et al. 2013).

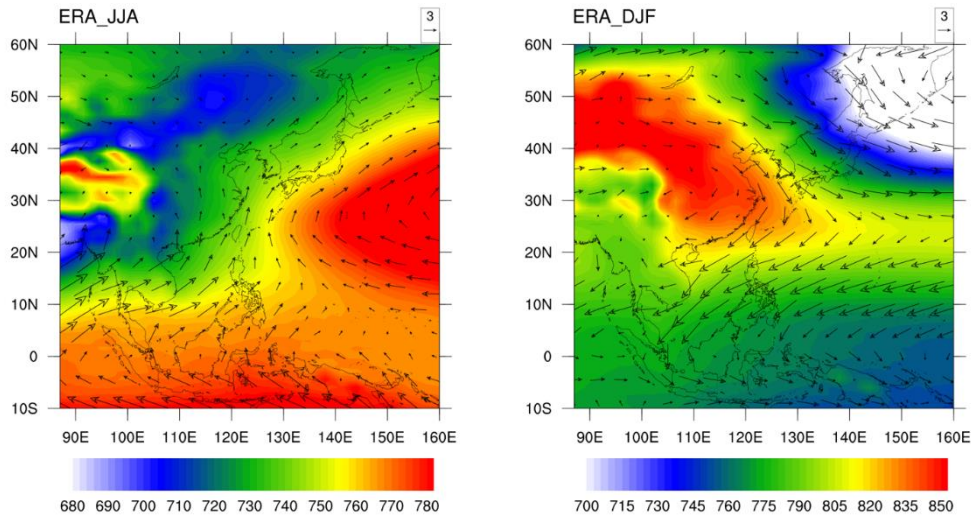


***Figure 1.2*** *(left) June-to-August (JJA) and (right) December-to-February (DJF) 925hPa geopotential height (shading, units: m) and wind (arrows, units: ms$^{-1}$) from the ERA-Interim Reanalysis dataset (1979 – 2005).*

The climate in Southern China is strongly affected by the East Asian Monsoons (***Figure 1.2***). Differential radiative heating induces land-sea temperature and pressure contrast which results in strong low-level southwesterly or southeasterly in summer. The warm and moist air streams from the ocean cause an increase in both precipitation and temperature, starting from mid-May and reaching a peak in June to August (Wang and LinHo 2001). The wet season ends when the Siberian High develops in late September, due to the rapid cooling of the East Asian continent. Subsidence developed

in the inland region forms a high-pressure anomaly which pushes air towards the ocean and produces a low-level northwesterly or northeasterly over a broad continental region. The dry northerly effectively reduces the humidity and precipitation, starting from October, followed by the onset of winter monsoon in late November, characterized by cold and dry circulations. The monthly area-averaged near-surface temperature, meridional wind, and precipitation over Southern China are shown in ***Figure 1.3*** in order to depict the seasonal cycle. The western Pacific subtropical high (WPSH) is another important system altering the climate and its seasonality in Southern China. The sinking branch of the Hadley circulation locates over the western North Pacific dynamically forms this large and semi-permanent anticyclonic flow covering most regions in East Asia during summer (Rodwell and Hoskins 2001). The contribution from WPSH depends on its strength and location. The southwesterly wind near the western rim of WPSH brings more rain to Southern China, but the high-pressure anomaly can make the weather fine there if WPSH extends more westward.

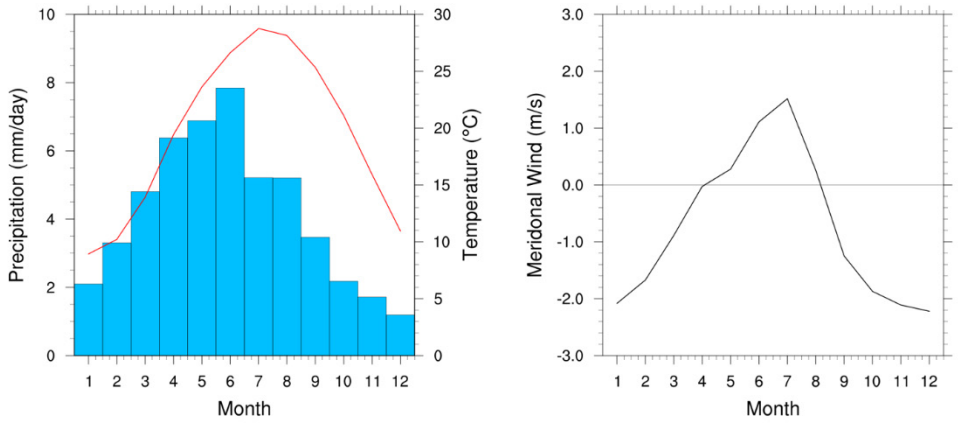


***Figure 1.3*** *Monthly averaged (left, blue bars) precipitation from APHRODITE (1979 – 2003), (left, red line) 1000hPa temperature and (right, southerly as positive) meridional wind from the ERA-Interim Reanalysis dataset (1979 – 2003) over the continental area in 20 – 30°N, 110 – 120°E.*

Variability related to ENSO, subtropical high, and monsoons gives rise to a strong

interannual variation of precipitation in Southern China. ENSO is an atmosphere-ocean coupled phenomenon in the tropical Pacific Ocean with a warmer (colder) eastern Pacific sea surface in the positive (negative) phase, i.e. El Niño (La Niña). ENSO has the strongest influence on the global climate during the boreal winter, with periods ranging from about 3 to 7 years (Wu et al. 2008). The warner (colder) sea surface temperature (SST) anomalies over the eastern Pacific in El Niño (La Niña) further suppress (enhance) the Walker circulation via the Bjerknes feedback (Bjerknes 1996). The induced anticyclone due to the anomalous subsidence over the western Pacific during El Niño years interacts with the monsoons by providing a southwesterly wind component from SCS towards Southern China, which enhances the local precipitation (Wang et. al, 2000). The effects of La Niña on precipitation are less prominent than that of El Niño over Southern China, with no significant deviations from that during the neutral state (Zhang et al. 2015). Lau and Yang (1997) found that the onset of East Asian summer monsoon (EASM) is delayed during El Niño years; this also leads to the later evolution of EASM and affects the summer precipitation. EASM exhibits an interannual variability partially independent of ENSO. Potential causes of the variability include the degree in differential heating between land and ocean, the continental meridional temperature gradient, or even interactions between other circulation systems, such as the mid-latitude jet (Li and Yanai 1996). A stronger (weaker) summer monsoon wind circulation corresponding to a tendency of having more (less) precipitation (Wang and Lau 2001). EASM has a strong negative correlation with the strength of WPSH as well (Wang et al. 2013). WPSH was found to have significant variations with a typical period of 2 to 4 years. The strength and position of WPSH are highly dependent on SST anomalies and convective motion over SCS and the western tropical Pacific (Sui et al. 2007). ENSO is one of the possible factors of the WPSH variability. WPSH tends to be eastward retreated and weakened

during a developing strong El Niño in summer (Xue et al. 2018). The suppressed easterly component over Southern China due to the eastward retreated or weaker WPSH is favorable for the southwesterly driven by EASM, which additionally interacts with the reduced local high-pressure anomaly making Southern China rainier. Weakened WPSH also allows the Mei-yu fronts to linger at more southern latitudes, implying more precipitation in Southern China in late spring and summer (Chang et al. 2000). Besides, both ENSO and WPSH variations have an impact on TC genesis and frequency in the Western North Pacific (Camargo and Sobel 2005, Wang et al. 2013). TCs tend to become more intense and longer-lived in El Niño years. Also, with a weaker or less westward extended WPSH, the number of TC genesis and days with tropical storms in tropical Pacific is higher (Wang et al. 2013, Camp et al. 2019). TC-related rainfall thus has a strongly varying temporal distribution, which further contributes to the precipitation variability in Southern China.

Intense precipitation often happens in late spring and summer over Southern China. In fact, hydrological extremes, like flooding, become common natural hazards that cause loss of human lives and large damage in agriculture and properties over Southern China (Huang et al. 2008, Li et al. 2012, Zhang et al. 2012). Jiang and Zipser (2010) reported that TCs originate in the tropical Western Pacific play an important role in precipitation extremes. They also found that ENSO events have a significant contribution to the precipitation extremes, especially the TC rain here. According to Wu et al. (2016), preexistent precipitation extremes (PPEs) not related to TCs account for about 40% of total events during April – August. They can be triggered by synoptic disturbances at different vertical levels. The South Asian high (SAH) interacts with the westerly jet and can form a strong upper-level divergent anomaly during PPEs. WPSH enhances cold air intrusion in the middle levels and converges the southwesterly

monsoon and the southeasterly from the southern flange of WPSH in the low levels over Southern China. These impacts from SAH and WPSH enhance lower-level moisture transport towards Southern China, which triggers the formation of PPEs. Extreme rainfalls in early spring and autumn are rare. In winter, occasionally there are extreme rainfalls during strong El Niño and a positive phase of Indian Ocean Dipole (Zhang et al. 2015).

Diurnal rainfall is an important component of the Southern China hydrological cycle (Wai et al. 1996; Hirose and Nakamura 2005; Chen et al. 2009; Yuan 2013; Huang and Chen 2015). Much attention has been paid to diurnal rainfall variations in recent years, following the improvement in the reliability, accuracy, and spatiotemporal resolution of data from remote sensing, such as the Tropical Rainfall Measuring Mission (TRMM) 3B42 satellite precipitation (Huffman et al. 2007) and land-based weather stations. The average rain rate difference between morning and afternoon hours can exceed 20%, and even 40% for the coastal region, of the daily mean rainfall during summer over Southern China (Chen et al. 2009). The local diurnal cycle can be classified into two kinds: morning rainfall over the ocean, islands and coastal regions, and afternoon rainfall over inland areas. The diurnal rainfall is generally more significant over the land than the ocean, because of a stronger diurnal temperature variation and a more limited moisture supply, making the precipitation more sensitive to solar heating over the continent (Dai et al. 2006). Local terrain also affects diurnal rainfall over land. For example, mountainous locations experience an earlier diurnal rainfall than the valley (Gebremichael et al. 2007). Terrain-slope heating is favorable for inland cloud formation. More intense diurnal rainfalls are found over coastal regions. The diurnal land-sea breeze characterized by the differential heating also allows the propagation of convection signals (Ichikawa and Yasunari 2006, Chen et al, 2016). For Southern

China, coastal morning rainfall starts near 05:00 to 06:00 local time (LT), which decreases rapidly in the afternoon; while the afternoon rainfall peak is found over land around 15:00 to 17:00 LT (Dai et al. 2006, Chen et al. 2009, Chen et al, 2016, Lui et al. 2019a). Diurnal rainfall also has a strong seasonality; pre-summer (May and June) and mid-summer (July and August) diurnal variations are much stronger than other seasons (such as spring, though the latter is a wet season in Southern China; see Wai et al. 1996, Dai et al. 2006, Chen et al. 2009, Huang and Chen 2012).

### 1.3 Precipitation characteristics in Southern China under the warming climate

From the Intergovernmental Panel on Climate Change Fifth Assessment Report (IPCC AR5), the change in precipitation due to warming climate is complex in Asia, owing to topographic effects, large scale circulation, etc. (WGI AR5). From observations, the mean state rainfall is becoming more intense over Southern China starting from the 1950s using land-station data (Zhang and Cong 2014). For the projected future climate, it was found that most regions have a general reduction in background circulation, however, enhanced moisture capacity of the troposphere results in stronger precipitation. Meanwhile, EASM circulation and rainfall are projected to increase in the future, after the interdecadal weakening during the 1960s to the 1980s (***Figure 1.4***). A strengthened EASM with a moister atmosphere increases the regional precipitation significantly in summer.

On the other hand, the East Asian winter monsoon (EAWM) has been weakening since the 1980s. There is however no consensus in the projection of the strength of EAWM among different studies; one of the reasons is the different definitions of the EAWM intensity in these works. It is claimed that the wintertime East Asia trough (EAT) is projected to be more northeast-southwest tilted (Xu et al. 2016). This more NE-SW

tilted EAT will reduce the tendency of EAWM to take the southern pathway towards East Asia and decrease the local winter monsoon intensity. Hong et al. (2017) also found that the intensity of EAWM denoted by different indices drops in the future based on general circulation model (GCM) simulations. The weakened EAWM reduces dry air transport from the north and results in more rainfall over Southern China. Thus, despite the weak agreement in the future projection of EAWM, the winter precipitation is projected to increase significantly in the future over East Asian regions.

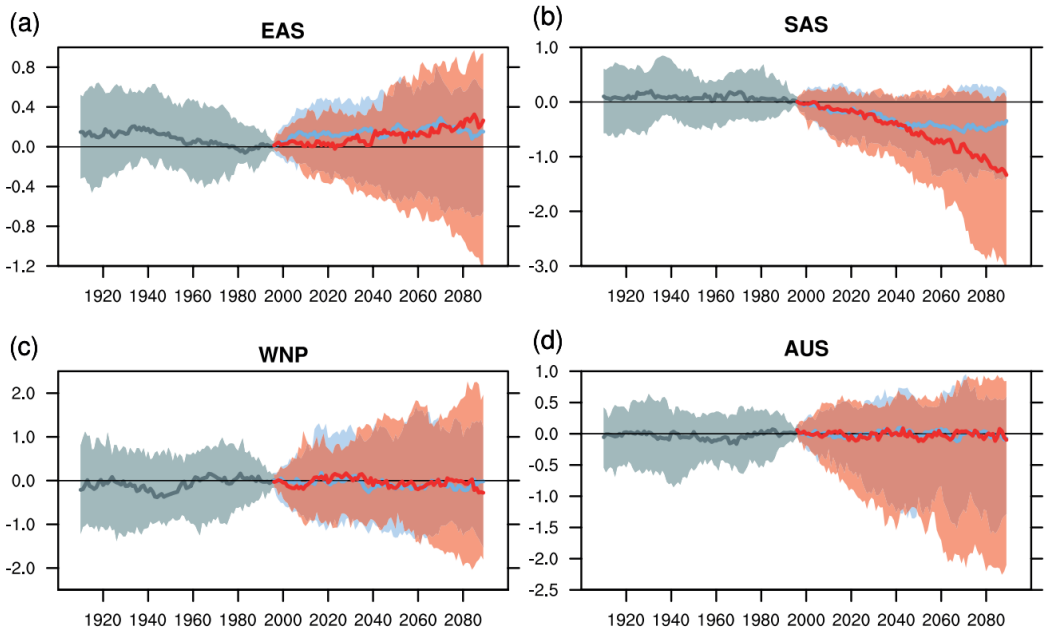


***Figure 1.4*** *(Grey) Historical, (light blue) RCP4.5, and (red) RCP8.5 simulated time-series of summer monsoon indices over (a) East Asia, (b) South Asia, (c) western North Pacific, and (d) Australia. Reprinted from the IPCC AR5 WGI Figure 14.5 (Christensen et al. 2013).*

The interannual precipitation variability over Southern China is expected to increase, especially during summer, based on CMIP3 and CMIP5 model projections (Christensen et al. 2013). There is high confidence that ENSO will remain the dominant mode of interannual global climate variability in the future (Christensen et al. 2013). Monsoon variability and rainfall are highly correlated with ENSO (Wang et

al. 2000, Wu et al. 2003); understanding how the monsoon-ENSO teleconnection changes is essential in projecting monsoon variability. However, changes in ENSO are highly uncertain (Collin et al. 2010, Cai et al. 2015). Regarding the future monsoon-ENSO relationship and related precipitation characteristics, it is expected to remain strong under a warmer climate (Li et al. 2010, Annamalai and Sperber 2016). Some recent results based on improved numerical models projected an increased monsoon-ENSO-related rainfall amount (Wang et al. 2019). Apart from the intensity, there is also a possible frequency change in the non-neutral state of ENSO (Cai et al. 2015); El Niño and extreme La Niña years are expected to be more common. This can result in enhanced interannual precipitation variations through teleconnection. The frequency of strong TCs and the lifetime maximum-intensity of TCs in the western North Pacific are both projected to increase (Ying et al. 2012, Christensen et al. 2013). The related rainstorms will contribute in a positive way to future precipitation variability in summer, especially over coastal locations.

Unlike the mean state precipitation, which is limited by the moisture supply within a region, extreme precipitation rates are highly dependent on the ability of the atmosphere in holding moisture. Generally, the impacts of a warmer climate on extreme rainfall will be stronger compared to that on mean state rainfalls (Easterling et al. 2000; Trenbeth 2011). The increase in extreme precipitation rates roughly follows the Clausius–Clapeyron relation (CC relation) according to observational studies (e.g. Schroeer and Kirchengast 2018) and high-resolution GCM experiments (Lui et al. 2019b). The CC relation indicates that the saturated water vapor pressure increases with temperature thermodynamically. The rainfall rate of a precipitation event increase directly with temperature once there is excessive moisture supply. Under a typical situation of the atmosphere, there will be about a 7% increment in moisture holding

capacity, as well as the resulting extreme precipitation rates, per one degree Celsius of low-level tropospheric temperature rise (Pall et al. 2007). Apart from pure thermodynamic reasoning, changes in extreme precipitation can also be attributed to other factors, such as changes in regional total precipitation amount (Zhai et al. 2005), TC rain (Ying et al. 2012, Lui et al. 2019b), monsoon characteristics (Christensen et al. 2013, Zhang et al. 2015) and large-scale circulation (Wang and Zhou 2005). These factors can affect extreme precipitation rates and make them deviate from the CC relation. Numerous regional climate model (RCM) studies projected a significant intensification in extreme precipitation in different domains (e.g. Beniston et al. 2007; Gao et al. 2002; Ngo-Duc et al. 2017).

Studies using RCMs were carried out to project the changes in the diurnal rainfall under the warmer climate in different regions. Spatial shifting and intensification or reduction of the diurnal cycle are suggested by some model experiments (e.g. Liang et al. 2004). There are also studies indicating that the diurnal cycle will not have a significant change in some geographical locations (e.g. Laprise et al. 2013). The propagation of diurnal-scale convective signals is highly dependent on the regional circulations and land-sea temperature contrast over the coastal regions (Ichikawa and Yasunari 2006, Chen et al, 2016). Due to projected changes in land-sea temperature contrast (Sutton et al. 2007) and large atmospheric circulations (Sooraj et al. 2015), potential changes in the temporal distribution of diurnal rainfall in Southern China are worth investigating. In this project, the focus will be on the future change in the intensity and the spatiotemporal distribution of the diurnal rainfall.

### 1.4 Climate model and dynamical downscaling

Climate models are important for deepening our understanding of weather phenomena

and the predictability of future climate. General circulation models (GCMs) are tools to mathematically represent the major Earth system components determining the climate, including the atmosphere, land surface, ocean, and sea ice. Circulation variables, such as wind, temperature, pressure, etc., are temporally and spatially evolving. Climate simulations using GCMs are conducted by prescribing some external forcings and allowing the variables to evolve within a target period. Therefore, the evolution of the climate system can be numerically estimated by model integrations.

Some projects were conducted using the coupled atmosphere-ocean general circulation models (AOGCMs). The experiments were conducted by prescribing initial conditions of the atmosphere and ocean with additional forcings of the globe under different climate scenarios. The Coupled Model Intercomparison Project (CMIP), which was established by the World Climate Research Programme and the Working Group on the Coupled Modelling since 1995, is one of the most representative projects constructing experiments using AOGCMs from different climate institutes. The project provided public accessible datasets of simulation results from individual AOGCM for further investigations under different scenarios. In Phase 5 (CMIP5, https://esgf-node.llnl.gov/projects/cmip5/), simulations under climate scenarios suggested in the IPCC AR5, known as Representative Concentration Pathways (RCPs), were included. The RCPs represent a possible range of changes in the atmospheric concentration of greenhouse gases labeled by equivalent values of increase in the radiative forcing (in $W/m^2$) in the year 2100 (Van et al. 2011). In CMIP5, experiments were designed to provide results on long-term and atmosphere-only simulations for the $19^{th}$ – $21^{st}$ centuries. Further analysis of the projected climate for the next century is thus feasible based on CMIP5 results.

In order to reduce the computational costs to simulate the whole global climate, the

horizontal resolution of GCMs is usually coarse (> 100km). Some small-scale weather phenomena and weather extremes cannot be resolved by the coarse-resolution GCMs (Giorgi et al. 2009). In regional climate models (RCMs), higher spatial and temporal resolutions can be achieved compared to GCMs, with about the same computation cost, by limiting the simulation domain. The simulation starts by prescribing the initial conditions and lateral boundary conditions (ICBC) of the atmosphere and sea-surface. The structure of smaller-scale weather phenomena can be resolved with higher definitions. Finer-scale simulations can also improve the interaction between climate variables and topography as well as representations of processes in the subgrid-scale regime in GCMs. The simulated climate phenomena, especially for the weather extremes and cumulus convection which have small scales in both time and space, are thus more reliable and have finer features in RCMs.

Even though some simulation experiments were using high-resolution GCM recently (e.g. Murakami 2012; Plosphay and Lau 2010), the long simulation time makes the ensemble experiments less feasible. Thus, those GCM simulations rely much on the physics of a single model, which may induce biased simulation results. Some studies found that simulations based on averaging multi-model results are far better than using single model simulations in probabilistic climate projection (Tebaldi and Knutti 2007). A lot of running time is actually spent on the grids over regions that are not of interest in GCM simulations; RCM can save computation time by limiting the simulation within the domain of interest. As a result, more model outputs can be generated by RCM than by GCM at the same time with a similar or even usually a finer resolution. This advantage makes RCM simulations with multi-model ensembles more effective, by introducing ‘dynamical downscaling’ techniques.

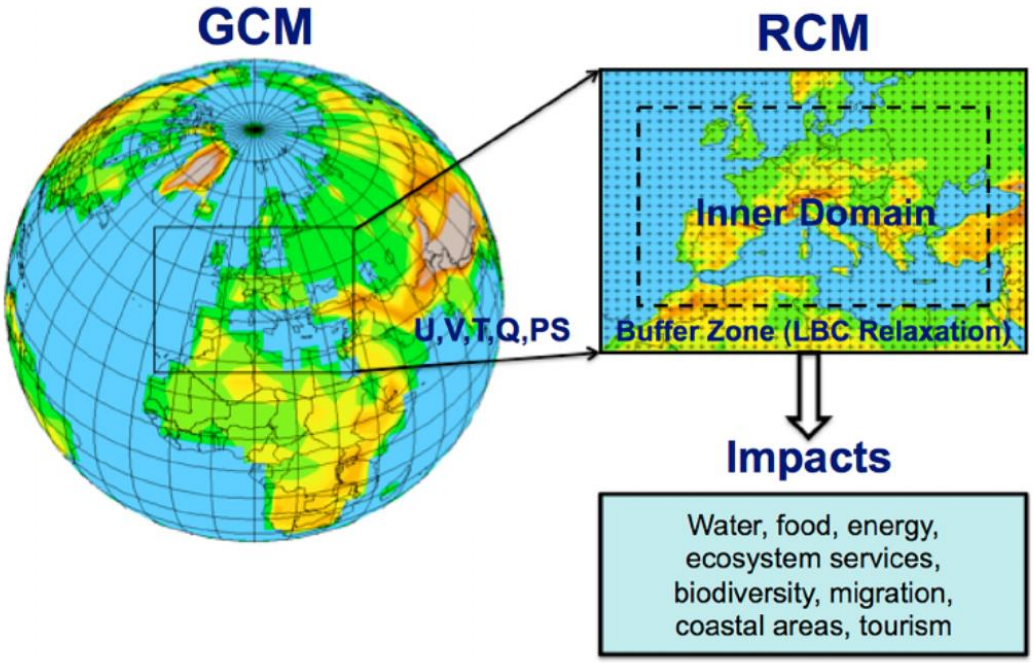


***Figure 1.5*** *Schematic depiction of regional climate modeling and application. Reprinted from Giorgi 2019.*

One commonly used downscaling technique is called 'statistical downscaling', which relates the GCM output with the regional climate variables using observatory data (Wilby and Wigley 1997). Statistical downscaling is not adopted in this project because the statistical relationship between GCMs and local variables in the future climate cannot be guaranteed. It also assumes that the statistical relation will remain the same in the future which might not be true. Dynamical downscaling is another downscaling technique involving the construction of ICBC of RCMs. It allows the RCM to simulate the future climate by providing suitable ICBC using governing physical equations. Those physical equations should not be time-varying, hence dynamical downscaling provides a climate projection with a more reasonable physical interpretation.

To conduct a downscaling experiment, climate variables generated from coarser-resolution GCMs are introduced into the ICBC of an RCM. ***Figure 1.5*** provides a schematic diagram to illustrate the mechanism of dynamical downscaling.

Meteorological variables including wind (U, V), temperature (T), specific humidity (Q), and surface pressure (Ps) are taken from the GCM. These variables are then prescribed as lateral boundary conditions (LBC) within the buffer zone of RCM via a diffusion process. RCM can hence calculate new variables related to the climate, such as precipitation, cloud formation, soil moisture, etc. from its implemented physical schemes. The newly calculated climate variables with a more comprehensive spatiotemporal description are used for further studies about the regional impacts of climate variations and climate change.

### 1.5 Research objectives and thesis outline

Although there were many studies on projecting the hydrological characteristics over different domains, most of them using AOGCMs give a strong consensus only over a broad region. Regional climate projection remains uncertain because of various influences of complex local features, such as terrain, local circulation, and teleconnections with the changing large-scale circulations. This research aims at projecting the hydrological characteristics over Southern China, based on the dynamical downscaling technique. The following are the objectives of this study:

1. To examine the performance of RegCM4 in dynamical downscaling GCM outputs, with a focus on hydrological events at various timescales over Southern China.
2. To quantify changes in rainfall characteristics at various time scales due to global warming.
3. To understand the mechanisms responsible for such precipitation changes.

To achieve the first goal, GCMs capable of simulating important circulation features affecting Southern China are selected from a list of CMIP5 models. The research methodology, including details of GCM selection, the RegCM4 configuration, and the

experiment design are presented in chapter 2. Chapter 3 evaluates the performance of dynamical downscaling by comparing raw GCM and downscaled circulation variables. Chapters 4 to 6 address the second and third research goals. Hydrological cycles including “seasonal mean state precipitation”, “interannual seasonal precipitation variability”, and “daily and sub-daily precipitation distribution and extreme” are presented in these three chapters respectively. Discussion on the mechanisms and climate attribution of the changes are included by the end of each chapter. Chapter 7 is a conclusion summarizing the results in chapters 4 to 6 with discussions.

# 2 Data and Methodology

## 2.1 CMIP5 GCM selection

22 GCMs from the Coupled Model Intercomparison Project, Phase 5 (CMIP5) (Taylor et al., 2012) were first ranked according to their performance on simulating important climate variables or elements over Southern China, to select suitable models for providing LBC for dynamical downscaling. ***Table 2.1*** gives the analyzed CMIP5 models and the reanalysis/observational data for reference. The domain of analysis is (1°S – 40°N, 105 – 135°E), as shown in ***Figure 1.1***. The data from CMIP5 models in ***Table 2.1*** with the period 1979 – 2005 were used to examine their performance, based on comparison with ERA-interim Reanalysis and HadISST for the same period. Also, TRMM for the period 1998 – 2013 was used for evaluating model precipitation. Eight circulation variables/elements were examined for evaluating the performance of CMIP5 models (see ***Table 2.2***).

| Index | Acronym of Model | Modeling Center/Institute |
|---|---|---|
| **1** | ACCESS1-0 | Commonwealth Scientific and Industrial Research Organization and the Bureau of Meteorology, Australia |
| **2** | ACCESS1-3 | |
| **3** | bcc-csm1-1 | Beijing Climate Center (BCC), Yunnan University, and China Meteorological Administration |
| **4** | bcc-csm1-1-m | |
| **5** | CanESM2 | Canadian Centre for Climate Modelling and Analysis |
| **6** | CMCC-CM | Euro-Mediterranean Center on Climate Change, Italy |
| **7** | CNRM-CM5 | National Centre for Meteorological Research, France |
| **8** | CSIRO-Mk3-6-0 | Commonwealth Scientific and Industrial Research |

| | | |
|---|---|---|
| | | Organization and Queensland Climate Change Centre of Excellence, Australia |
| **9** | FGOALS-g2 | LASG, Institute of Atmospheric Physics, Chinese Academy of Sciences |
| **10** | GFDL-CM3 | NOAA Geophysical Fluid Dynamics Laboratory, USA |
| **11** | GFDL-ESM2G | |
| **12** | GFDL-ESM2M | |
| **13** | HadGEM2-ES | Met Office Hadley Center, UK |
| **14** | IPSL-CM5A-LR | Institut Pierre Simon Laplace, France |
| **15** | IPSL-CM5A-MR | |
| **16** | IPSL-CM5B-LR | |
| **17** | MIROC5 | Japan Agency for Marine-Earth Science and Technology, Atmosphere and Ocean Research Institute (The University of Tokyo), and the National Institute for Environmental Studies |
| **18** | MIROC-ESM | |
| **19** | MIROC-ESM-CHEM | |
| **20** | MPI-ESM-MR | Max Planck Institute for Meteorology, Germany |
| **21** | MRI-CGCM3 | Meteorological Research Institute, Japan |
| **22** | NorESM1-M | Norwegian Climate Center, Norway |

**Observational/Reanalysis Data**

| | |
|---|---|
| ERA-interim (1979 – 2005) | European Centre for Medium-Range Weather Forecasts (ECMWF) |
| TRMM 3B42 (1998– 2013) | NASA and the Japan Aerospace Exploration Agency |
| HadISST (1979 – 2005) | Met Office Hadley Center, UK |
| Global Precipitation | World Climate Research Programme (WCRP) |

| |
|---|
| Climatology Project (GPCP) |
| (1979 – 2005) |

***Table 2.1*** *CMIP5 models with their corresponding model number and also the reference datasets. Most reference variables are from the reanalysis data from ERA-interim (1979 – 2005), except for precipitation which is taken from TRMM (1998 – 2013) and GPCP (1979 – 2005), and the sea surface temperature from HadISST (1979 – 2005). Selected models for the dynamical downscaling are highlight by blue color.*

| Variables | Method |
|---|---|
| **1. Summer Monsoon** | Taylor diagram of 850hPa JJA u-wind over (5-25°N, 90-130°E) |
| **2. Winter Monsoon** | Taylor diagram of 850hPa DJF v-wind over (25-50°N, 110-140°E) |
| **3. Summer Temperature** | Taylor diagram of 850hPa JJA temperature over the domain of interest |
| **4. Winter Temperature** | Taylor diagram of 850hPa DJF temperature over the domain of interest |
| **5. Summer Precipitation** | Visual inspection (5-25°N, 90-140°E)[!] |
| **6. ENSO Variability** | Taylor diagram & visual inspection of regressed DJF & MAM 850hPa wind & SST on Niño3.4 index[@] |
| **7. Summer Monsoon Variability** | Taylor diagram & visual inspection of regressed 850hPa wind & precipitation on EASM index[#] |
| **8. Winter Monsoon Variability** | Taylor diagram & visual inspection of regressed 850hPa wind & precipitation on EAWM index[*] |

*#: GPCP dataset is used such that the reference data and model simulations cover the same period.*

*!@#*: Please refer to the text for the algorithm to examine the performance of these variables.*

***Table 2.2*** *The summary of eight variables examined in CMIP5 models and the corresponding testing methods.*

To evaluate the model outputs, spatial correlation, standard deviation, and root mean square error were compared for most variables. The statistics were summarized by Taylor diagrams (Taylor 2001). For wind and temperature, most models give magnitudes comparable to those from the reference data. Hence, a Taylor diagram can be solely used to determine model performance. For precipitation and some of the regression maps, because some models cannot generate reasonable amplitudes/patterns, visual inspection was used. After examining their performance, models were ranked according to their simulations in these eight variables. A detailed description of the ranking method and results can be found in **Appendix 1**.

### 2.1.1 Summer and winter monsoon

For the summer monsoon, the 850hPa zonal wind over the area bounded by the red box in ***Figure 2.1 (left)*** is considered:

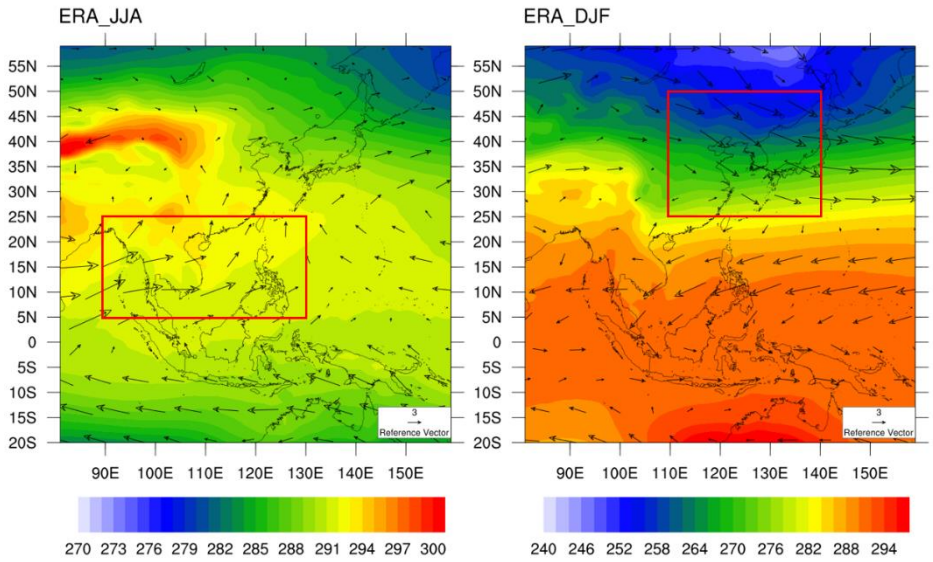


***Figure 2.1*** *(left) JJA and (right) DJF mean 850hPa wind (arrows, units: ms-1) and 850hPa temperature (shading, units: K) calculated from ERA-interim dataset with the period (1979 – 2005). The red box in both plots indicates the region where the monsoon pattern can be indicated.*

This area is chosen because the southwesterly wind over this region is a dominant feature of the summer monsoon. The zonal component of the 850hPa wind over this region is also an indicator of the onset and maintenance of the summer monsoon over SCS and Southern China (Yihui and Chan 2005).

***Figure 2.2 (left)*** shows a Taylor diagram for the JJA zonal wind (uwind) at 850hPa, for assessing models' performance in capturing the East Asia Summer Monsoon (EASM). Taylor diagram can provide the pattern correlation (angular axis), standardized deviation (radial axis), and the calculated root mean square error (distance between the point and REF) for a particular variable from models versus observations. The closer a point to REF, the better the result is. Models inside the second grey semicircle are classified as having the best performance and are given a score of 4. For those models located between the second and the third grey semicircle,

they are given a score of 3, and so on. From ***Figure 2.2 (left)***, the performance of models varies a lot. Nonetheless, the general performance of models in simulating the mean EASM circulation is quite well.

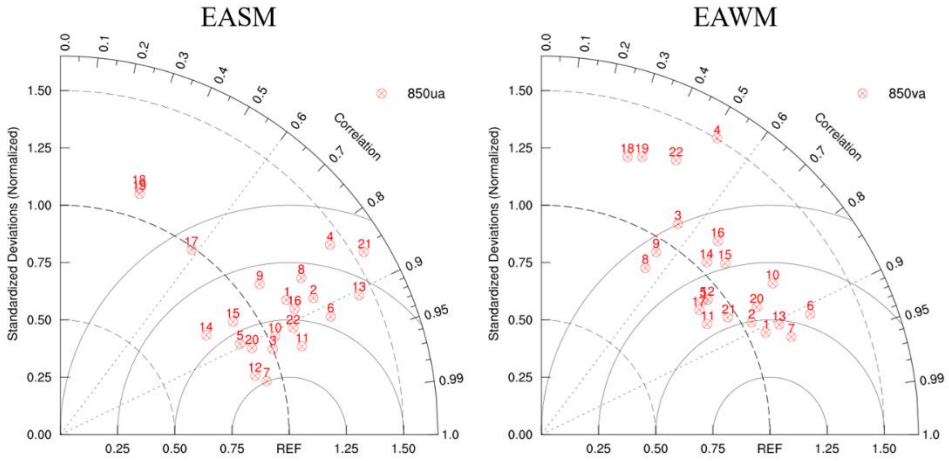


***Figure 2.2*** *Taylor diagrams for (left) JJA 850hPa zonal wind and (right) DJF 850hPa meridional wind based on values over the domains outlined in* ***Figure 2.1****. The angular axis and the radial axis indicate the pattern correlation and the standardized deviation respectively. The distance between a point and REF indicates the root mean square error of the corresponding model.*

***Figure 2.1 (right)*** and ***2.2 (right)*** show the focused area and a Taylor diagram respectively, for the 850hPa meridional wind (vwind), for East Asia Winter Monsoon (EAWM) evaluation. Compared to EASM, EAWM is dominated by the meridional component for the low-level wind. Most models can generate a reasonable magnitude and spatial distribution of the vwind in the environments.

### 2.1.2 Summer and winter temperature

For 850hPa temperature for JJA and DJF, Taylor diagrams are also used to summarize the performance of models in the whole domain of interest (***Figure 1.1***).

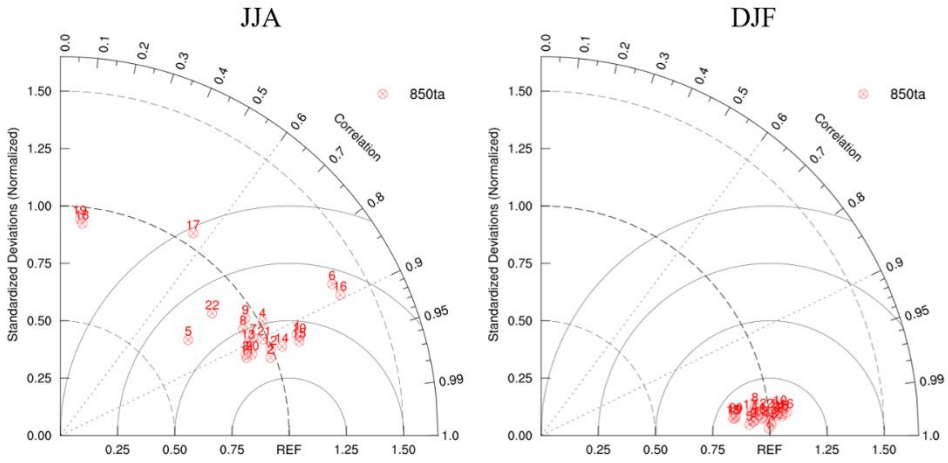


***Figure 2.3*** *Same as* ***Figure 2.2****, but for (left) JJA 850hPa temperature and (right) DJF 850hPa temperature over (6°S – 45°N, 100 – 140°E).*

For the summer temperature (see ***Figure 2.3 (left)***), most models can give a reasonable summer temperature and obtain a score of 4, except for models 17, 18, and 19. For winter, all models perform very well and have a score of 4.

### 2.1.3 Summer precipitation

For summertime precipitation, most models cannot give a reasonable magnitude, especially in the coastal area in Southern China. Therefore, the performance of models is further determined by inspection. It is because precipitation is not a primary variable prescribed into the RCM. The spatial patterns of rainfall are closely related to the wind circulation, which makes the spatial distribution a more important indicator of the performance of precipitation than the exact magnitude. Besides, models with coarse resolutions tend to give too little precipitation over coastal locations with complex terrains, such as east of the Philippines or coastal Southern China. The common failure in simulating a reasonable magnitude of precipitation near those locations also reduces the significance of the magnitude in determining the performance of models.

To illustrate the algorithm to determine the quality of JJA precipitation. ***Figures 2.4*** and ***2.5*** show the summertime mean rainfall from models. For models with a reasonable output of JJA precipitation (e.g. ACCESS1-0), the major rain-band location should be comparable to that in the reference data. The local maximum over southeastern China is also important as this is the focus area of this study. Models 1 and 13 are found to give the best pattern compared with the reference data. Classification of the performance of all listed models and the reason behind can be found in **Appendix 1.1**.

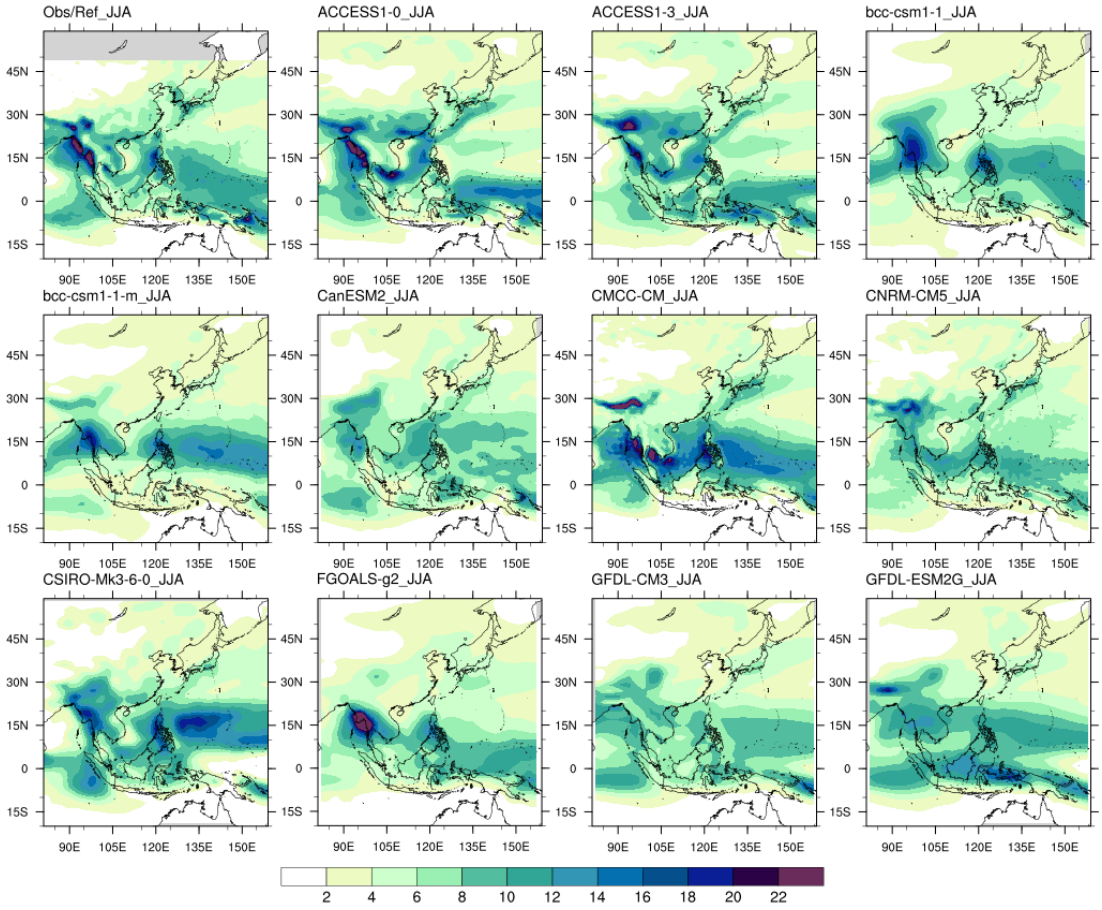


***Figure 2.4*** *The JJA mean precipitation (units: mm/day) of the reference data (top-left) and models 1 – 11 in* ***Table 2.1****.*

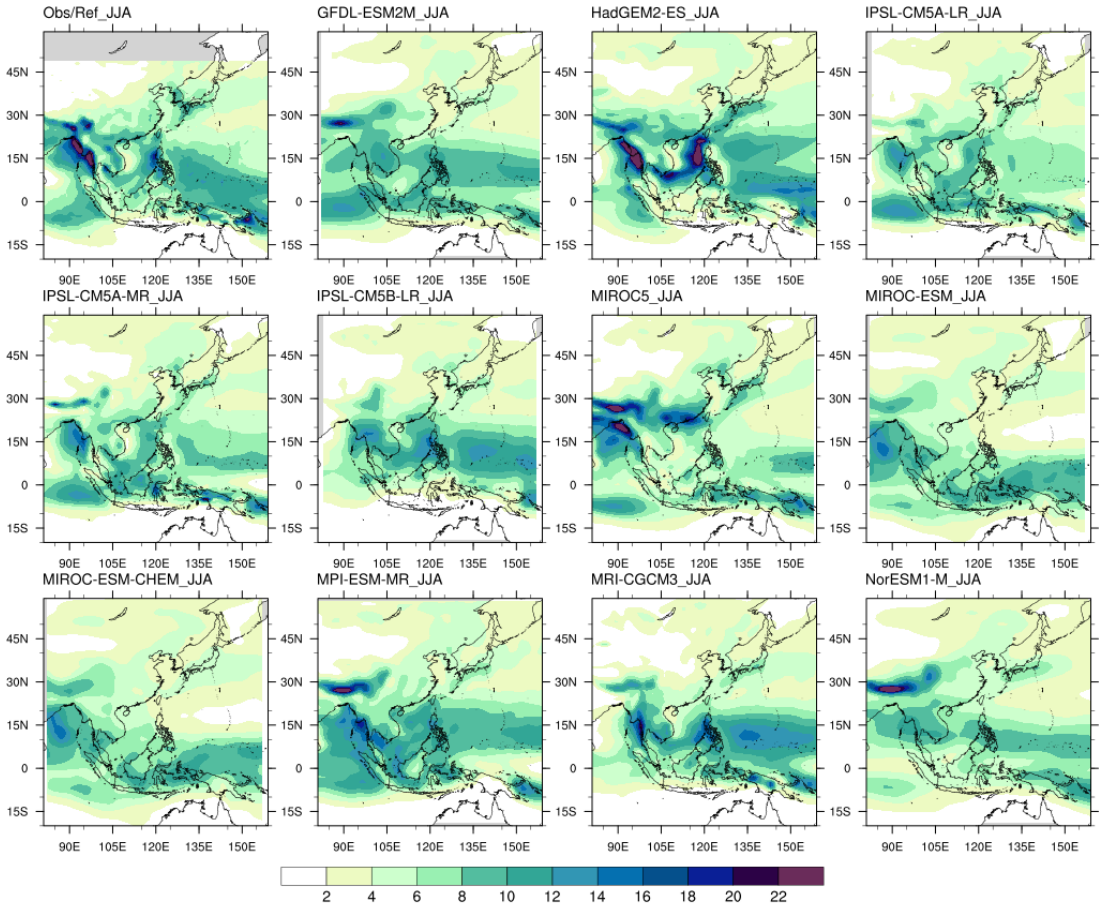


***Figure 2.5*** *Same as* ***Figure 2.4*** *but for models 12 – 23.*

### 2.1.4 ENSO variability

To obtain ENSO-related circulation signals, model and reference data are regressed onto the Niño3.4 index (Bamston et al., 1997), which is defined as the anomalous area-averaged SST over 5°S – 5°N, 170°W – 120°W. The region Niño3.4 is chosen because it contributes to the seasonal regional climate with some well-known teleconnections (e.g. Ropelewski & Halpert, 1987).

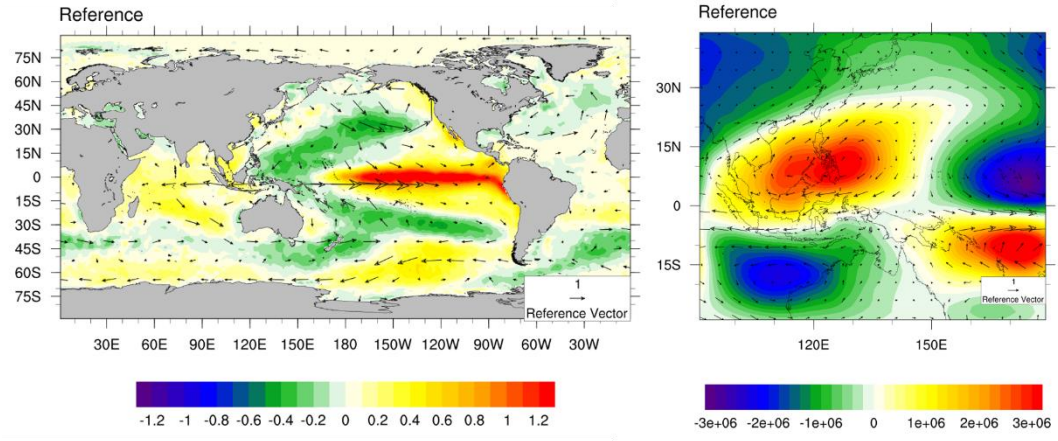


***Figure 2.6*** *(left) Regressed global DJF 850hPa wind (arrows, unit: $ms^{-1}$) and sea-surface temperature (shading, unit: K) and (right) the regressed DJF 850hPa wind (arrows, unit: $ms^{-1}$) and 850hPa stream function (shading, unit: $m^2s^{-1}$) over the western Pacific and southeastern Asia of the reference data onto the Niño3.4 index.*

The time series of the Niño3.4 index was calculated for each individual model. 850hPa wind and SST were then regressed on to the index to extract the ENSO variability and related teleconnections. Regression maps for 850hPa wind and SST are plotted in ***Figure 2.5***. Positive anomalous equatorial SST extending from South America to the central Pacific, and also the low-level anticyclone covering the Philippines, adjacent to southeastern China, are two important features related to ENSO (Wang et. al, 2000). The western part of the anomalous anticyclone enhances southwesterly, thus acts against the northeasterly background wind during winter, and enhances rainfall over southeastern China. A similar effect is found in MAM, but with weaker magnitude.

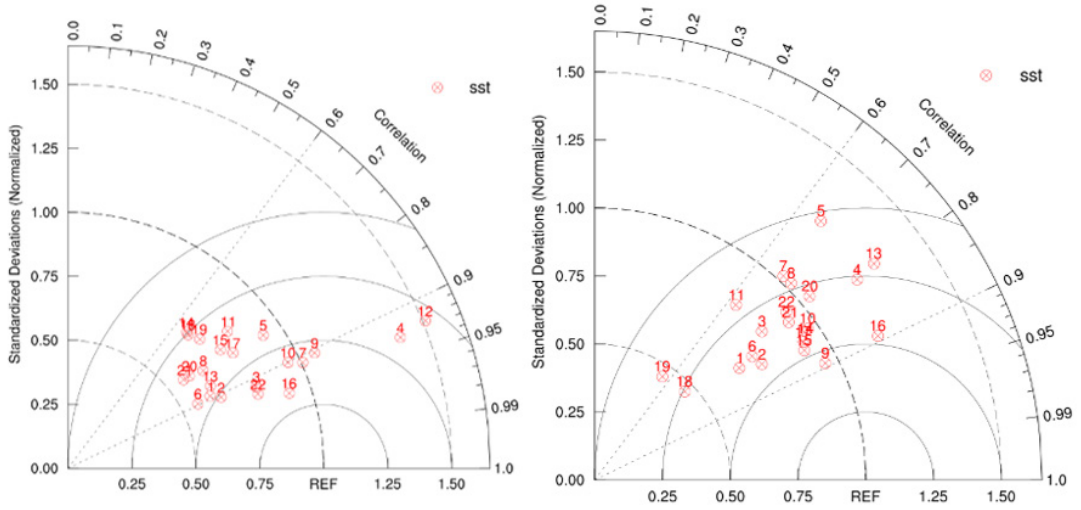


***Figure 2.7*** *Same as* ***Figure 2.2****, but for (left) DJF and (right) MAM regressed sea-surface temperature on Niño3.4 index over (15°S – 15°N, 150°E – 95°W).*

ENSO variability was examined through reviewing the Taylor diagram of SST over the tropical Pacific (15°S – 15°N, 160°E – 95°W) and the structure of the induced anticyclone over the Philippines by examining the regressed 850hPa stream function. There is a slight displacement of the anticyclone, though without a preferred direction, in most models which induces a large bias, as can be seen in the Taylor diagrams. The anticyclonic feature in models is further examined by inspection. Most models can reproduce a reasonable (fair) pattern of the warm SST anomaly over the eastern Pacific during the positive Niño3.4 period in DJF(MAM) but with some variations in magnitude (***Figure 2.6***). However, they cannot reproduce the magnitude or pattern of the Philippine Sea anticyclone. In other words, the performance of models is rather poor in capturing this feature. More details can be found in **Appendix 1.2 (DJF)** and **1.3 (MAM)**.

2.1.5 Summer monsoon variability

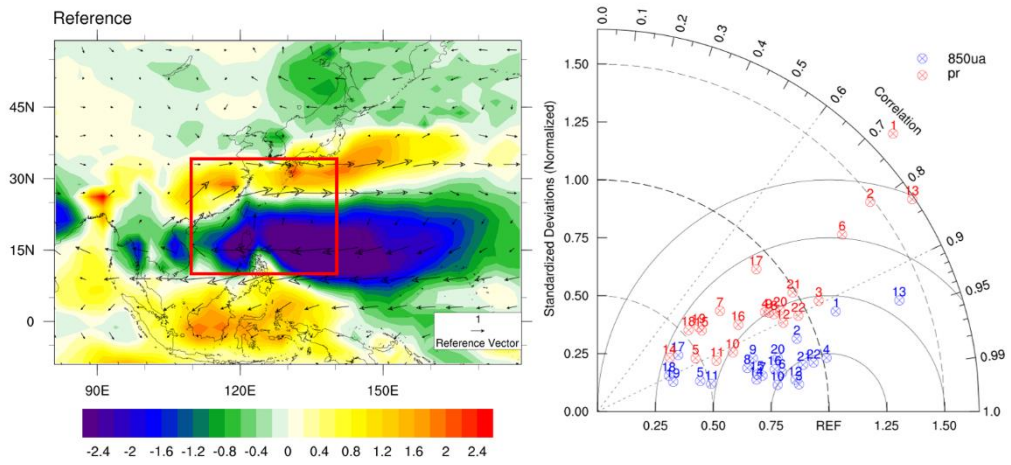


***Figure 2.8*** *(left) Regressed 850hPa wind (arrows, unit:* $ms^{-1}$*) and precipitation (shading, unit:* $mm/day$*) and (right) the Taylor diagram of 850hPa zonal wind and precipitation flux over the enclosed region by a red rectangle in (left).*

Apart from its mean circulation state, monsoon variability is also considered and it has a strong impact on the regional precipitation characteristics. To quantify the EASM variability, the index by Wang and Fan (1999) is chosen. It is defined as the difference between the 850hPa westerly anomalies averaged over 5 – 15°N, 90 – 130°E, and those over 22.5 – 32.5°N, 110 – 140°E. The regressed 850hPa wind and the precipitation of reference data and the Taylor diagram of regressed 850hPa zonal wind and precipitation are plotted in ***Figure 2.7***. GPCP Monthly Analysis Product over the same period as for the model historical runs is used here; TRMM was not used, because there is no data before 1998. To assess performance in capturing EASM variability of models, two features are considered: the northward transition of 850hPa wind from easterly to southerly and then to westerly, and the wet-dry-wet pattern of precipitation inside the area indicated by the red box in ***Figure 2.7 (left)***. As expected, more than one-third of models can reproduce such a wind pattern, because the index is calculated based on the 850hPa wind pattern solely. For the regressed precipitation, although the

performance of models has a large variation in magnitude (standard deviation bias), 19 of them can generate a pattern correlation larger than 0.6. The performance of precipitation was further examined by inspection. Details of the classification results are included in **Appendix 1.4**.

2.1.6 Winter monsoon variability

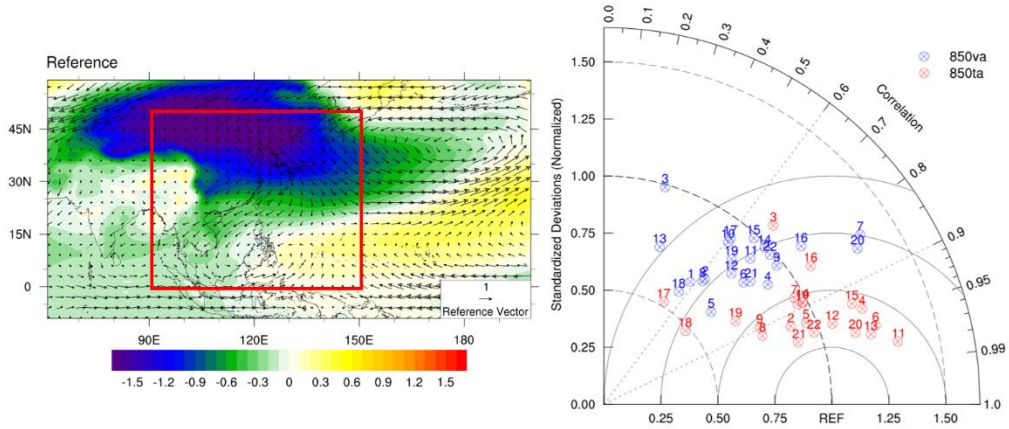


***Figure 2.9*** *(left) DJF 850hPa wind (arrows, unit: ms$^{-1}$) 850hPa temperature (shading, unit: K) regressed on EAWM index and (right) the Taylor diagram of 850hPa regressed meridional wind and temperature over the enclosed region by a red rectangle in (left) (0 – 50°N, 90 – 150°E).*

To capture the EAWM variability, the index of Wang and Chen (2013) is adapted here: $I_{EAWM} = \frac{2\times SLP_1^* - SLP_2^* - SLP_3^*}{2}$, where $SLP_1^*, SLP_2^*$ and $SLP_3^*$ indicate the normalized area-averaged sea-level pressure over 40 – 60°N, 70 – 120°E, 30 – 50°N, 140°E – 170°W and 20°S – 10°N, 110 – 160°E, respectively. This index reflects the east-west as well as north-south SLP gradients typically associated with the strength of EAWM (Wang and Chen 2013). ***Figure 2.8 (right)*** summarizes the statistics of the regression maps of 850hPa meridional wind and temperature onto this index, over 0 – 50°N, 90 – 150°E. Most models can capture the regressed temperature pattern reasonably well. For the meridional wind, although the Taylor diagram can successfully filter some

outliers (e.g. models 3, 13 & 17), further analysis via inspection is needed (see **Appendix 1.5**).

### 2.1.7 Selection results

| Index | Model | Sumer Monsoon | Winter Monsoon (V) | Summer Temperature | Winter Temperature | Summer Precipitation | ENSO(DJF) | ENSO(MAM) | EASM Variability | EAWM Variability | Overall | Score | Ranking |
|---|---|---|---|---|---|---|---|---|---|---|---|---|---|
| 1 | ACCESS1-0 | | | | | | | | | | | 3.5625 | 4 |
| 2 | ACCESS1-3 | | | | | | | | | | | 3.625 | 3 |
| 3 | bcc-csm1-1 | | | | | | | | | | | 2.6875 | 17 |
| 4 | bcc-csm1-1-m | | | | | | | | | | | 3 | 10 |
| 5 | CanESM2 | | | | | | | | | | | 2.75 | 15 |
| 6 | CMCC-CM | | | | | | | | | | | 2.8125 | 13 |
| 7 | CNRM-CM5 | | | | | | | | | | | 3.6875 | 2 |
| 8 | CSIRO-Mk3-6-0 | | | | | | | | | | | 2.5625 | 19 |
| 9 | FGOALS-g2 | | | | | | | | | | | 2.6875 | 17 |
| 10 | GFDL-CM3 | | | | | | | | | | | 3.3125 | 5 |
| 11 | GFDL-ESM2G | | | | | | | | | | | 2.875 | 11 |
| 12 | GFDL-ESM2M | | | | | | | | | | | 3.0625 | 7 |
| 13 | HadGEM2-ES | | | | | | | | | | | 3.0625 | 7 |
| 14 | IPSL-CM5A-LR | | | | | | | | | | | 2.75 | 15 |
| 15 | IPSL-CM5A-MR | | | | | | | | | | | 3.0625 | 7 |
| 16 | IPSL-CM5B-LR | | | | | | | | | | | 2.8125 | 13 |
| 17 | MIROC5 | | | | | | | | | | | 2.1875 | 20 |
| 18 | MIROC-ESM | | | | | | | | | | | 1.5625 | 22 |
| 19 | MIROC-ESM-CHEM | | | | | | | | | | | 1.6875 | 21 |
| 20 | MPI-ESM-MR | | | | | | | | | | | 3.75 | 1 |
| 21 | MRI-CGCM3 | | | | | | | | | | | 3.1875 | 6 |
| 22 | NorESM1-M | | | | | | | | | | | 2.875 | 11 |



***Table 2.3*** *The result of the model selection of CMIP5 models. The color boxes indicate the scores of models, with the highest (green) equals 4 and the lowest (red) equals 1. The overall scores are list in the second last column and the last column shows the ranking of models.*

After reviewing these simulated circulation elements, the performance of CMIP5 models is summarized in ***Table 2.3***. A score of 1 to 4 (from the worst to the best) is given to a model for a particular circulation feature. The overall score is calculated by the averaged score of all circulation elements. Four models, namely ACCESS1-3, CNRM-CM5, GFDL-CM3, and MPI-ESM-MR, were found to have the best overall performance and were chosen for dynamical downscaling. Note that ACCESS1-0 was

not selected in spite of its good performance; only one model per institute was chosen, in order to have an even sampling of model types.

### 2.2 Regional climate model configuration

The Regional Climate Model Version 4.6 (RegCM4.6) was adopted for dynamical downscaling in this study. It is a hydrostatic model with a staggered Arakawa B-grid system, developed by the International Centre for Theoretical Physics (ICTP, Giorgi et al. 2012). RegCM4 and its previous versions have been used for the numerous climate projections over various regions in the world, including the Coordinated Regional Downscaling Experiment (CORDEX) (https://cordex.org/) (Giorgi et al. 2009, Gu et al. 2012, Oh et al. 2014, Lui et al. 2019a).

Here the RegCM4 was integrated with a horizontal resolution 25 km × 25 km, with 18 sigma vertical levels. Three cumulus schemes, the Kuo-type scheme (Anthes 1977), the Grell scheme (1993), and the MIT scheme (Emanuel 1991; Emanuel and Živković-Rothman 1999), can be used. The MIT scheme (Emmanuel scheme) is chosen over the whole domain, based on the results of Li et al. (2016) and Lui et al. (2019a), which indicate that the scheme can produce the most reasonable precipitation at a variety of timescales over Southern China. Simulated data of RegCM4 were stored with a time-interval of 6-hourly for atmospheric variables and hourly for surface flux, including precipitation. The configuration of RegCM4 is given in ***Table 2.4***.

| | |
|---|---|
| **Horizontal Grids** | 150 zonal × 180 meridional, ds = 25.0 km, centered at (20°N, 120°E) |
| **Vertical Levels** | 18 sigma levels |

| | |
|---|---|
| **Cumulus Convective Scheme** | Emanuel scheme, for both land and sea |
| **Boundary-Layer Scheme** | Holtslag PBL (Holtslag et al. 1990) |
| **Ocean Flux Scheme** | Zeng et al. 1998 |
| **Land Surface Processes** | CLM4.5 |
| **Simulation Period** | Historical: Jan 1979 to Dec 2003 (25 years)<br>Future (RCP8.5): Jan 2050 to Dec 2099 (50 years) |
| **Buffer Zone** | 12 grids |

***Table 2.4*** *RegCM4 configuration used in this study.*

### 2.3 Experiment design

The model was integrated during the "historical" and "future" eras. For the historical (future), the simulation period was from Jan 1979 (2050) to Dec 2003 (2099). Future projections were obtained according to the RCP8.5, which is the "business-as-usual" scenario suggested by IPCC AR5.

The performance of RegCM4 in capturing the present-day climate was first evaluated, by downscaling 6-hourly ICBC data from ERA-interim. The run covered the period of Jan 1979 to Dec 2003. Results were compared to the reanalysis or observational data to assess any RCM bias. Apart from ERA-interim and TRMM, station-based APHRODITE (Asian Precipitation - Highly-Resolved Observational Data Integration Towards Evaluation) daily rainfall data (Yatagai et al. 2012) with the period 1979 – 2003 were also used to evaluate the performance of RegCM4. Chen et al. (2013) reported that TRMM tends to overestimate daily precipitation over Southern China. Furthermore, historical simulations using the four selected GCMs were compared with

products from the corresponding GCMs. The naming and period of all simulations are shown in ***Table 2.5***. Finally, simulations forced by GCMs within the same period were averaged to give the multi-model ensembles (MME) mean, so as to increase the reliability of climate projections (Tebaldi and Knutti 2007). The difference between two MME averages for the historical and future simulations were examined, in order to infer climate change signals over Southern China.

| **Acronyms** | **ICBC** | **Simulation Period** |
|---|---|---|
| **RegCM4_EA** | ERA-interim | 1979 – 2003 |
| **RegCM4_AC** | ACCESS1-3 | 1979 – 2003 (HIST) |
| | | 2050 – 2099 (RCP8.5) |
| **RegCM4_CN** | CNRM-CM5 | 1979 – 2003 (HIST) |
| | | 2050 – 2099 (RCP8.5) |
| **RegCM4_GF** | GFDL-CM3 | 1979 – 2003 (HIST) |
| | | 2050 – 2099 (RCP8.5) |
| **RegCM4_MP** | MPI-ESM-MR | 1979 – 2003 (HIST) |
| | | 2050 – 2099 (RCP8.5) |

***Table 2.5*** *The short name, ICBC, and simulation period of all RegCM4 simulations conducted in this project.*

### 2.4 Moisture budget analysis

Moisture budget analysis is commonly used in the attribution of the sources of and the changes in precipitation over a domain under certain climate scenarios. Specifically, long-term mean precipitation P, evaporation E and vertically integrated moisture flux $\vec{Q}$, and are related by

$$\bar{P} = \bar{E} - \overline{\nabla \cdot \vec{Q}} \quad (2.1).$$

$\vec{Q}$ is defined by $\vec{Q} = \frac{1}{g}\int_0^{p_s} q\boldsymbol{V}dp$, the vertically integrated product of specific humidity $q$ and wind vector $\boldsymbol{V}$, where $p_s$ is surface pressure, g is the gravitational acceleration, and overbar denotes the long-term mean. Equation 2.1 illustrates that the change in mean state precipitation should be balanced by the total changes in evaporation and vertically integrated moisture flux convergence.

Moisture budget analysis was also used in IPCC AR5 to understand increased mean precipitation over monsoon regions and its relationship with change in evaporation and moisture transport in the future climate. AR5 suggests that the growing trend of global precipitation in monsoon regions is generally due to the increasing specific humidity. From CMIP3 and CMIP5 studies, numerical models suggested a weakened low-level circulation, but with increased specific humidity. ***Figure 2.10*** indicates that the mean precipitation is increasing under all suggested RCPs over monsoon regions, with stronger growth for warmer scenarios. Evaporation and moisture flux convergence also increase, and the latter has a more comparable magnitude with precipitation. Vertically integrated wind convergence $-\int_0^{p_s} \nabla \cdot \boldsymbol{V}dp$ is however decreasing in all the scenarios, which suggests that increase in $-\nabla \cdot \vec{Q}$ is from the enhanced specific humidity $q$. The total increase in evaporation and specific humidity outweighs the weakening circulation and causes a significant growth in precipitation. Similar analysis techniques are used to examine changes in precipitation at various timescales.

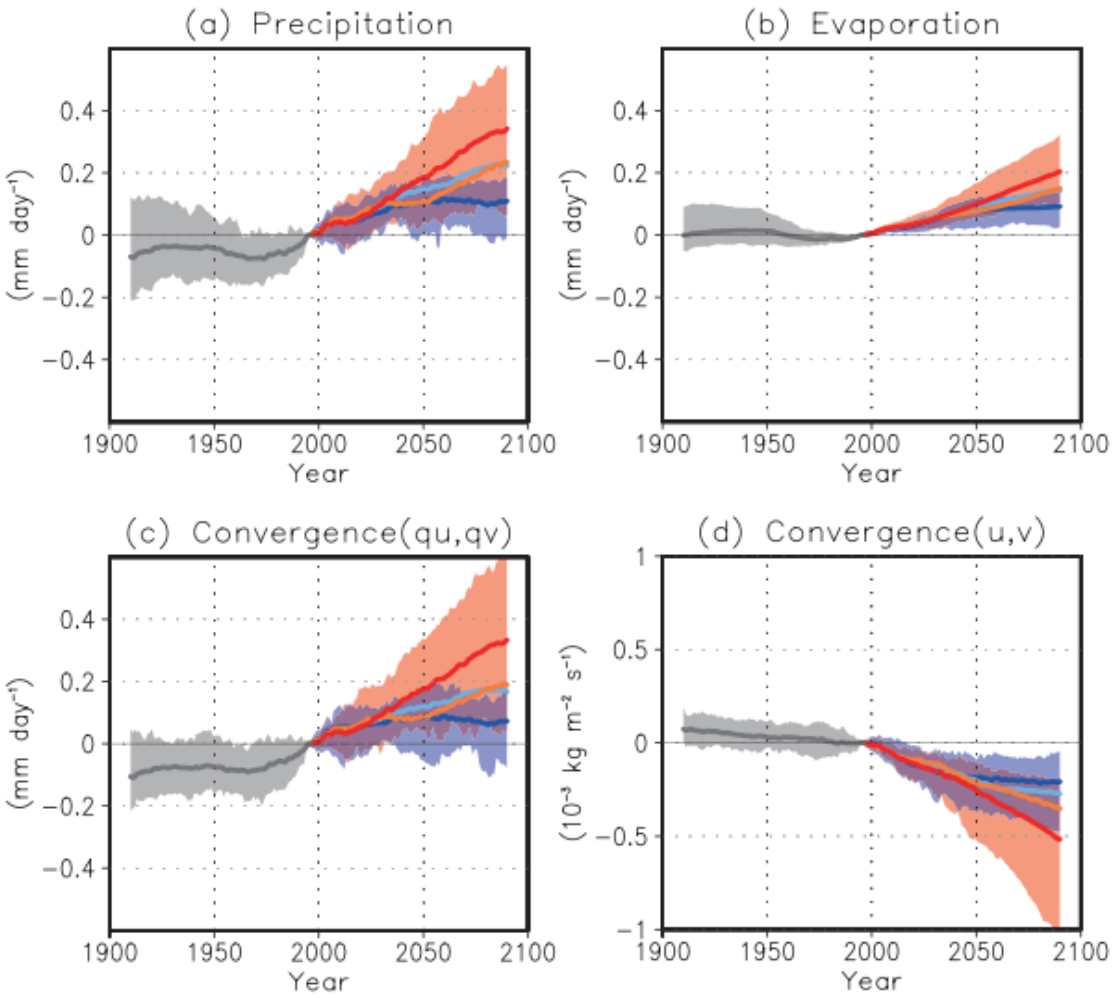


***Figure 2.10*** *Simulated time-series of area-averaged anomalous (a) precipitation, (b) evaporation, (c) vertically integrated moisture flux convergence (below 500hPa) and (d) wind convergence based on CMIP5 models in historical climate (grey), and under climate scenarios RCP2.6 (dark blue), RCP4.5 (light blue), RCP6.0 (orange) and RCP8.5 (red) over monsoon region. Reprinted from the IPCC AR5 WGI Figure 14.2 (Christensen et al. 2013).*

# 3 Performance of RegCM4 and Dynamical Downscaling

This chapter focuses on the evaluation of RegCM4 in reproducing the mean seasonal climate over the domain of interest, including low-level temperature, wind, and precipitation. The outputs of RegCM4_EA are compared with ERA-interim for temperature and wind and with TRMM and APHRODITE for precipitation. The differences between RegCM4_EA and the raw reanalysis/observational data can be used to indicate any bias in RegCM4. After that, the downscaled outputs of the selected GCMs are compared with their parent models, to determine the ability of RegCM4 in retaining major features from GCMs after applying dynamical downscaling.

## 3.1 RegCM4 performance

### 3.1.1 Low-level temperature and wind

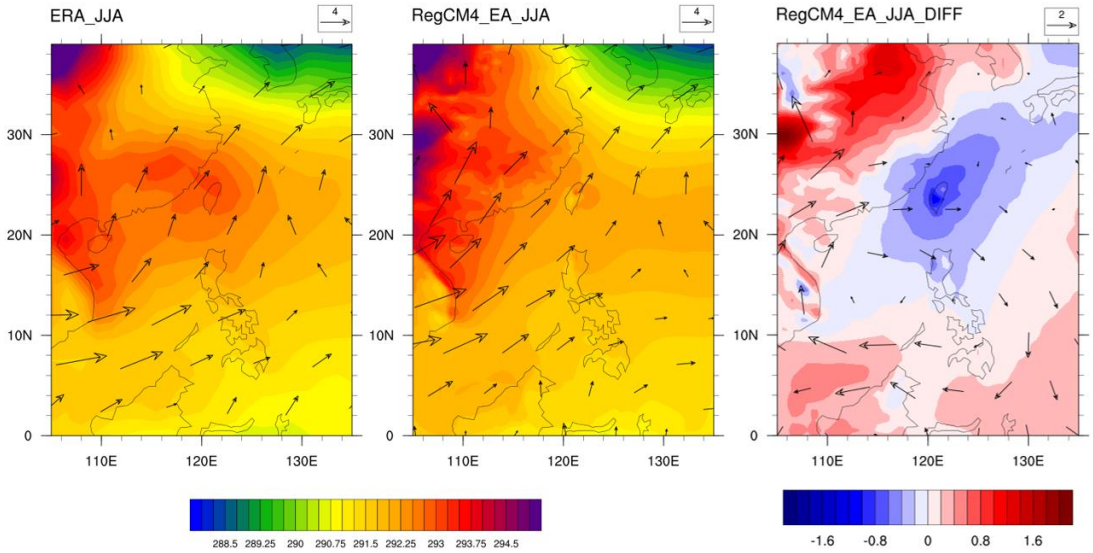


***Figure 3.1*** *JJA mean 850hPa wind (arrows, units: ms-1) and temperature (shading, units: K) from (left) ERA-interim, (middle) RegCM4_EA and (right) RegCM4_EA minus ERA-interim during 1979 – 2003 respectively.*

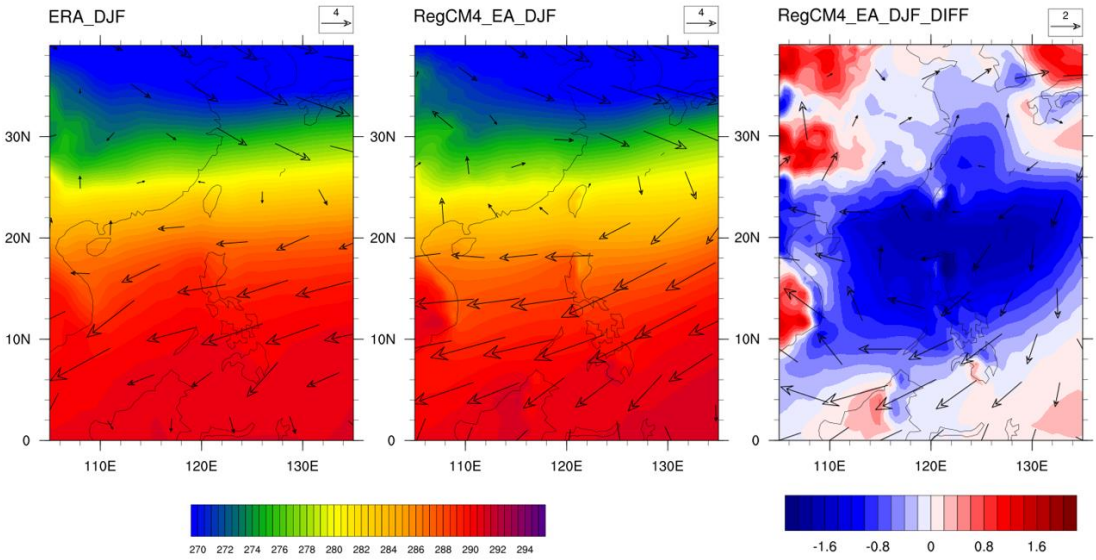


***Figure 3.2*** *Same as* ***Figure 3.1*** *but for DJF.*

***Figures 3.1 – 3.2*** show the mean 850hPa temperature and wind from ERA-interim and those from RegCM4_EA, for JJA and DJF. RegCM4 tends to produce warmer temperature over land for all seasons (including MAM and SON, not shown). For boreal winter (DJF), a warm bias of about 2°C is found. A cold bias over the oceanic area north of 10°N is seen throughout the whole year, with a magnitude comparable to that of the warm bias. The model also tends to produce a northerly or northeasterly bias in the low levels over the eastern and southern parts of the domain, except for summer (JJA). At the same time, a slight southerly bias is found near Indochina, resulting in an anticyclonic circulation in the low levels. The magnitude of wind bias is strong over the ocean, reaching about 50% of the original wind speed. A noticeable difference between ERA-interim products and RegCM4 outputs in the wind is found near the western boundary of the domain. Further inspection showed that this is related to the slight difference in the elevation of the 850hPa level, which intersects with the local topographic feature there. Overall, RegCM4 can give low-level circulation and

temperature that resemble reanalysis in different seasons. Most low-level wind branches, such as the southwesterly onshore wind over Southern China in JJA and the strong northwesterly to northeasterly wind over the whole model domain in DJF, are reasonably reproduced.

### 3.1.2 Precipitation

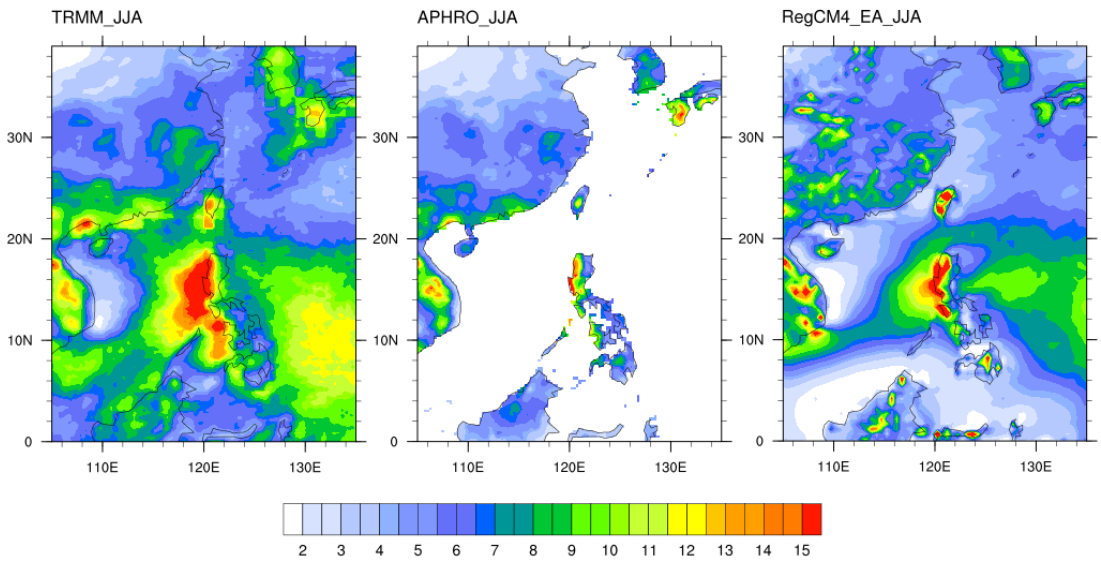


***Figure 3.3*** *JJA mean precipitation (units: mm/day) from (left) TRMM 3B42 (1998 – 2018), (middle) APHRODITE (1979 – 2003) and (right) RegCM4_EA.*

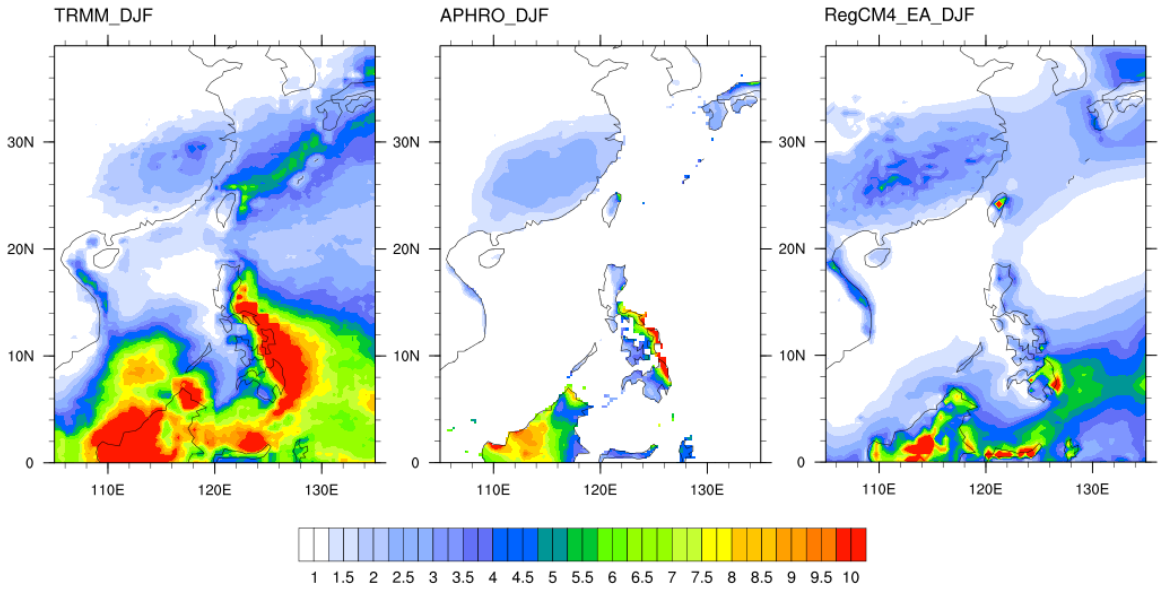


***Figure 3.4*** *Same as* ***Figure 3.3*** *but for DJF.*

The JJA and DJF mean precipitation from various reference datasets and RegCM4_EA are given in ***Figures 3.3*** and ***3.4***. TRMM (1998 – 2018) and APHRODITE (1979 – 2003) give patterns consistent with each other, but with the former having slightly stronger magnitudes. Model rainfall is now compared with APHRODITE (TRMM) over continental (oceanic) areas. For precipitation over land, RegCM4 tends to reproduce a wetter climate over Southern China during MAM (not shown) and DJF (***Figure 3.4***), with a mean rainfall bias of about 20%. For SON (not shown) and JJA (***Figure 3.3***), there is a wet bias near the mountainous area in 25 – 30°N, 100 – 115°E. It is noteworthy that, during JJA, the rain belt near coastal Southern China is displaced northward by about 2 – 3° in the model; this feature has a magnitude that is comparable to the one more along the coast in APHRODITE. Precipitation over land is generally well simulated. Note that the model precipitation features are sensitive to topography, leading to noisier patterns than those from both TRMM and APHRODITE over the same locations.

Over SCS, the precipitation is too weak in RegCM4_EA during the dry seasons (SON and DJF). There is a significant dry bias in the ocean in all seasons, which may be related to the low-level anticyclone mentioned in section 3.1.1. Overall, it is seen that compared to precipitation over land, RegCM4 performance is less satisfactory in the capturing rainfall over the ocean. In view of its performance, in this study, we focus on precipitation characteristics from RegCM4 over land only.

### 3.1.3 Maximum consecutive dry days

The dry season is an important feature of the hydrological characteristics of Southern China. To quantify it, the annual number of maximum consecutive dry days (CDD) was examined. CDD was calculated by counting the maximum consecutive days with daily precipitation less than 1.0 mm/day in one year, then taking the average over the whole period. For the purpose of computing CDD, the annual period starts from 1$^{st}$ June to 31$^{st}$ May next year to prevent cutting off the dry season in Southern China (SON and DJF). Therefore, there are a total of 24 (49) annual periods in the historical (future) simulations. ***Figure 3.5*** shows plots of CDD from TRMM, APHRODITE, and RegCM4_EA. The average CDD over Southern China is about 25 to 40 days. TRMM has much longer CDD than APHRODITE and RegCM4_EA. The failure of TRMM in reproducing a reasonable number of CDD over Southern China is reported in Huang et al. (2017). CDD in RegCM4_EA is comparable to that in APHRODITE, except for regions over Southwest China.

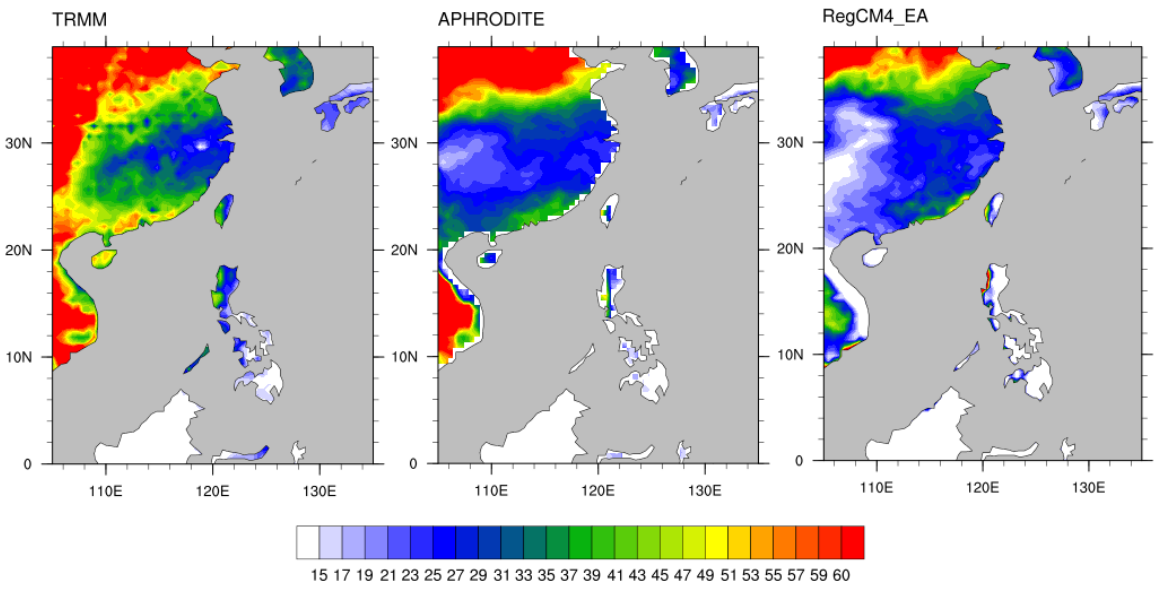


***Figure 3.5*** *Mean annual maximum consecutive dry days (units: days) for (left) TRMM, (middle) APHRODITE and (right) RegCM4_EA.*

### 3.1.4 Diurnal rainfall

For diurnal rainfall (DR), we focus on JJA because the magnitude of DR is significant in JJA only over Southern China. ***Figures 3.6*** and ***3.7*** show the DR cycle from TRMM 3B42 3-hourly data and RegCM4_EA respectively. DR in TRMM (***Figure 3.6***) is mainly dominated by two modes within the domain of interest, one related to continental rainfall and the other with oceanic rainfall. Continental rainfall starts in the afternoon around 14:00 and reaches a peak at 17:00 local time (LT), and has a strong intensity over coastal Southern China. Oceanic rainfall has the strongest signal over SCS. It starts in the early morning (05:00 LT), reaches a peak in the afternoon, and is suppressed in the evening (17:00 LT). The magnitude of the morning rainfall is much weaker than that of the afternoon rainfall. Features of these two modes of DR are consistent with previous studies (Dai et al. 2006, Chen et al. 2009, Chen et al, 2016, Lui et al. 2019a). Compared to TRMM, the cycles of both DR modes in RegCM4 occur

three-hour earlier (***Figure 3.7***). The time bias of the DR cycle was also reported by Giorgi et al. (2012). The reason for that is due to the earlier triggering of convective cumulus schemes, regardless of the scheme chosen. Regarding its magnitude, the afternoon rainfall is stronger in RegCM4_EA but there is no significant difference in the morning rainfall.

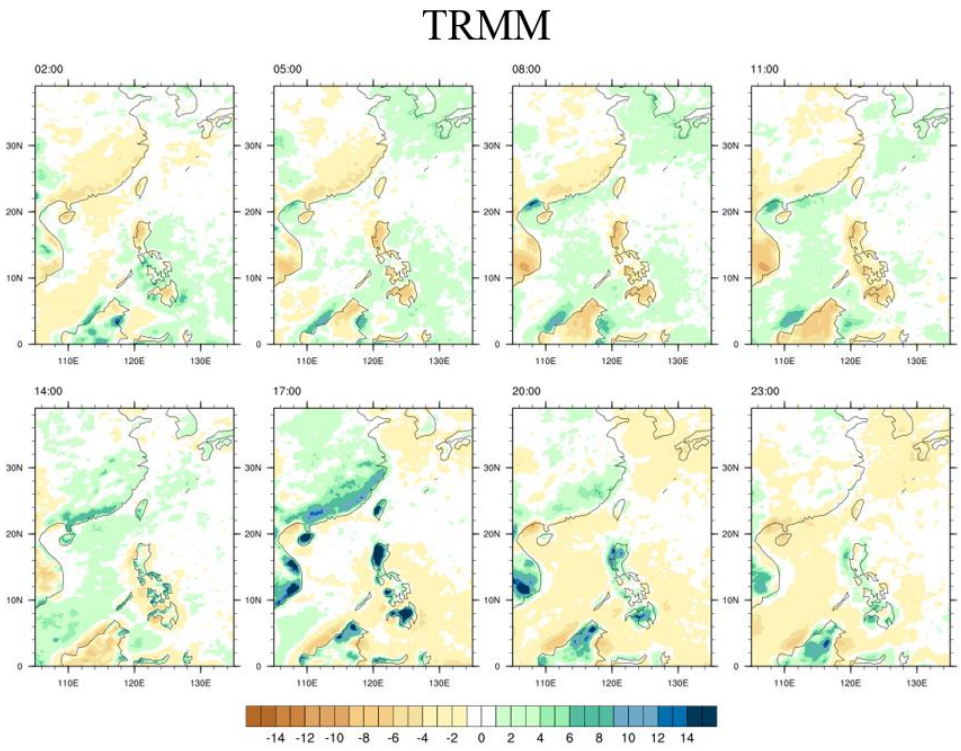


***Figure 3.6*** *3-hourly JJA precipitation deviation from the daily mean (units: mm/day) from TRMM with the period 1998 – 2017. The local time (UTC +8) is indicated at the top-left of each panel.*

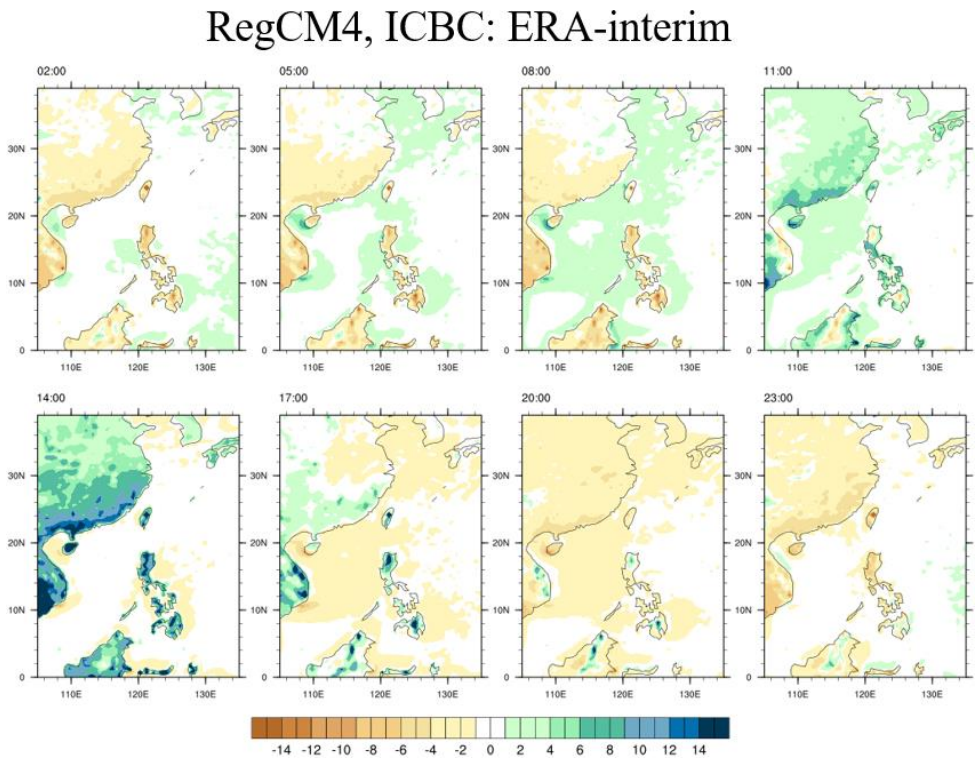


***Figure 3.7*** *Same as* ***Figure 3.6*** *but for RegCM4_EA. The 3-hourly data is computed by averaging the values from the adjacent two hours of the plotted LT.*

### 3.2 Performance of dynamical downscaling using RegCM4

To ensure the dynamical downscaling can retain general features simulated by the GCMs, downscaled products are compared with those from the parent GCMs. We first evaluate the performance of low-level temperature and wind. Downscaled precipitation is also evaluated, in order to determine the credence of simulated hydrological events and their future projections.

#### 3.2.1 Low-level temperature and wind

***Figures 3.8 – 3.11*** give the Taylor diagrams for seasonal mean 850hPa temperature and winds by comparing downscaled results with corresponding raw GCM products, for both historical (1979 – 2003) and future (2050 – 2099) simulations. In general, it

can be inferred that RegCM4 can reproduce well the 850hPa temperature (green circles) and zonal wind (red circles). However, this is not the case for the 850hPa meridional wind (blue circles); there is a good performance in MAM (***Figure 3.8***) and DJF (***Figure 3.11)***, but the matching is rather poor in JJA (***Figure 3.9***). For ACCESS1-3, downscaling results in the v-wind seem to deviate from its parent GCM in SON as well (***Figure 3.10***).

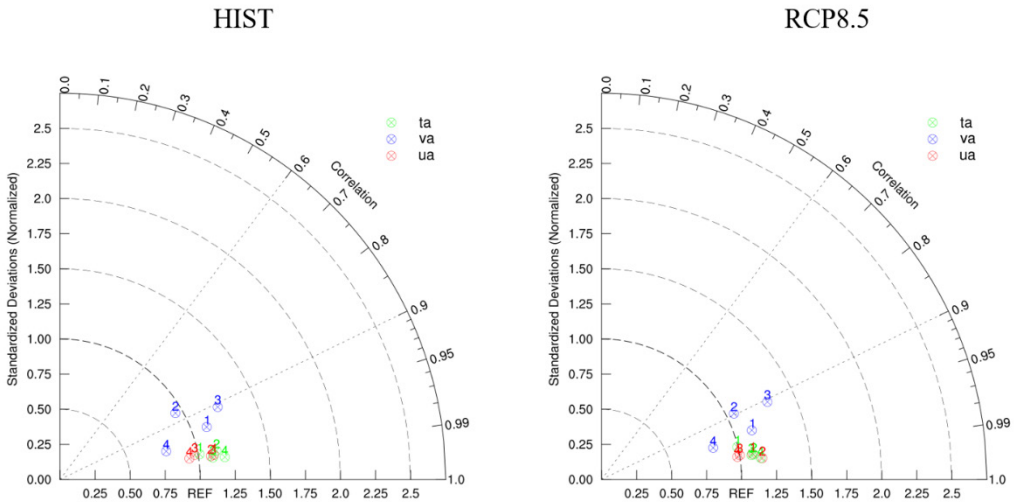


***Figure 3.8*** *Taylor diagrams examining the performance of dynamical downscaling for MAM mean 850hPa (green) temperature, meridional component (blue) and zonal component (red) of wind for (left) historical (1979 – 2003) and (right) RCP8.5 (2050 – 2099) simulation. Number on colored circles represents the RegCM4 downscaled products, with 1: ACCESS1-3, 2: CNRM-CM3, 3: GFDL-CM3, and 4: MPI-ESM-MR. REF refers to the corresponding raw GCMs products. See text for details.*

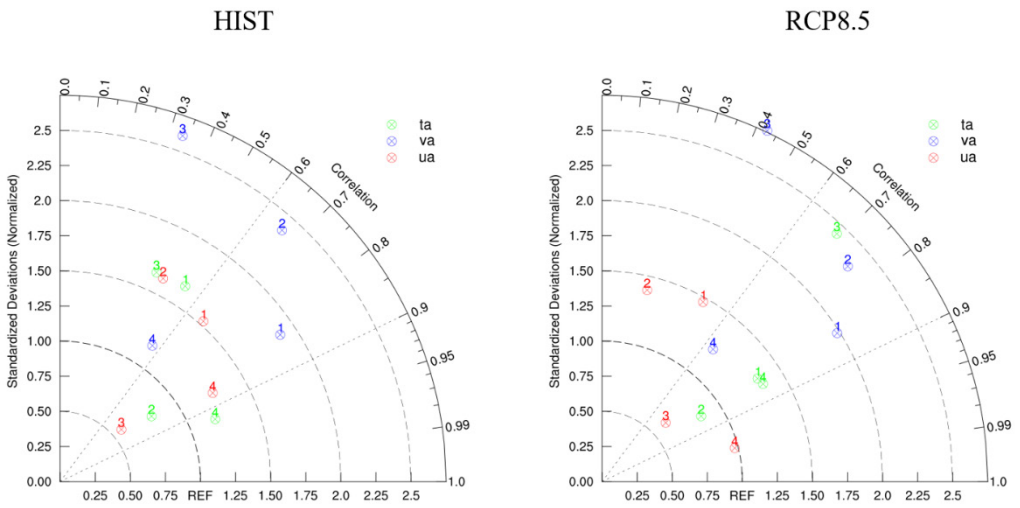


***Figure 3.9*** *Same as* ***Figure 3.8*** *but for JJA.*

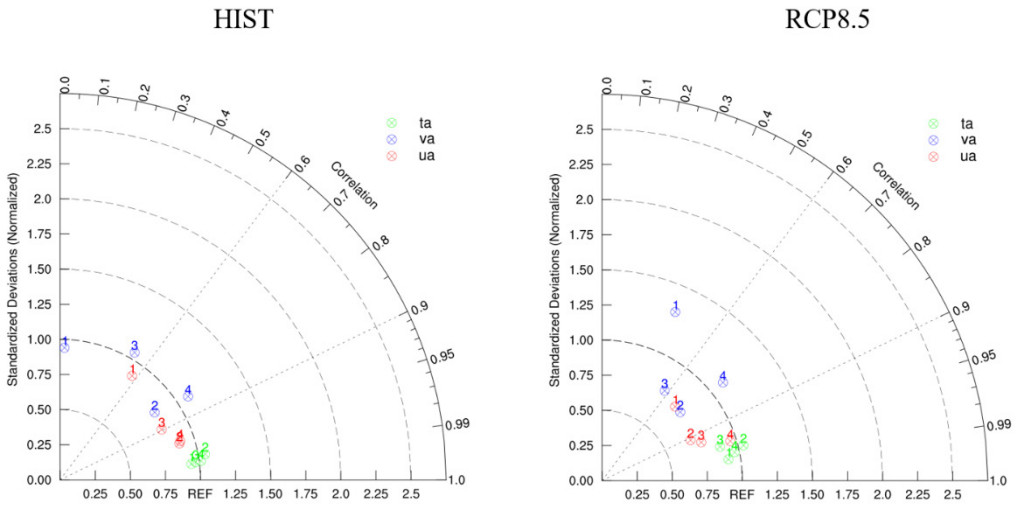


***Figure 3.10*** *Same as* ***Figure 3.8*** *but for SON.*

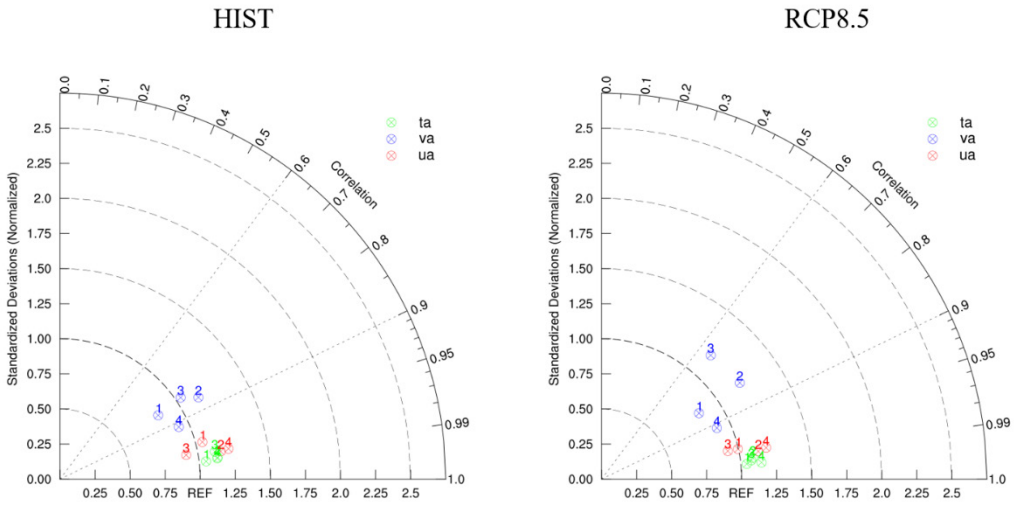


***Figure 3.11*** *Same as* ***Figure 3.8*** *but for DJF.*

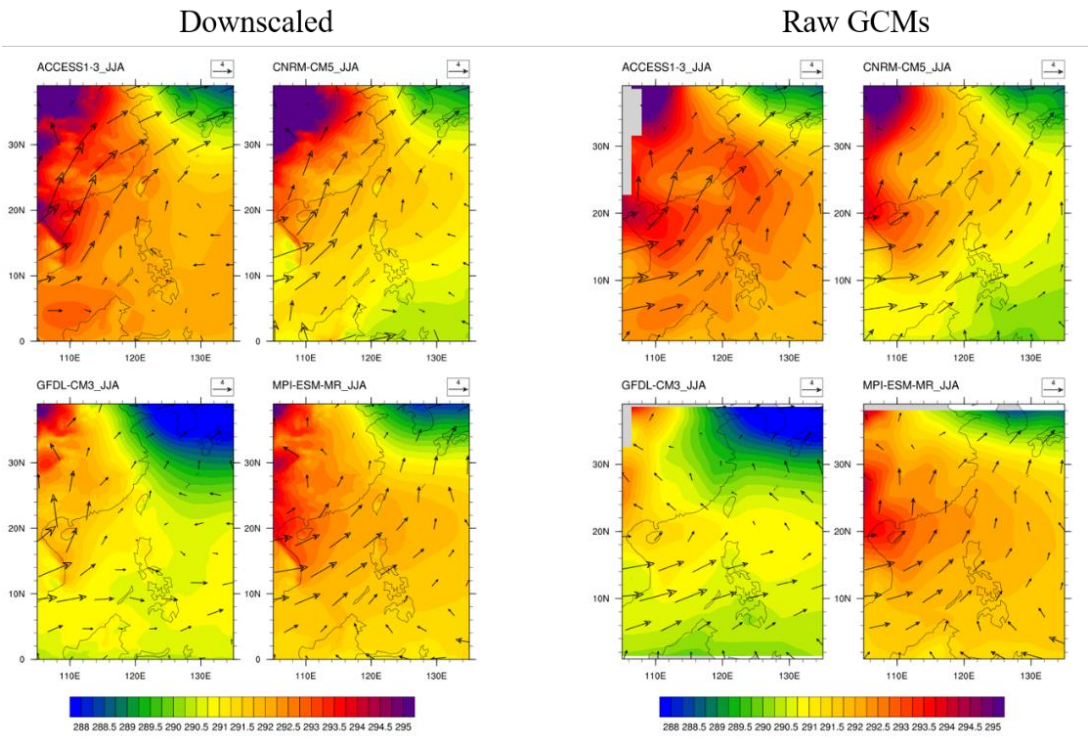


***Figure 3.12*** *JJA historical mean (1979 – 2003) 850hPa temperature (shading, units: K) and wind (arrows, units: ms$^{-1}$) from (left panel) RegCM4 downscaling and (right panel) raw GCMs.*

***Figure 3.12*** gives the dynamically downscaled and raw GCM results for JJA mean 850hPa temperature and wind for historical and future simulations. It can be seen that

temperature patterns from RegCM4 and the parent GCMs match each other rather well, with much inland area being warmer and the ocean cooler. In raw GCMs, the temperature patterns are rather smooth in all models, decreasing gradually from the warmer continent to the cooler ocean. However, the temperature patterns over land are much more complicated in RegCM4, with some local extrema over locations with higher elevation or located at the leeward side. It results in mismatches in spatial patterns and standardized deviations shown by the Taylor diagrams (see ***Figure 3.9***). Likewise, the JJA season southwesterly wind branch is displaced to the northwest in RegCM4_AC and RegCM4_CN. The wind starts turning from westerly to southerly in the western part of the model domain, i.e. from about 115°E in GCMs to 110°E in RegCM4. RegCM4_MP can retain most features from its parent GCM, except the zonal wind being stronger near SCS and Southern China. RegCM4_GF gives a strong wind branch over continental Southern China, which is not seen in the parent GCM results.

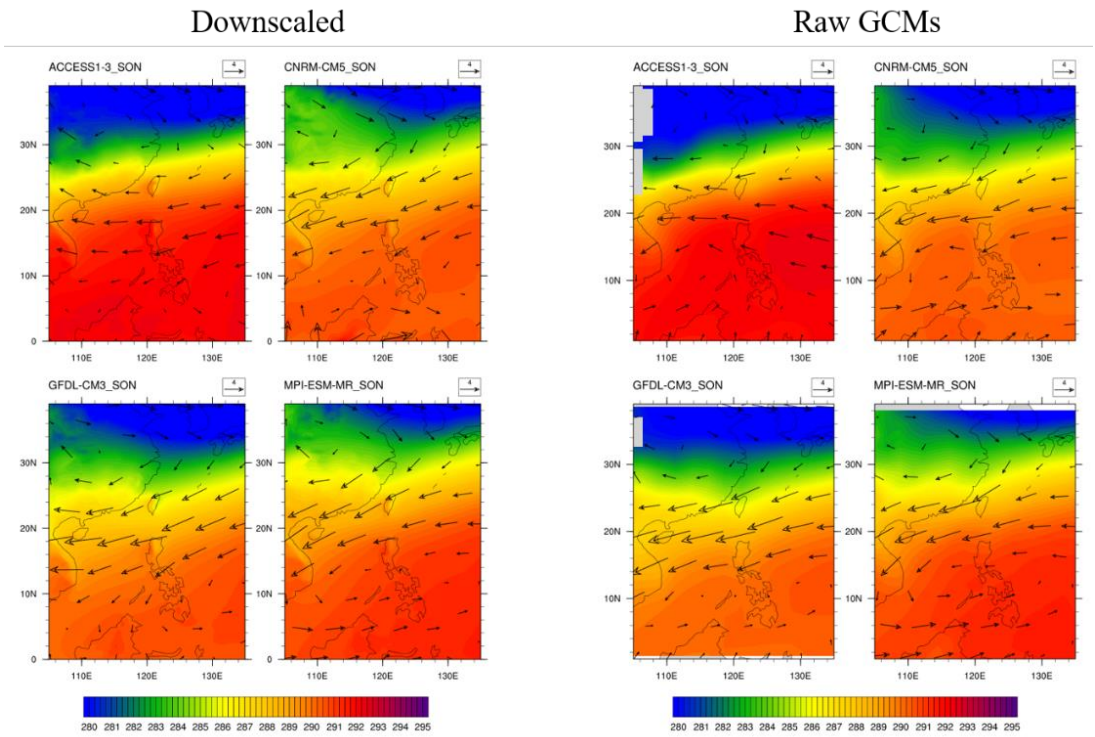


***Figure 3.13*** *Same as* ***Figure 3.10*** *but for SON.*

For SON, low-level temperature from all GCMs is well reproduced in RegCM4 (***Figure 3.13***). From the Taylor diagram (***Figure 3.10***), the downscaled variable and its standard deviation are close to those from the parent GCMs. The zonal wind is well reproduced, with the easterly wind branch from 10°N – 30°N being captured after downscaling. The magnitudes of the meridional component of winds are small over the whole domain, which causes the parameters presented by the Taylor diagrams to be sensitive to small biases, especially for ACCESS1-3. The performance of downscaling ACCESS1-3 in SON is further evaluated.

For MAM and DJF, the performance is satisfactory. No big difference can be found between the downscaled products and the raw GCMs. Most prominent low-level features, such as the southwesterly over Southern China in MAM, the winter monsoon in the whole domain, and temperature patterns, are well reproduced by RegCM4 with similar magnitudes (not shown).

### 3.2.2 Precipitation

Unlike temperature and wind, precipitation is not a primary variable provided as ICBC. Precipitation characteristics thus rely on the internal dynamics and physics of the RCM. To ascertain whether the RegCM4 results are reasonable, precipitation outputs are compared with those from the GCMs.

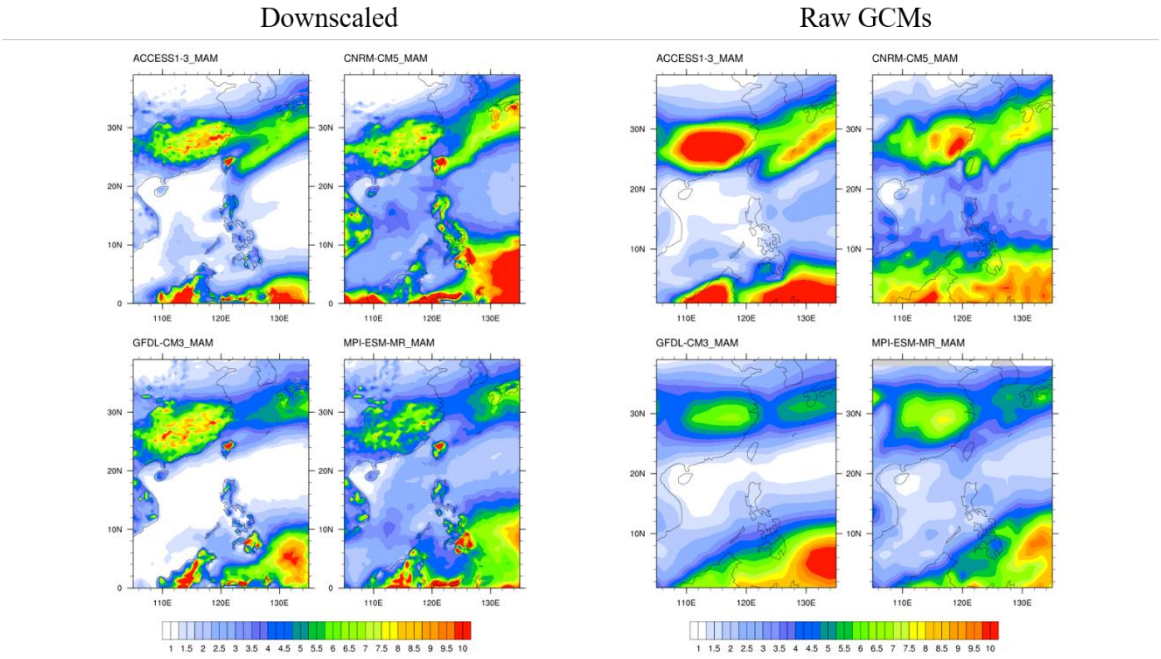


***Figure 3.14*** *Same as* ***Figure 3.12*** *but for MAM precipitation (units: mm/day).*

***Figures 3.14 – 3.17*** show the seasonal mean precipitation from the selected GCMs and their downscaled outputs in the historical simulations. For MAM, RegCM4 can reproduce most features in the mean precipitation, especially those over land (***Figure 3.14***). For GFDL-CM3 and MPI-ESM-MR, mean precipitation over Southern China is displaced to more southern locations. Such a shift results in stronger inter-model consensus in the location of the wet area. RegCM4 also reduces the MAM rainfall amount as compared to ACCESS1-3; on the other hand, there is more rain in the RCM compared to GFDL-CM3. The downscaled products also resemble the APHRODITE

more in terms of their spatial patterns. In a sense, downscaling using RegCM4 can reduce the precipitation bias from parent GCMs over Southern China in MAM.

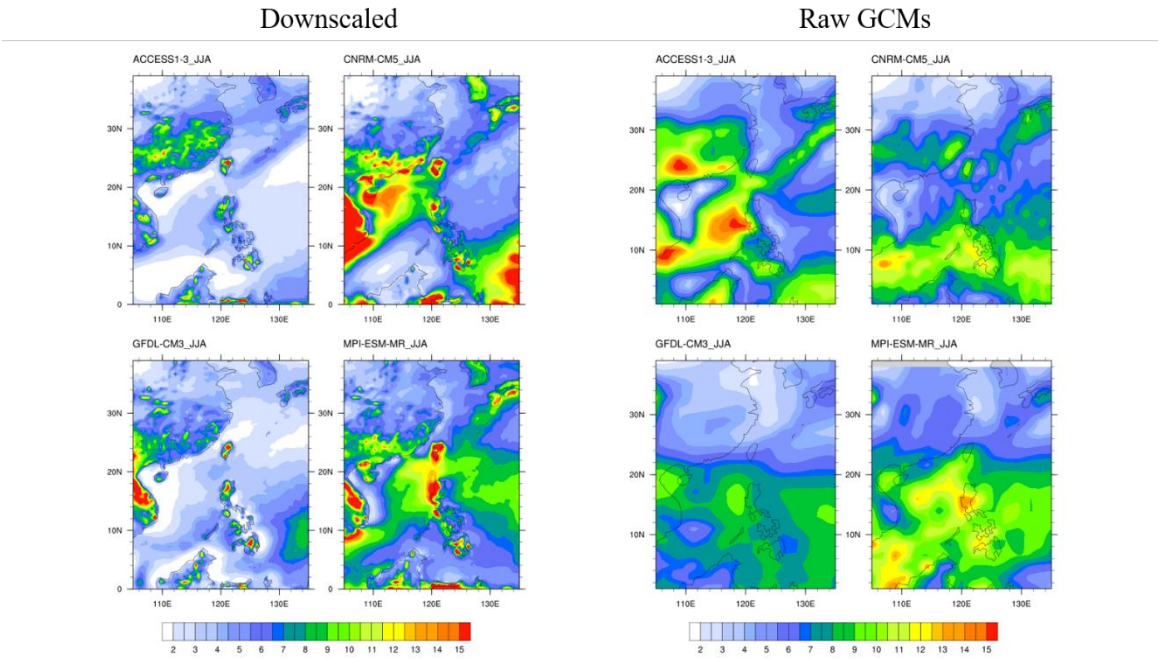


***Figure 3.15*** *Same as* ***Figure 3.14*** *but for JJA.*

For JJA, the precipitation patterns can be very different compared with those from the GCMs (***Figure 3.15***). For ACCESS1-3 and MPI-ESM-MR, downscaled results over land are similar to their parent GCMs. In RegCM4_CN, precipitation is enhanced, such that simulated rainfall resembles APHRODITE more compared to the parent GCM. The rain belt over Southern China is also shifted southward to more coastal locations. For GFDL-CM3, the wet zone over coastal Southern China in the parent GCM now disappears after downscaling. This raises the question of whether the inclusion of downscaled GFDL-CM3 in JJA is reasonable. Owing to the inconsistencies between downscaled and raw GCM low-level temperature and wind, downscaled GFDL-CM3 results will be discarded when examining the JJA climate in this study.

Over the oceanic region, it is noticed that RegCM4 cannot reproduce the rainfall from

raw GCMs in JJA. In particular, SCS becomes much drier after downscaling for all models. The above suggests that the boreal summer precipitation over the ocean in this model might not be reliable.

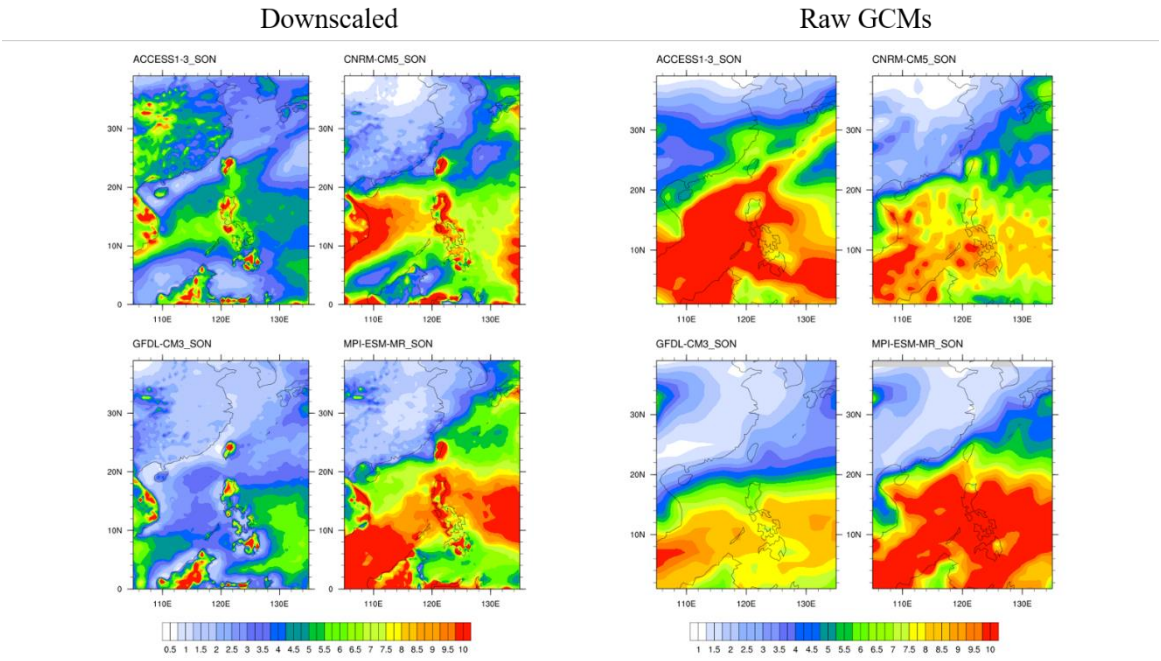


***Figure 3.16*** *Same as* ***Figure 3.14*** *but for SON.*

***Figure 3.16*** shows the SON rainfall results. For precipitation over land, features from CNRM-CM5, GFDL-CM3, and MPI-ESM-MR are well reproduced by the regional model. For ACCESS1-3, which is the wettest among all models, RegCM4_AC produces in even stronger wet biases, making the downscaled SON rainfall deviates even more from APHRODITE. Thus, for SON, RegCM4_AC is discarded due to its abnormally wet climate over land, and also its poor performance in reproducing the low-level meridional wind (see ***Figure 3.10***). Similar to JJA, RegCM4 also performs inadequately in simulating precipitation over the ocean, irrespectively of the parent GCM. The inter-model consensus in the oceanic precipitation pattern is also rather poor.

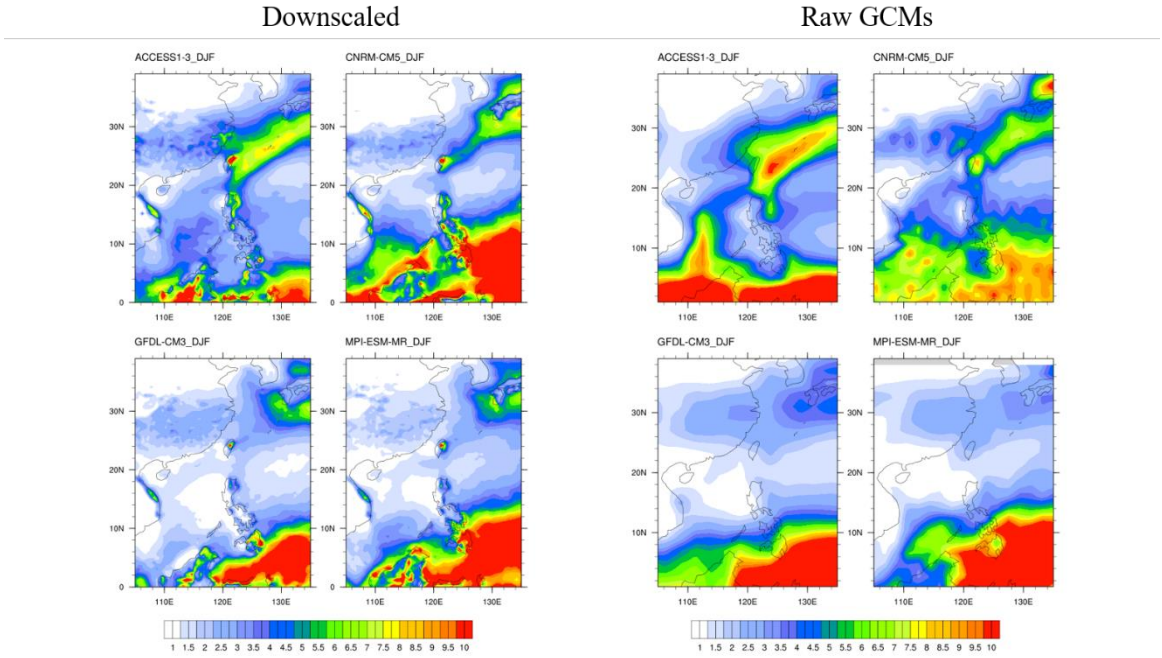


***Figure 3.17*** *Same as* ***Figure 3.14*** *but for DJF.*

Finally, precipitation in DJF over land is well reproduced, in terms of both its pattern and magnitude (***Figure 3.17***). For GFDL-CM3 and MPI-ESM-MR, rainfall patterns are slightly shifted to the south, with features more comparable to APHRODITE. Over the ocean, RegCM4 precipitation is still drier than the raw GCM outputs. Although its performance is better than that in JJA or SON, the inter-model consensus for rainfall over SCS is still weak.

The reason why RegCM4 has a poorer performance for precipitation over the ocean than that over land might be due to the difference in moisture transport over the ocean versus land. Precipitation over the ocean can be more sensitive to the background specific humidity. In our selected models, seasonal mean 850hPa wind over SCS deviates among models. For example, RegCM4_CN and RegCM4_MP reproduce stronger low-level zonal wind and cyclonic vorticity; the resulting moisture transport and perhaps Ekman pumping of moisture within the planetary boundary layer might

be conducive to stronger convection and precipitation; on the other hand, such features are not found RegCM4_AC and RegCM4_GF (see ***Figure 3.13*** and ***Figure 3.16***). As a result, the models give weak inter-model consensus in the precipitation over the ocean.

### 3.2.3 Summarized dynamical downscaling results

Overall, it is found that RegCM4 can retain the major feature of seasonal mean low-level temperature, wind, and precipitation over the continental area from the parent GCMs. The results of test simulations (RegCM4_EA) indicate that wet and warm biases are found in all seasons except for JJA. The rain belt in JJA over coastal Southern China is also shifted 2 – 3° northward. However, in comparison, the precipitation over the ocean is poorly captured than that over land, with a dry bias over SCS being found in all seasons.

About the dynamical downscaling for the four selected GCMs, namely ACCESS1-3, CNRM-CM5, GFDL-CM3, and MPI-ESM-MR, low-level temperature and wind are generally well captured, except for GFDL-CM3 in JJA and also the meridional wind for ACCESS1-3 in SON. GFDL-CM3 (ACCESS1-3) also fails to reproduce reasonable features and even increases the biases of precipitation over land in JJA (SON) after downscaling. The inter-model consensus in precipitation over SCS is poor in JJA, SON, and DJF. This indicates that the oceanic precipitation might be too sensitive to ICBC and is unable to be reasonably simulated based on the implemented model physics and/or schemes in RegCM4.6 under a horizontal resolution of 25km. After reviewing the performance of RegCM4 and dynamical downscaling of the four selected models, it was decided to exclude RegCM4_GF (RegCM4_AC) from the MME mean in analyses of the JJA (SON) precipitation characteristics and focus on the

analysis of continental rainfall only.

# 4 Seasonal Mean Climate Projection

Analyses of the differences between MME_HIST and MME_RCP8.5 in the seasonal mean climate are conducted in this chapter, in order to evaluate the projected seasonal climate change in low-level temperature, wind, and precipitation characteristics over Southern China. Attribution of the changes in precipitation characteristics is also included to understand the potential causes.

## 4.1 Changes in mean state climate

***Figure 4.1*** shows the difference in the multi-model ensemble (MME) average seasonal mean 850hPa temperature and wind between historical (MME_HIST) and future (MME_RCP8.5) simulations, based on RegCM4 downscaling results. The original historical and future-projected values are shown in **Appendix 2.1**. It can be seen that the whole domain is undergoing warming under the RCP8.5 climate scenario. The temperature increase is generally stronger over land and in higher latitudes, especially for SON and DJF. The whole domain is warmed by about 2 to 3°C in the low levels in MAM and JJA. Warming of more than 4°C is found over locations north of 25°N in SON and DJF, with the strongest signal near the Chongqing province (30°N, 105°E).

For the low-level wind, changes due to global warming are negligible in MAM and DJF. For JJA, there is enhanced westerly over the 5 – 15°N. There is a strengthened low-level cyclonic flow near the eastern boundary in SON. A similar feature was found by Liu et al. (2011) based on RCM simulations. This induces a stronger northerly wind component over Southern China, the consequence of which on the regional precipitation will be further examined.

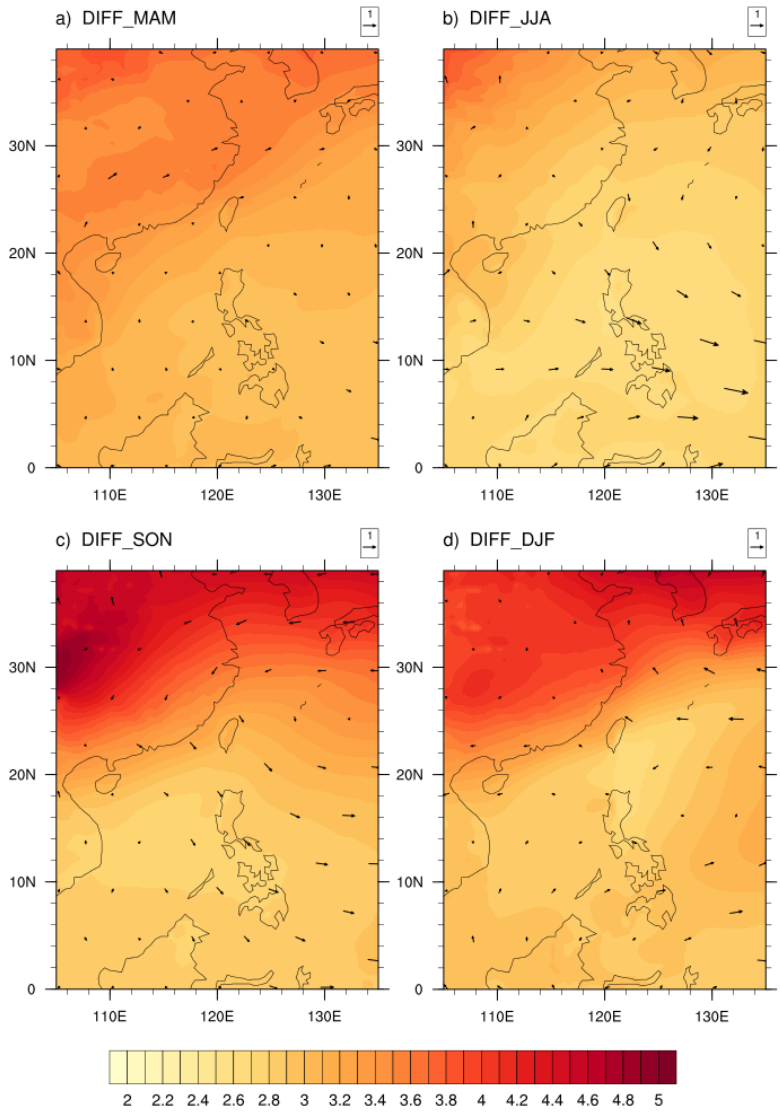


***Figure 4.1*** *MME_RCP8.5 minus MME_HIST mean 850hPa temperature (shading, units: K) and wind (arrows, units: ms$^{-1}$) in (a) MAM, (b) JJA, (c) SON, and (d) DJF. RegCM4_GF(RegCM4_AC) is excluded for JJA(SON).*

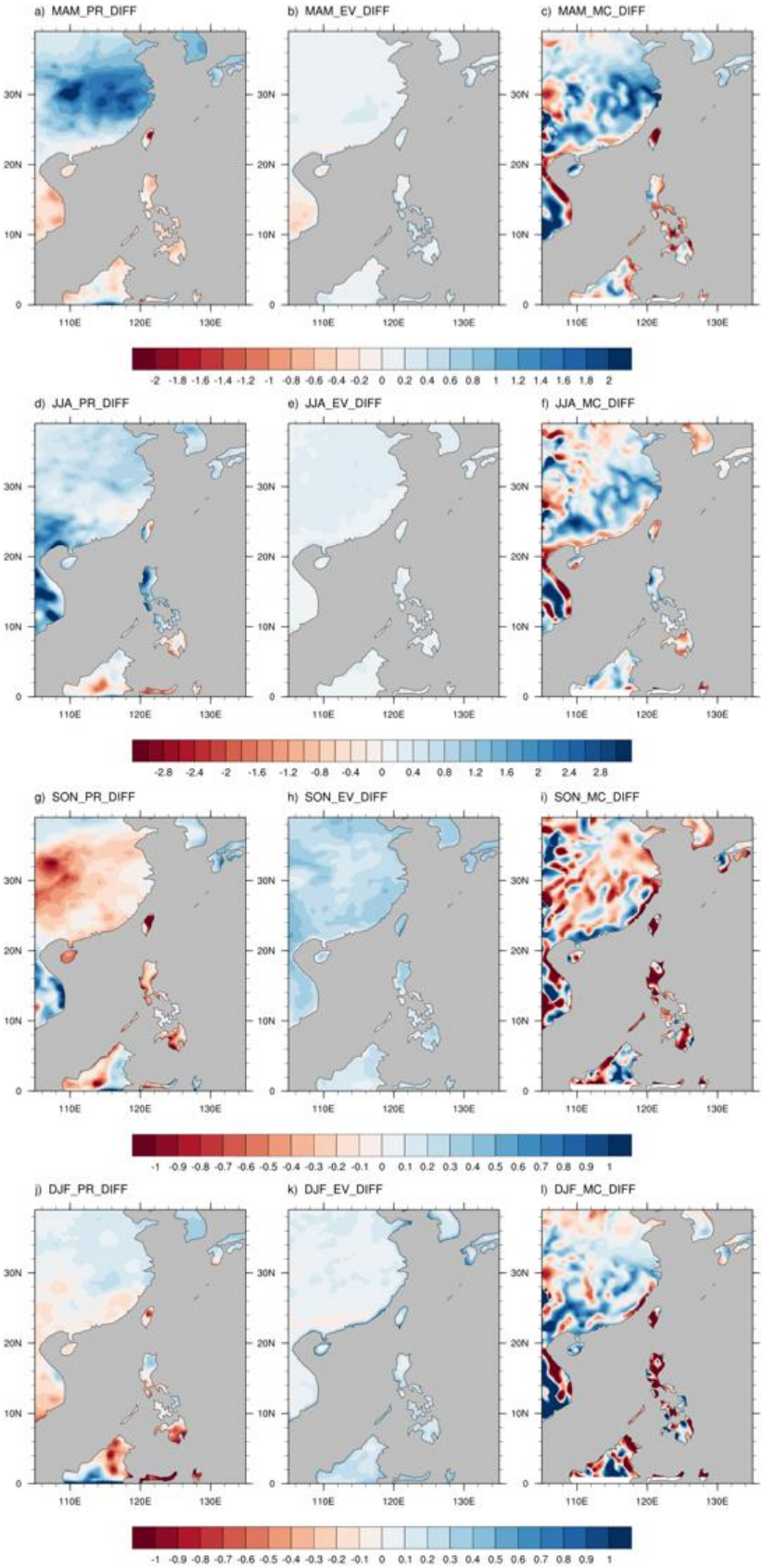


***Figure 4.2*** *Difference of seasonal mean (a, d, g, j) precipitation, (b, e, h, k) evaporation, and (c, f, i, l) vertically integrated moisture flux convergence between MME_HIST and*

*MME_RCP8.5 for (a, b, c) MAM, (d, e, f) JJA, (g, h, i) SON, and (j, k, l) DJF. Only the continental region is plotted. RegCM4_GF(RegCM4_AC) is excluded for JJA(SON). The maps of the variables simulated in two MMEs are included in* ***Appendix 2.2****.*

Changes in mean precipitation for different seasons are shown in ***Figures 4.2a, d, g, j***. During MAM (***Figure 4.2a***), precipitation is increased by about 1 – 2 mm/day (20%) over the inland area of 25 – 35°N, 105 – 120°E. Rainfall changes over coastal Southern China, however, are not significant. For JJA (***Figure 4.2d***), precipitation increases generally over the whole land area. The increase in precipitation is about 0.5 – 1.5 mm/day (10 – 15%) over Southern China along the rain belt at 22 – 26°N (see ***Figure A3***). Precipitation in SON (***Figure 4.2g***), however, shows an opposite trend to that in MAM and JJA. In particular, there is a prominent dry signal south of 35°N, covering Southern China. Rainfall reduces by 15 – 20% for most of the area. For DJF, there is no significant difference in mean precipitation intensity and pattern for MME_HIST and MME_RCP8.5 (***Figure 4.2j***).

**4.2 Moisture budget analysis on seasonal mean state precipitation change**

Seasonal mean precipitation $\bar{P}$ is balanced by the evaporation $\bar{E}$ and vertically integrated moisture flux convergence $-\overline{\nabla \cdot \vec{Q}}$. In this section, moisture budget analysis is conducted in order to better understand the source precipitation change. ***Figure 4.2*** shows changes in the three terms in the moisture budget equation (equation 2.1) for MME_HIST, MME_RCP8.5. Here evapotranspiration is used to replace pure evaporation, which has similar physical meaning in the hydrological cycle.

Accompanying changes in $\bar{P}$ (see section 4.1), $\bar{E}$ is increased by no more than 0.3 mm/day over most of the domain in all seasons except SON. $\bar{E}$ contributes much more to the moisture budget in SON and has the greatest changes of about 2 times of

that in the remaining seasons. In general, $-\overline{\nabla \cdot \vec{Q}}$ matches the pattern of precipitation change for MAM and SON, but not for JJA and DJF. A possible reason for the mismatch is the decrease in the near-surface vertical resolution of the RegCM4 outputs during the interpolation from sigma-coordinates to pressure-coordinates. It could increase the calculation error of discrete vertical integration over a complex terrain when the integrated quantity has a strong vertical variation in low levels, which is the case for wind/moisture flux convergence during JJA and DJF. Nonetheless, $-\overline{\nabla \cdot \vec{Q}}$ is still useful in explaining the source of changes in precipitation in different seasons.

For wet seasons (MAM and JJA) (***Figures 4.2a – f***), the increase in $\bar{E}$ is much smaller than the increase in $\bar{P}$, which is mainly balanced by the $-\overline{\nabla \cdot \vec{Q}}$ term. This means changes in wind convergence and/or specific humidity of atmosphere are responsible for the future increase in mean rainfall during the wet seasons over Southern China. For DJF (***Figures 4.2j – l***), changes in $\bar{P}$ and $\bar{E}$ are not significant; the change in $-\overline{\nabla \cdot \vec{Q}}$ is also noisy. SON (***Figures 4.2g – i***) is the only season with suppressed $\bar{P}$. The change in $\bar{E}$ is still positive, meaning that $-\overline{\nabla \cdot \vec{Q}}$ is the reason for the suppressed $\bar{P}$ in SON. Change of this term is generally negative over the whole domain, with a magnitude comparable to the sum of $\bar{P}$ and $\bar{E}$, which satisfies equation 2.1.

## 4.4 Changes in dry season

### 4.4.1 Maximum consecutive dry days

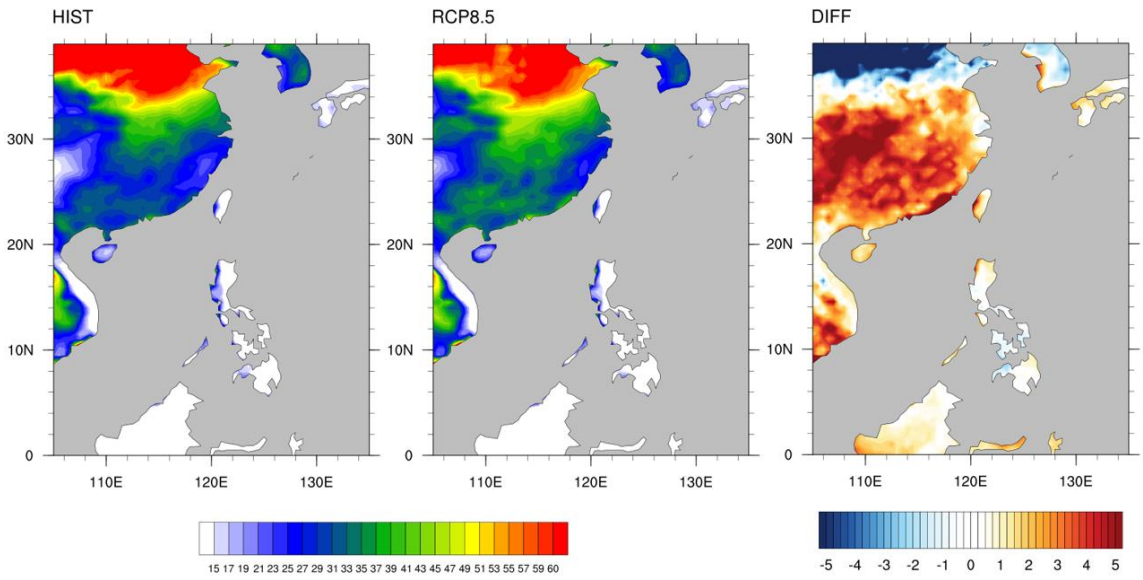


***Figure 4.8*** *Mean annual maximum consecutive dry days (units: days) for (left) MME_HIST, (middle) MME_RCP8.5, and (right) their difference.*

Previously it has been shown that SON is becoming drier in the projected future under RCP8.5. In addition to the mean precipitation, the mean CDD, computed annually, in MME_HIST and MME_RCP8.5 are also examined (***Figure 4.8***). MME_HIST gives a slightly longer CDD (by about 10%) than that in RegCM4_EA (see ***Figure 3.5***). The spatial patterns of CDD are similar in MME_HIST and MME_RCP8.5. It was found that CDD over regions south of 32°N is significantly lengthened by about 3 to 5 days, including Southern China. To further examine how CDD is changing, the mean start date and the mean end date of the consecutive dry periods are plotted in ***Figures 4.9*** and ***4.10***. Both the start date and the end date will become earlier in MME_RCP8.5. The start (end) date changes from mid-November (late December) to early November (mid-December) by about 10 days (5 days) over Southern China; such changes yield a net increase in CDD. An earlier shift in the dry season is consistent with the result that the boreal autumn will become drier in the future. For the more inland area over 28 – 34°N, changes in the start date and the end date are more dominant, although this

is not the focused region in our project. Robust signals of longer CDD are also captured in the raw GCMs (presented in **Appendix 3**). The raw GCM results increase the confidence in the lengthening CDD as well as the drier SON season. However, GCM outputs disagree with the earlier-shift of the start and the end date of CDD simulated by RegCM4. The former suggests that dry season is postponed in the future with a longer delay in the end date, which is not the case in the downscaled products.

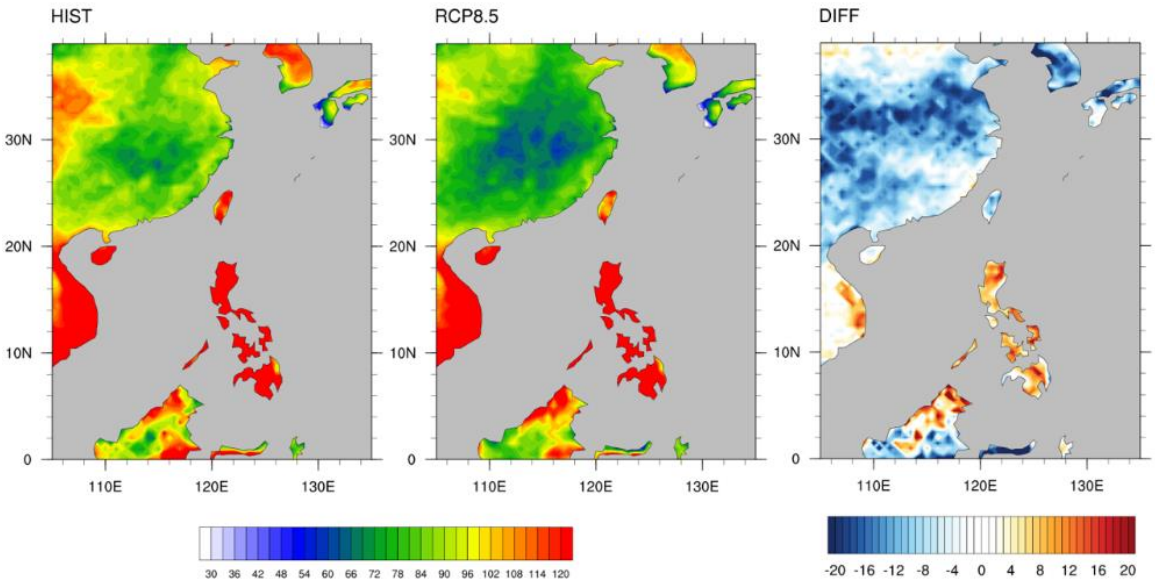


***Figure 4.9*** *Mean start date of the annual maximum consecutive dry days (units: days after 1st September) for (left) MME_HIST, (middle) MME_RCP8.5, and (right) their difference.*

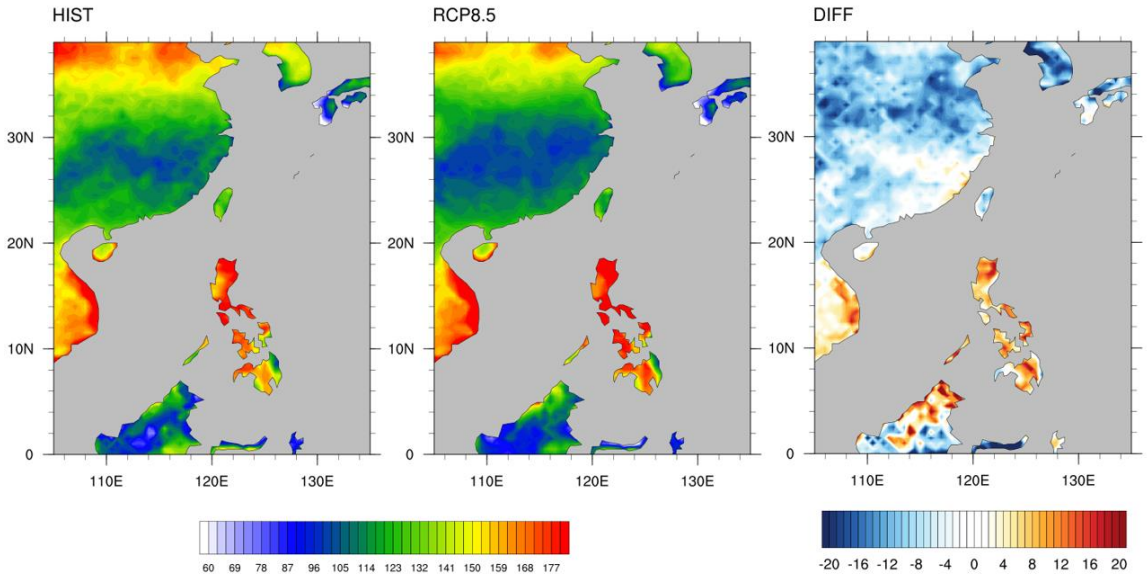


***Figure 4.10*** *Same as* ***Figure 4.9*** *but for the end date.*

4.4.2 Circulation changes associated with drier SON

Previous results such as the robust lengthening of CDD, indicate that SON is likely to become drier in the future over Southern China. In this sub-section, large-scale circulation changes associated with the drying trend will be further examined.

***Figure 4.11*** shows the difference in vertically averaged relative and specific humidity between MME_HIST and MME_RCP8.5 in the four seasons. The SON relative humidity has a significant drop by about 5 to 10%; this is not seen in other seasons. Also, a similar pattern is also found in the change of CDD, south of 32°N (see ***Figure 4.8***). Decreased relative humidity can suppress cloud formation and rainfall, thus leading to a drier SON. Moisture budget analysis indicates that there is reduced moisture flux convergence, consistent with suppressed precipitation in SON (see ***Figure 4.5***). In view of the fact that specific humidity is generally enhanced under global warming, changes in the background circulation seem to be the main reason Southern China becomes drier in SON in the future climate.

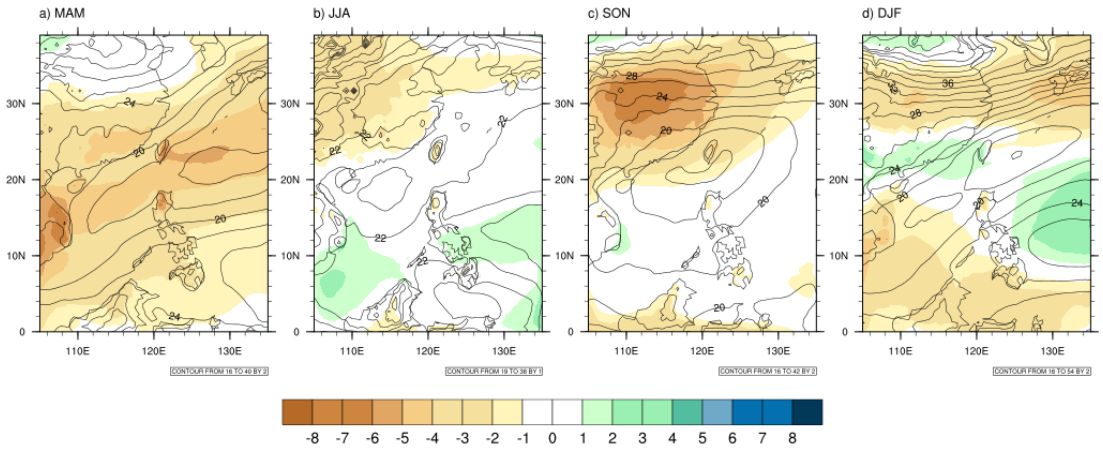


***Figure 4.11*** *Percentage changes in vertically averaged relative (shading, units: %) and specific (contours, units: %) humidity between MME_HIST and MME_RCP8.5 in (a) MAM, (b) JJA, (c) SON and (d) DJF. All four downscaled models are included in the MME.*

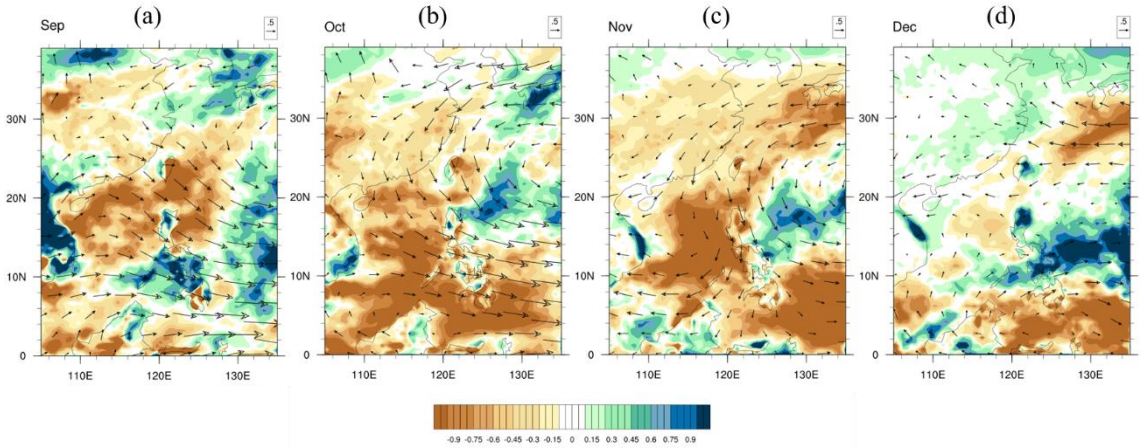


***Figure 4.12*** *Monthly mean precipitation (shading, units: mm/day) and 850hPa wind (arrows, units: ms$^{-1}$) difference between MME_HIST and MME_RCP8.5 for the period from (a) September to (d) December.*

Here we further focus on the month-to-month anomalous circulation, from September to December in the South China/Western North Pacific region. For the monthly mean 850hPa wind, a strengthened northerly component covering the whole Southern China is identified in October and November (see ***Figure 4.12***), associated with suppressed

precipitation. Further analyses using raw GCMs data are carried out to understand changes over a broader region. Eddy sea-level pressure (deviation from the area mean) (SLP*) and 850hPa wind from the MME average of the GCMs are plotted in ***Figure 4.14***. In October and November, anomalous northerly is related to negative SLP* to the east, at about 10 – 35°N. Thus the land-sea longitudinal pressure gradient becomes more negative across coastal eastern China, resulting in stronger low-level northerly wind over Southern China and intrusion of dry air from the north. Consequently, the moisture flux convergence is reduced, causing a reduction in SON precipitation and a lengthened dry season. A proposed reason for the anomalous low SLP* will be discussed in chapter 7 section 1.2.

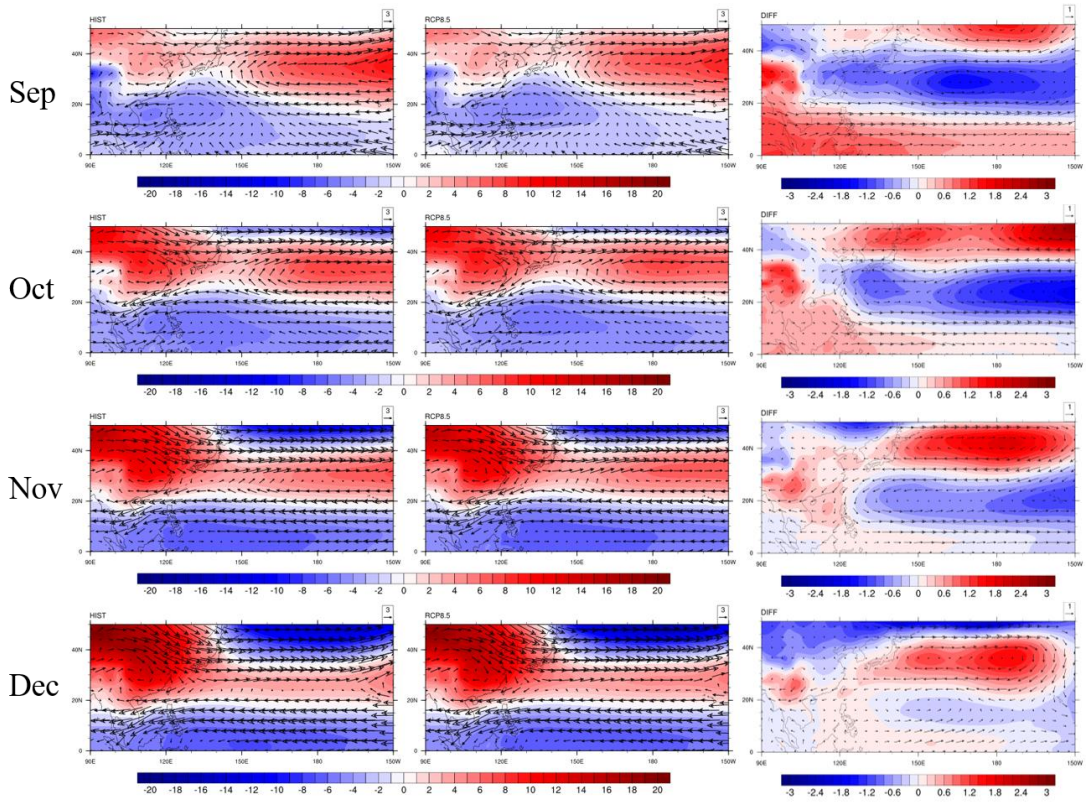


***Figure 4.13*** *Monthly plots of sea-level pressure deviated from area mean (shading, units: hPa) and 850hPa wind (arrows, units: ms$^{-1}$) from the MME of four selected raw GCMs for (left column) historical and (middle column) future simulations and (right column) their difference in (top row) September, (second row) October, (third row) November and (bottom row) December.*

# 5 Interannual Variability of Seasonal Precipitation

There are a number of circulation systems or recurrent climate modes, such as ENSO, monsoon, and WPSH, affecting the seasonal interannual precipitation variability over Southern China. Each of them might be modulated differently by the warming climate (see section 1.3). In this chapter, interannual precipitation variability over Southern China is examined; a novel moisture budget analysis method for studying precipitation variability will be introduced, in order to unveil the role of wind circulation and humidity change on such variability.

Interannual precipitation variability is represented by computing the variance of the seasonal mean rainfall. ***Figure 5.1*** shows the precipitation variance of MME_HIST, as well as the difference between MME_RCP8.5 and MME_HIST. Large variance is found only during the wet seasons (MAM and JJA) over Southern China, with values from about 5 to 10 $(mm/day)^2$. The difference between MME_HIST and MME_RCP8.5 is also large for the same seasons, and the increase is much stronger in JJA (about 30%) than that in MAM (about 15%). It is roughly equivalent to a 15% and a 7% increase in the magnitude of interannual seasonal variation, respectively. Most locations with increased interannual variance collocates with the projected wetter region (see ***Figure 4.2***). Changes in SON and DJF are rather small and noisy.

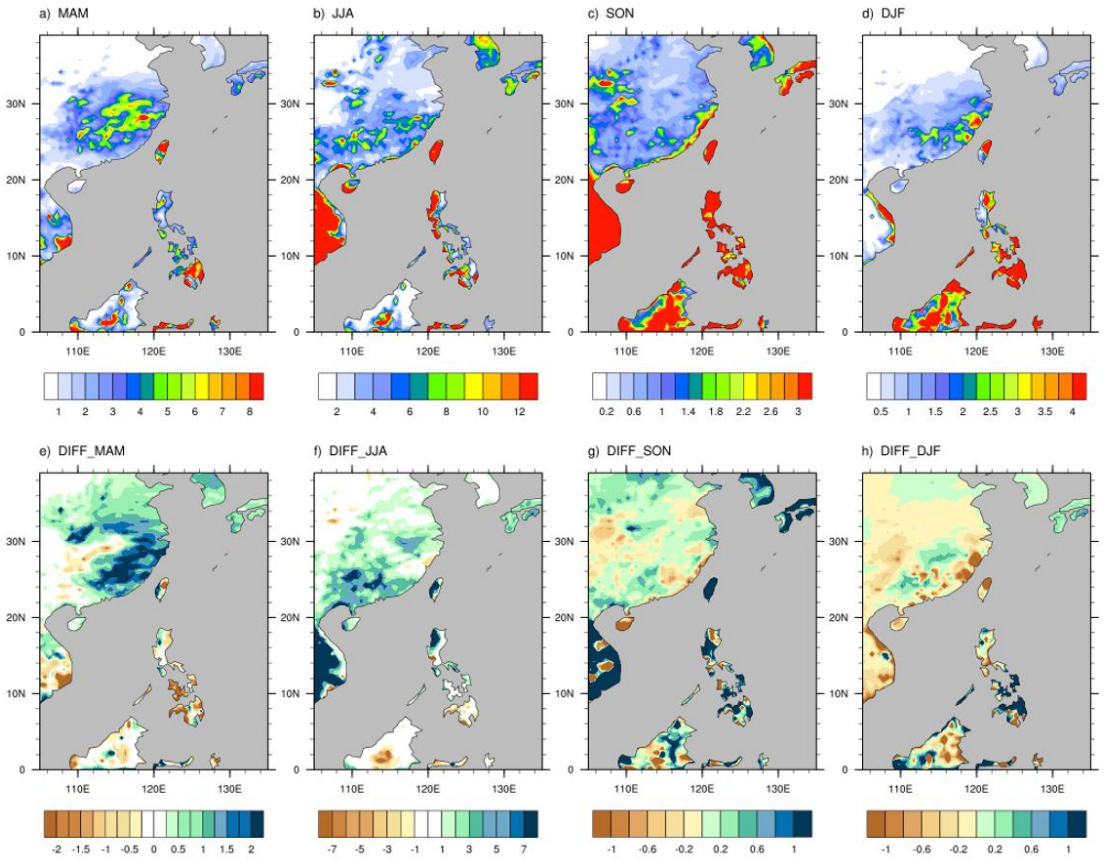


***Figure 5.1*** *MME_HIST interannual seasonal precipitation variance (upper, units: (mm/day)$^2$) and the difference from MME_RCP8.5 in (a, e) MAM, (b, f) JJA, (c, g) SON, and (d, h) DJF. RegCM4_GF(RegCM4_AC) is excluded for JJA(SON).*

The moisture budget equation can be further modified to study changes in interannual precipitation variability. Starting from:

$$P = E - \frac{1}{g}\nabla \cdot \int_0^{p_s} q\boldsymbol{V}dp \quad (5.1)$$

Removing the climatological mean and multiplying the sign of precipitation deviation $\hat{P}'$ yields:

$$\hat{P}'P' = |P'| = \hat{P}'E' - \hat{P}'\left(\frac{1}{g}\nabla \cdot \int_0^{p_s} q\boldsymbol{V}dp\right)',$$

where prime indicates the deviations from the climatological mean, with $\hat{P}' = sgn(P')$.

Taking the time average, one obtains:

$$\overline{|P'|} = \overline{\hat{P}'E'} - \overline{\hat{P}'\left(\frac{1}{g}\nabla \cdot \int_0^{p_s} q\boldsymbol{V}dp\right)'} \quad (5.2).$$

$\overline{|P'|}$ is the standard deviation of precipitation, $\overline{\hat{P}'E'}$ and $-\overline{\hat{P}'\left(\frac{1}{g}\nabla \cdot \int_0^{p_s} q\boldsymbol{V}dp\right)'}$ are contributions from evaporation and moisture flux convergence to the interannual precipitation variability, respectively. Equation 5.2 can shed light on interannual precipitation variance and its relationship with circulation changes. The results are shown in ***Figures 5.2*** and ***5.3***.

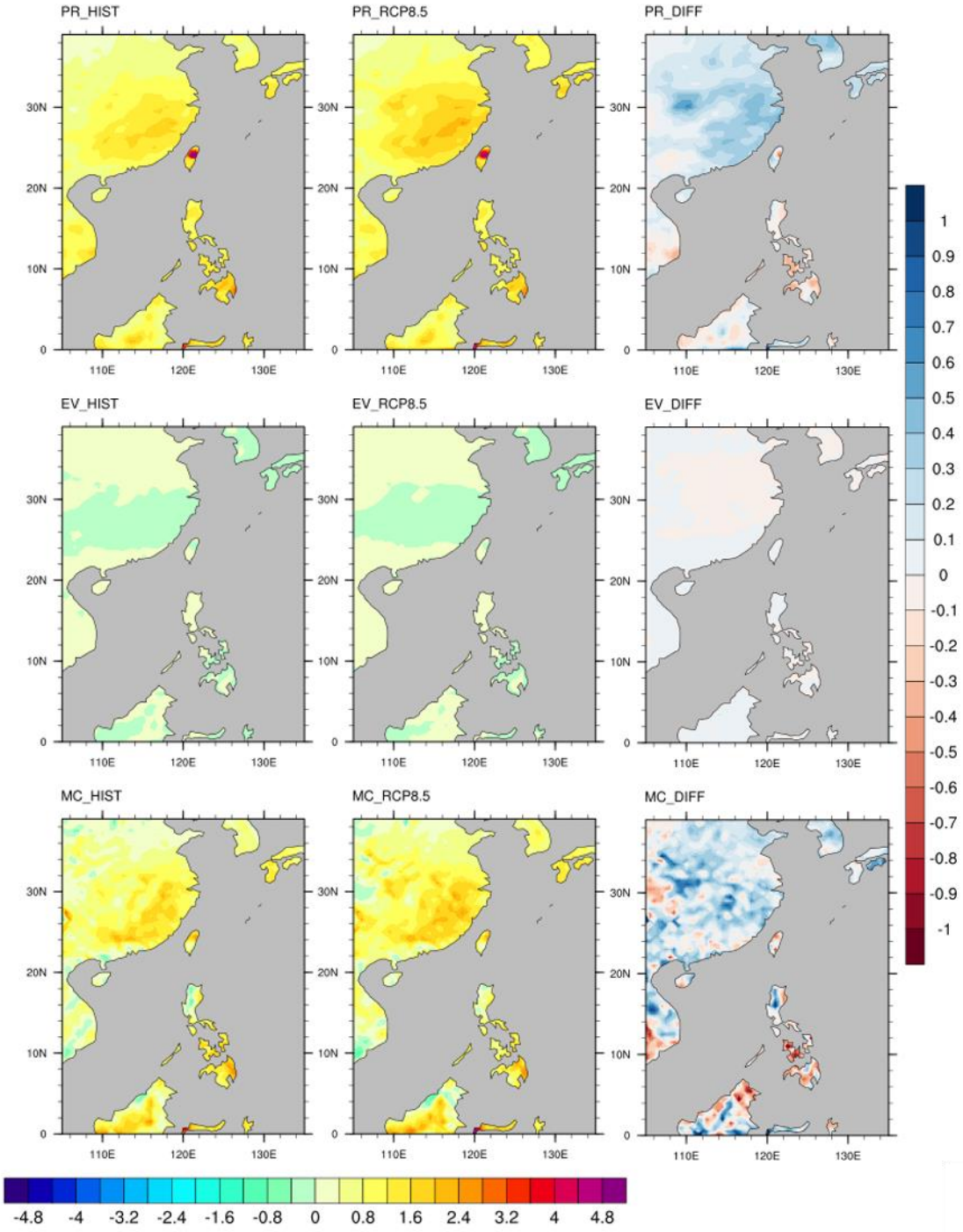


***Figure 5.2*** *Modified moisture budget for interannual variability in MAM, with all units converted into mm/day. The rows are the three terms with (top row)* $\overline{|P'|}$*, (middle row)* $\overline{\hat{P}'E'}$*, and (bottom row)* $-\overline{\hat{P}'\left(\frac{1}{g}\nabla\cdot\int_0^{p_s} q\mathbf{V}dp\right)'}$ *respectively. The columns stand for results from (left column) MME_HIST, (middle column) MME_RCP8.5, and (right column) their differences. Please refer to the text for details.*

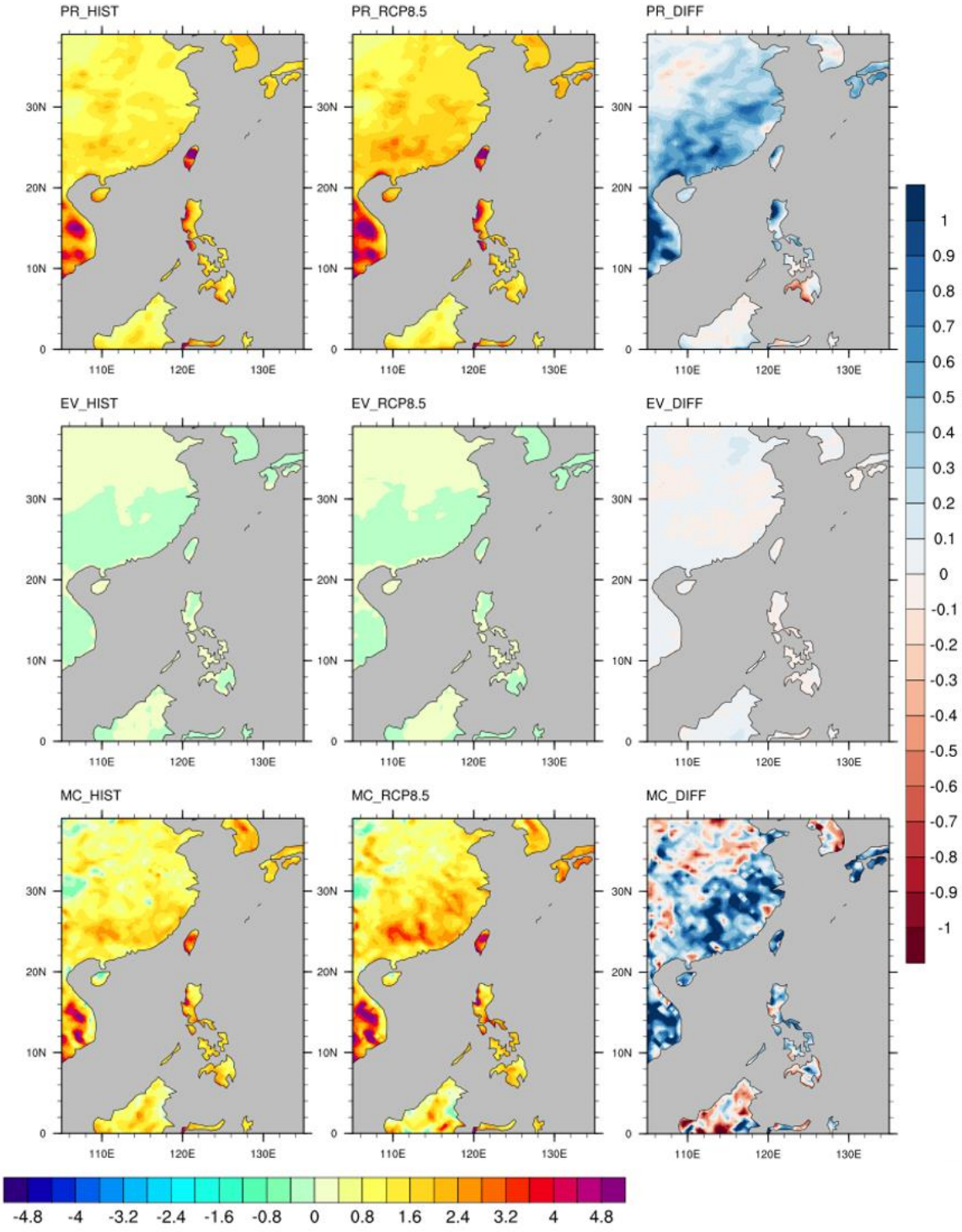


***Figure 5.3*** *Same as* ***Figure 5.2*** *but for JJA. RegCM4_GF is excluded.*

In both MAM and JJA, $\overline{\hat{P}'E'}$ is one order of magnitude smaller than $\overline{|P'|}$. The differences in $\overline{\hat{P}'E'}$ between MME_HIST and MME_RCP8.5 are also negligible,

indicating that change in $\overline{|P'|}$ is not due to $\overline{\hat{P}'E'}$. On the other hand, $\overline{-\hat{P}'\left(\frac{1}{g}\nabla\cdot\int_0^{p_s} q\boldsymbol{V}dp\right)'}$ resembles $\overline{|P'|}$ in both seasons, with comparable magnitudes and patterns. Therefore, precipitation variance is closely associated with variation in the moisture flux convergence. The $\overline{-\hat{P}'\left(\frac{1}{g}\nabla\cdot\int_0^{p_s} q\boldsymbol{V}dp\right)'}$ term is further decomposed into two terms, representing the contribution from the dynamical ($\bar{q}\boldsymbol{V}'$) and thermodynamic ($q'\overline{\boldsymbol{V}}$) effects. Their exact expression can be found in **Appendix 4**. It can be seen that the dynamical term outweighs the thermodynamic term in both seasons (see ***Figures 5.4*** and ***5.5***). This term in turn is further decomposed into three terms related to changes in background humidity ($\Delta q$), anomalous moisture advection ($\Delta(\mathbf{V}'\cdot\nabla\bar{\mathrm{q}})$) and anomalous wind convergence ($\Delta(\nabla\cdot\boldsymbol{V}')$) (***Figures 5.6*** and ***5.7***). The operator $\Delta(\cdot)$ represents the change of particular variable due to the warmer climate (see **Appendix 4** for their definitions). For MAM, the $\Delta q$ term has a similar pattern and magnitude to the total dynamical term in ***Figure 5.4***, indicating that changes in the background specific humidity are the major contributors to the dynamical effect in MAM. For JJA, the $\Delta(\nabla\cdot\boldsymbol{V}')$ term dominates, suggesting that the changing anomalous circulation is becoming more favorable for wind (hence moisture flux) convergence. Enhanced anomalous wind convergence contributes to the dynamical effect in relation to increased JJA precipitation variability.

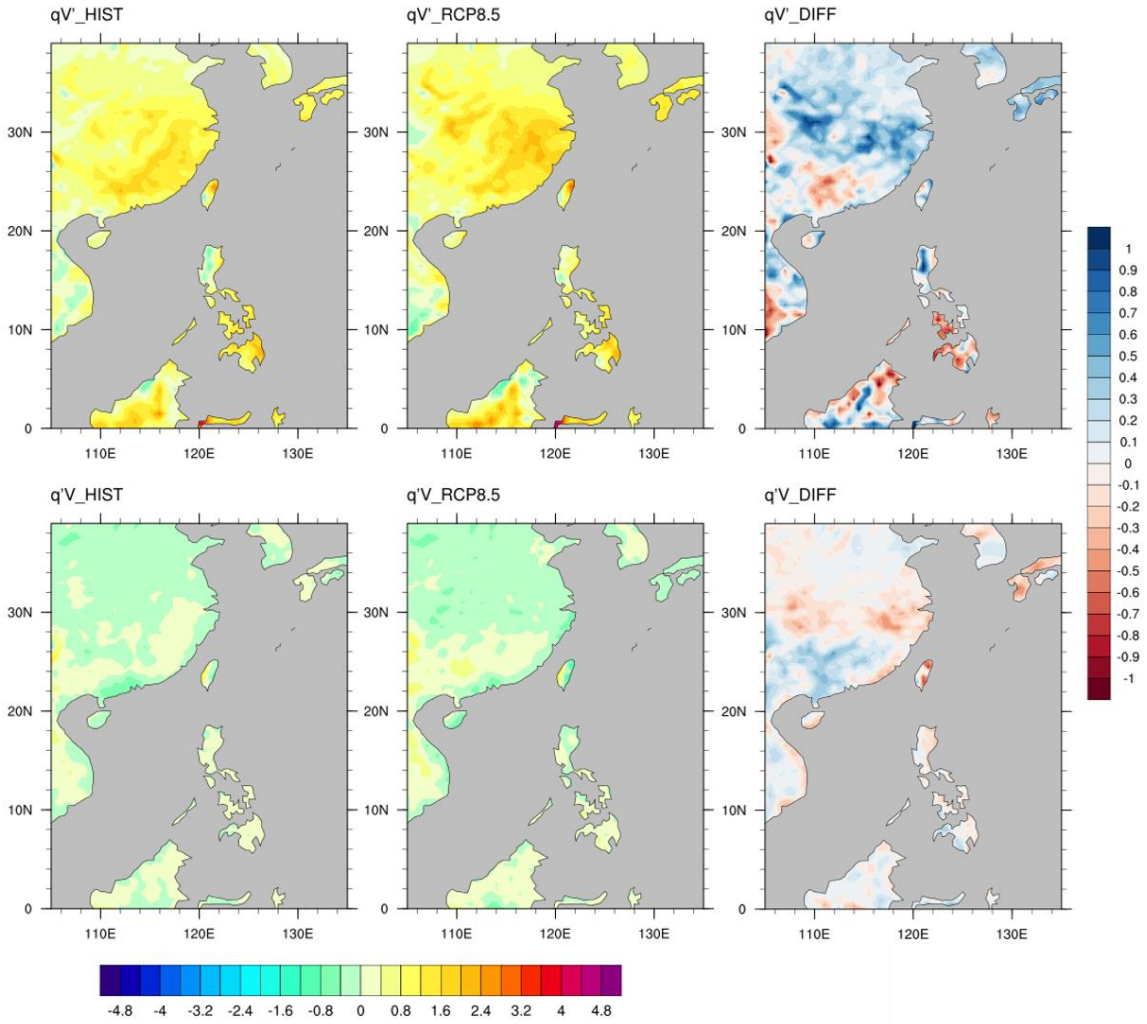


***Figure 5.4*** *Decomposed* $-\overline{\hat{P}'\left(\frac{1}{g}\nabla\cdot\int_0^{p_s} q\boldsymbol{V}dp\right)'}$ *in moisture budget for interannual variability for MAM, with all units converted into mm/day. The top panel is the dynamical term and the bottom panel is the thermodynamic term. The columns stand for results from (left column) MME_HIST, (middle column) MME_RCP8.5, and (right column) their differences. Please refer to* ***Appendix 4*** *for details.*

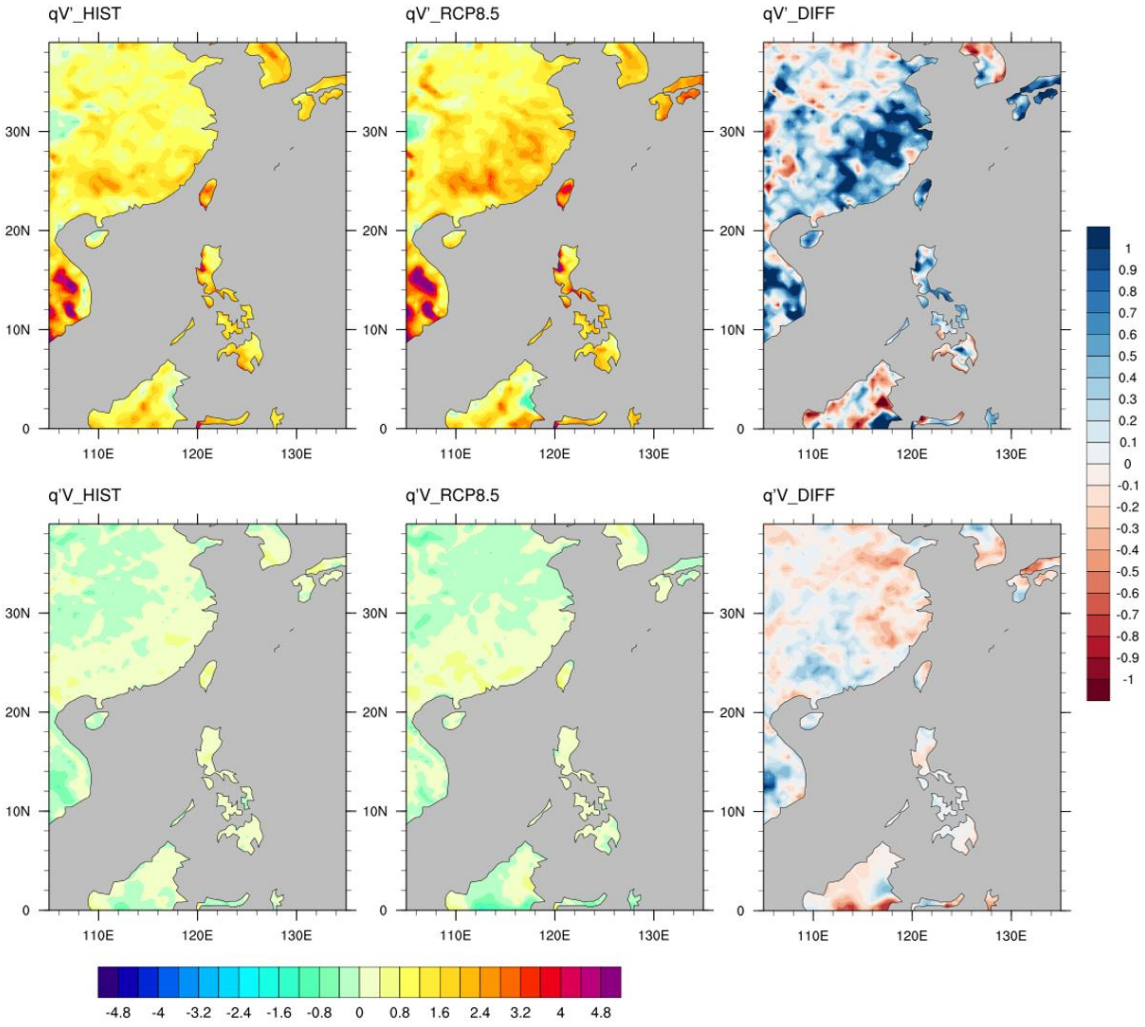


***Figure 5.5*** *Same as* ***Figure 5.4*** *but for JJA. RegCM4_GF is excluded.*

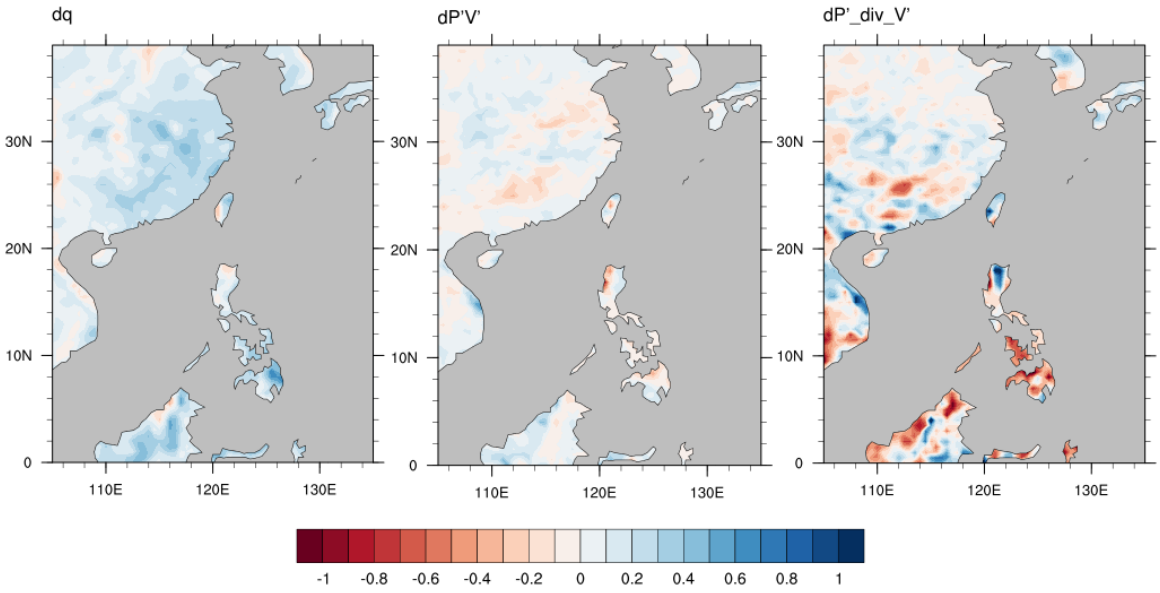


***Figure 5.6*** *Decomposed dynamical term explaining the contribution from change in (left) mean specific humidity ($\Delta q$), (middle) moisture advection ($\Delta(\boldsymbol{V'} \cdot \nabla \bar{q})$), and (right) anomalous wind convergence ($\Delta(\nabla \cdot \boldsymbol{V'})$) for MAM. Please refer to* ***Appendix 4*** *for details.*

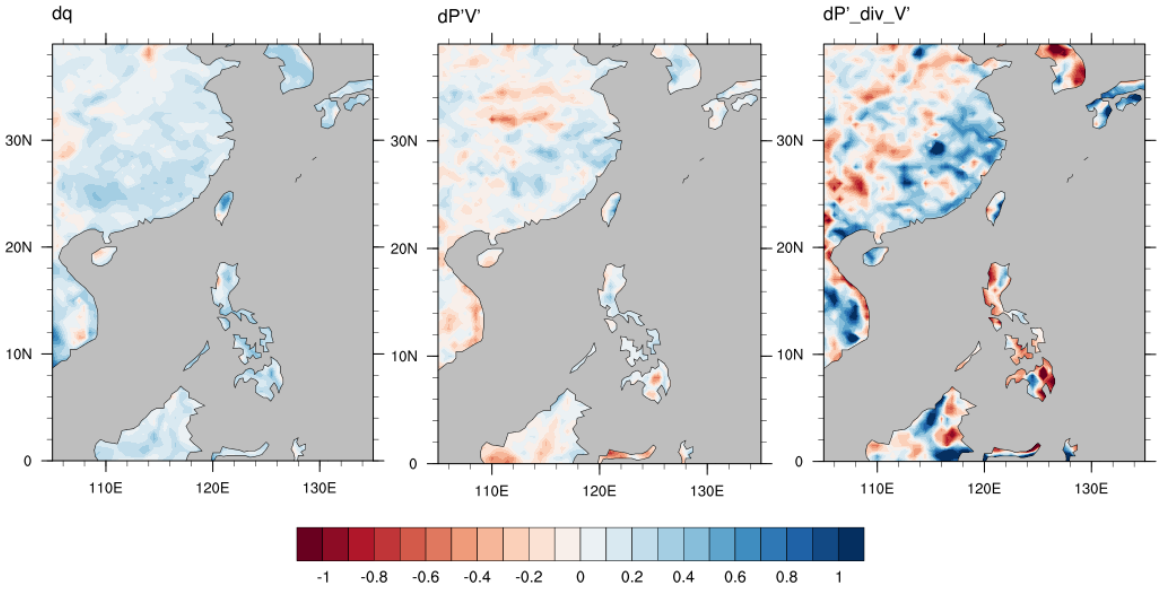


***Figure 5.7*** *Same as Figure 5.9 but for JJA. RegCM4_GF is excluded.*

# 6 Daily to Sub-daily Precipitation

Impacts of global warming on daily to sub-daily precipitation over Southern China are analyzed in this chapter. For daily precipitation, changes in probability of occurrence are studied for different seasons. Intensity change in extreme daily rainfall is also investigated and compared to that expected from the CC relation. For sub-daily precipitation, the diurnal rainfall cycle in JJA is analyzed. The frequency of 3-hourly rainfall in different seasons is included as well.

## 6.1 Daily precipitation

### 6.1.1 Daily precipitation probability density functions

A probability density function (PDF) can provide information on the frequency of events with respect to different intensities within a domain over a period of time. ***Figure 6.1*** shows the PDFs of daily precipitation calculated from MME_HIST and MME_RCP8.5 within the continental area covering Southern China based on data from $21 \times 21$ grids (22 – 32°N, 110 – 120°E). TRMM 3B32 and APHRODITE results are also included for comparison. PDFs of MME_HIST generally lie between TRMM and APHRODITE for intense rainfalls, indicating that MME_HIST can reproduce a reasonable occurrence of daily rainfall with different rain rates. The ratio of MME_RCP8.5 to MME_HIST indicates changes in the frequency of rainfall events with different intensities. If the ratio is above 1.0, it means the frequency is higher in the future for that particular intensity.

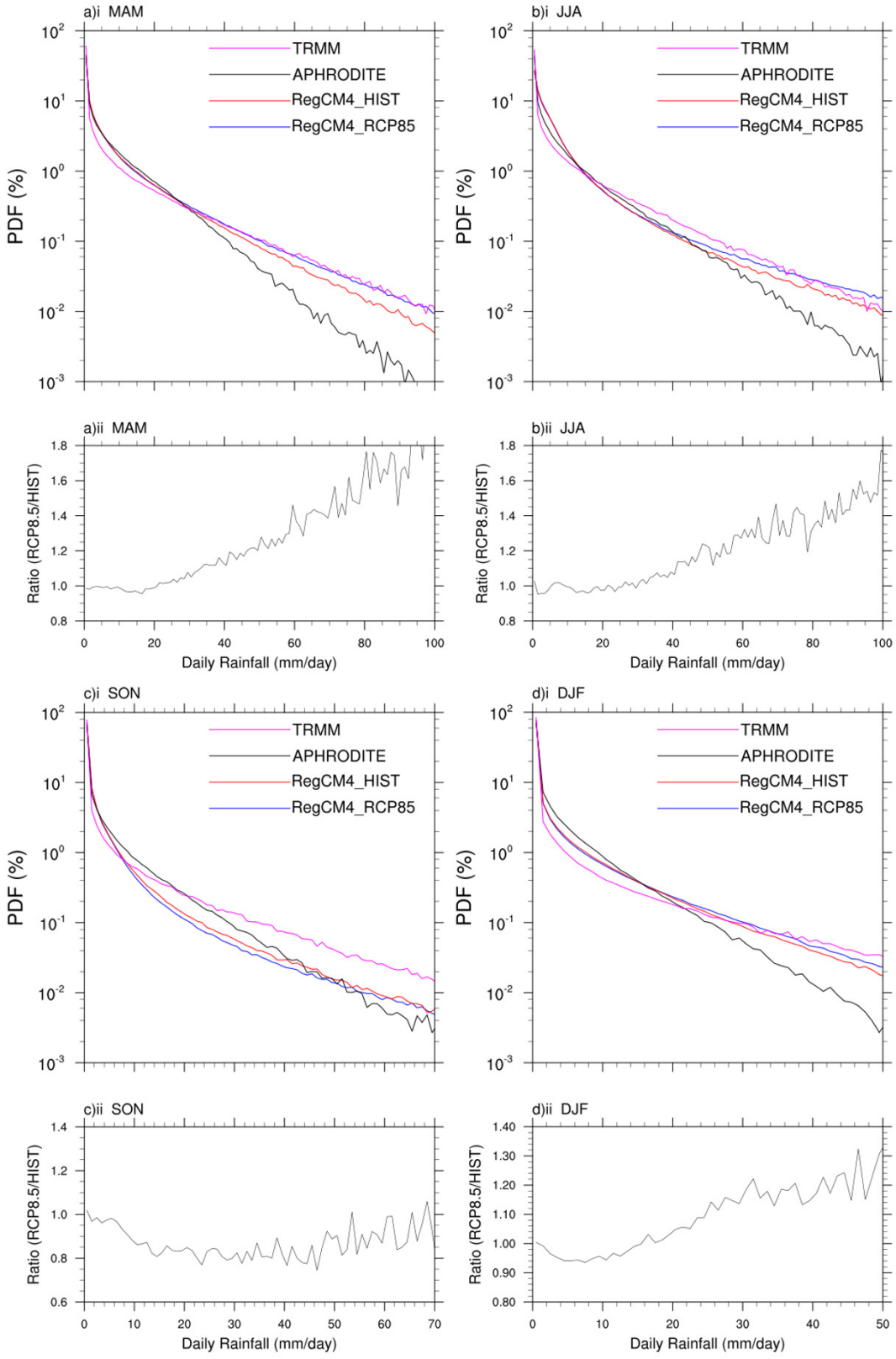


***Figure 6.1*** *(i) PDF (units: %) of (a) MAM, (b) JJA, (c) SON, and (d) DJF daily rainfall for TRMM, APHRODITE, MME_HIST, and MME_RCP8.5 with respect to different intensities over an area (22 – 32°N, 110 – 120°E). The y-axis is on a log-scale. The bottom plots (ii) are the ratio of the PDFs of MME_RCP8.5 to MME_HIST. The bin*

*width is 1mm/day. RegCM4_GF (RegCM4_AC) is excluded in JJA (SON).*

The ratios of probability of MME_RCP8.5 to MME_HIST are found to be similar for MAM, JJA, and DJF (see ***Figures 6.1a, b, d***). For light to moderate rain, historical and future climate give comparable frequencies. However, for extreme rainfall events with $\leq$ 1% occurrence, their frequencies increase sharply as a function of rain rates, especially for MAM and JJA (by about 30% to 60% for the same rain rate). PDFs in SON behaves differently compared to the other seasons, the probability of rain $\geq$ 5 mm/day is decreased by about 10 to 20% in MME_RCP8.5 compared to the same rain rate in MME_HIST (***Figure 6.1c***). It is noteworthy that SON is also the season with a significant reduction in seasonal mean rainfall.

6.1.2 Daily precipitation extreme

Daily precipitation extreme is indicated using the 95$^{th}$ percentile of daily rainfall for "rain days" (days with precipitation more than 1.0 mm/day) (referred to as 95PC). To maintain a reasonable presentation of the statistics, 95PC is investigated separately for each model, and their results for all seasons are shown in ***Figures 6.2*** – ***6.5***. TRMM gives a 95PC much larger than APHRODITE; it was reported TRMM tends to overestimate the daily extreme rainfall value in Southeast China (Zhao and Yatagai 2014), with too many dry days over China (Huang et al. 2017), because of insufficient numbers of rainfall over land in the input microwave estimates (Huffman et al. 2010). From ***Figure 6.1***, TRMM gives a very high (lower) probability of daily rain rate $\leq$ 1 mm/day (with light to moderate rainfall) in all seasons. However, the mean rainfall from TRMM is larger than that from APHRODITE (see ***Figures 3.3*** and ***3.4***). Thus, it seems that TRMM tends to give a higher proportion in heavy rainfall and hence a larger 95PC. On the other hand, APHRODITE probably underestimates the extreme

daily rainfall in southeast Asia (Ono and Kazama 2011), resulting in smaller 95PC. Although most downscaled models have a 95PC magnitude lying between TRMM and APHRODITE, here we focus on the change in 95PC under the warmer climate, instead of its absolute values.

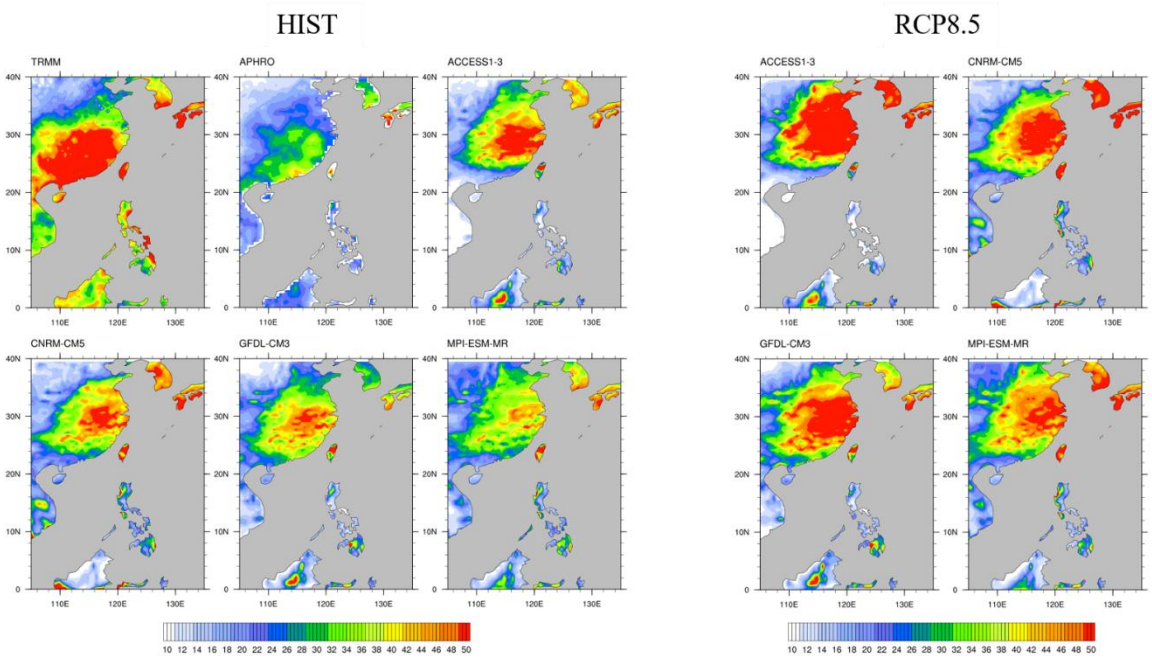


***Figure 6.2*** *The 95$^{th}$ percentile of daily precipitation (units: mm/day) in wet days during MAM for each model or reference data. The left panel shows the results from historical simulations or reference data while the right panel shows the future simulations. The name of the dataset is labeled on the top-left corner of each plot.*

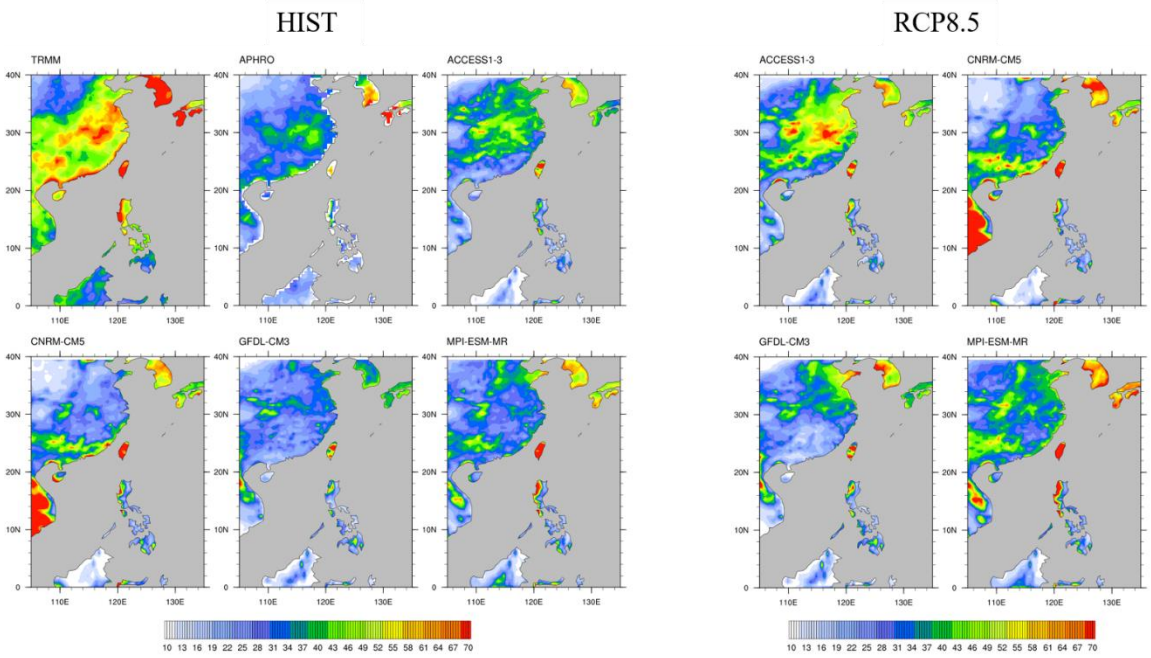


***Figure 6.3*** *Same as* ***Figure 6.2*** *but for JJA. Results from RegCM4_GF are also shown for a reference only without any further interpretation.*

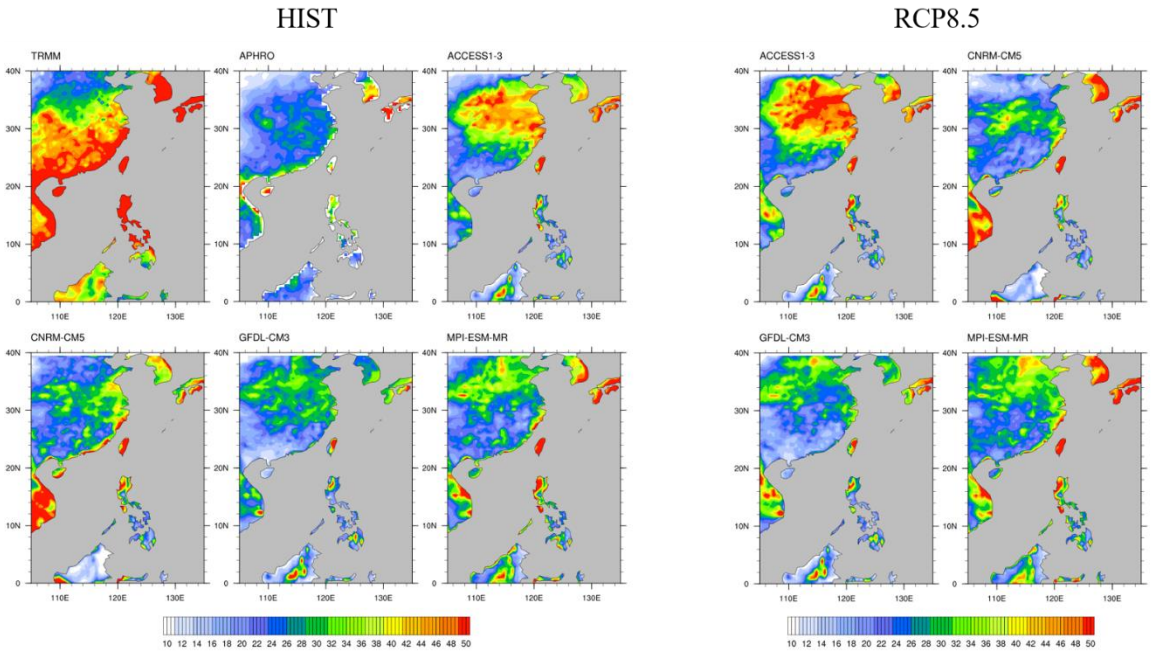


***Figure 6.4*** *Same as* ***Figure 6.2*** *but for SON. Results from RegCM4_AC are also shown for a reference only without any further interpretation.*

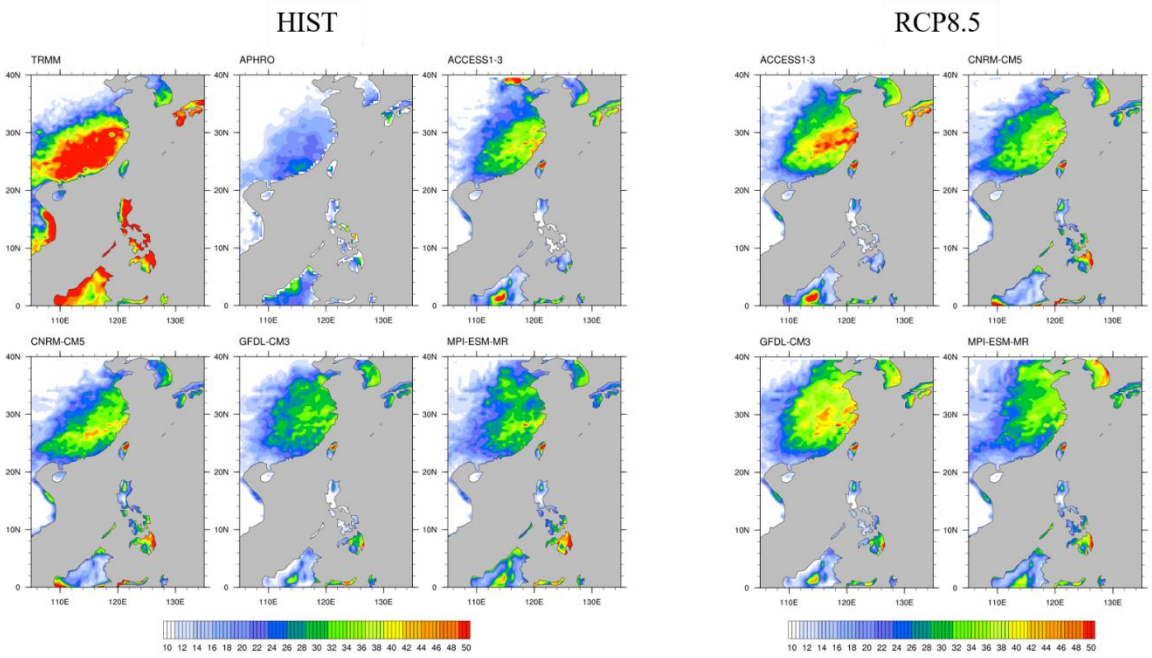


***Figure 6.5*** *Same as* ***Figure 6.2*** *but for DJF.*

For MAM (***Figure 6.2***), the patterns and magnitudes of 95PC are similar among four downscaled models under both historical and RCP8.5 scenarios, which also resemble the seasonal mean rainfall. Extreme daily rainfall signals are found to expand to the north in MME_RCP8.5, with a general increase in magnitude by about 5 to 10 mm/day. On the other hand, there is little change in 95PC over coastal Southern China. For JJA, the pattern varies among the downscaled datasets (***Figure 6.3***). Apart from RegCM4_GF, which is discarded from our analysis, all models projected an increase in 95PC over Southern China for about 5 to 10 mm/day. RegCM4_CN and RegCM4_MP agree with each other well. RegCM4_AC cannot reproduce the strong 95PC over coastal regions; instead, it gives strong signals in a more inland area. High values of 95PC north of 28°N is also seen in both reference data. For SON (***Figure 6.4***), 95PC from dynamical downscaling has patterns similar to APHRODITE (except for RegCM4_AC). RegCM4_GF gives 95PC over Southern China smaller than the RegCM4_CN and RegCM4_MP. RegCM4_GF and RegCM4_CN have a slightly

reduced SON 95PC over Southern China, while changes given by RegCM4_MP are not significant. For DJF, the 95PC pattern is slightly displaced to the northeast in the downscaling results compared to both TRMM and APHRODITE (***Figure 6.5***). The patterns and magnitudes are similar among models. Unlike the mean precipitation, 95PC in the DJF season increases for all models. The magnitude of increment depends on the location, but in general is no more than 5 mm/day.

Overall, the most robust increase in daily extreme precipitation is found in MAM and JJA. Here, we compare changes in 95PC with prediction according to the CC relation, which relates the atmospheric saturated vapor pressure $e_s$ with the change in low-level tropospheric temperature *T*:

$$\frac{de_s}{e_s} = \frac{L_v(T)}{R_v T^2} dT,$$

where $L_v$ is the latent heat of evaporation of water and $R_v$ is the gas constant for water vapor. After substituting typical values on Earth, $\frac{L_v(T)}{R_v T^2}$ is roughly equal to 0.07/°C, meaning that there is about a 7% increase in $e_s$ of the atmosphere for every 1°C increase in T. As discussed in section 1.3, past modeling studies suggested that increase in extreme precipitation intensity roughly follows the CC relation.

***Figures 6.6*** and ***6.7*** show the fractional change of 95PC in MAM and JJA, per degree change in 850hPa seasonal mean temperature $\left(\frac{\Delta 95pc}{\Delta T}\right)$. The PDF accounts for the probability of grids having certain values in $\frac{\Delta 95pc}{\Delta T}$ within the area 22 – 32°N, 110 – 120°E covering Southern China. For MAM (***Figure 6.6***), RegCM4_AC does not reproduce a significant change in 95PC over Southern China. Most grids in RegCM4_GF and RegCM4_CN have a $\frac{\Delta 95pc}{\Delta T}$ of about 5% per K, which is comparable but slightly smaller than that expected from the CC relation. RegCM4_MP

matches the theoretical CC values and has its peak value at about 7% per K. The MME mean of downscaled models has also a peak at 5% per K but with a rather wide distribution. These results suggest that extreme daily precipitation change is in broadly consistent with the CC relation over Southern China in MAM. In JJA (***Figure 6.7***), RegCM4_AC and RegCM4_CN give values of $\frac{\Delta 95pc}{\Delta T}$ along the rain-belt of about 6 to 9 % per K, while RegCM4_MP gives smaller values of about 2 to 6% per K. RegCM4_GF is the only model showing reduced 95PC and is discarded from our analysis. The PDFs of all other models have a similar shape and peak at about 5% per K. The change of daily precipitation extremes in JJA is also comparable to the CC relation with a less regional dependence than that in MAM.

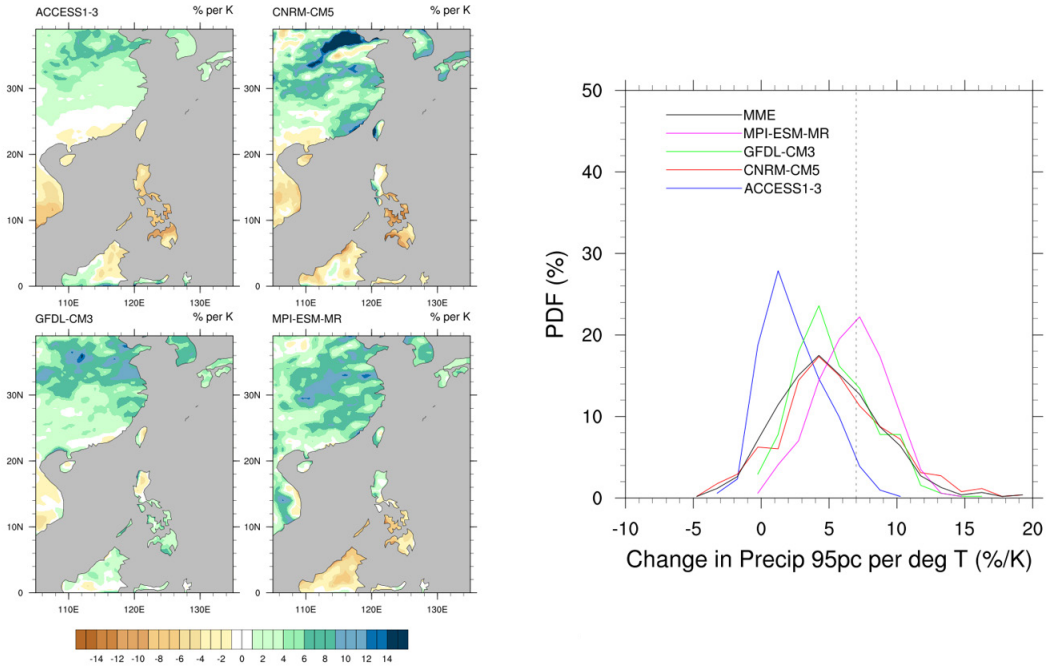


***Figure 6.6*** *(left panel) Changes in 95PC per degree rise in 850hPa temperature (units: % per K) in MAM for the downscaled models and (right) the corresponding PDFs (units: %) over the area (22 – 32°N, 110 – 120°E). The expected value from CC relation (7% per K) is represented by the dotted line. The bin width is 1.5 % per K.*

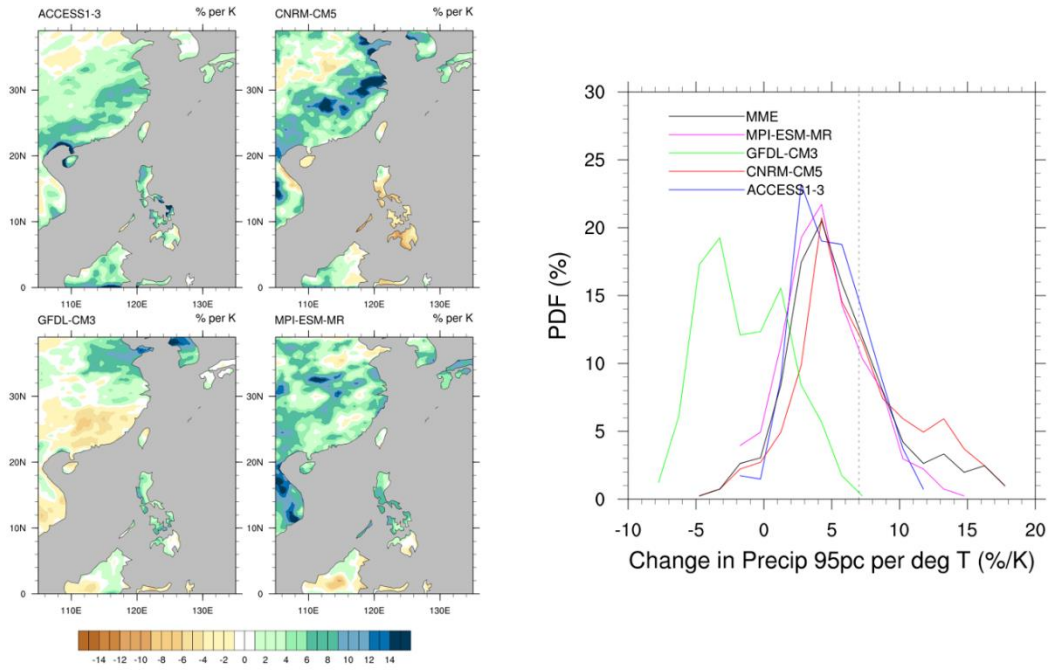


***Figure 6.7*** *Same as* ***Figure 6.6*** *but for JJA. RegCM4_GF is excluded in the MME mean PDF.*

## 6.2 Sub-daily precipitation

Sub-daily scales rainfall characteristics, including the DR cycle and frequency of 3-hourly precipitation as a function of rain rates, are analyzed in this section. TRMM is used as the reference data for assessing the performance of RegCM4; there is no sub-daily rain rate record in the APHRODITE data.

### 6.2.1 Summertime diurnal rainfall cycle

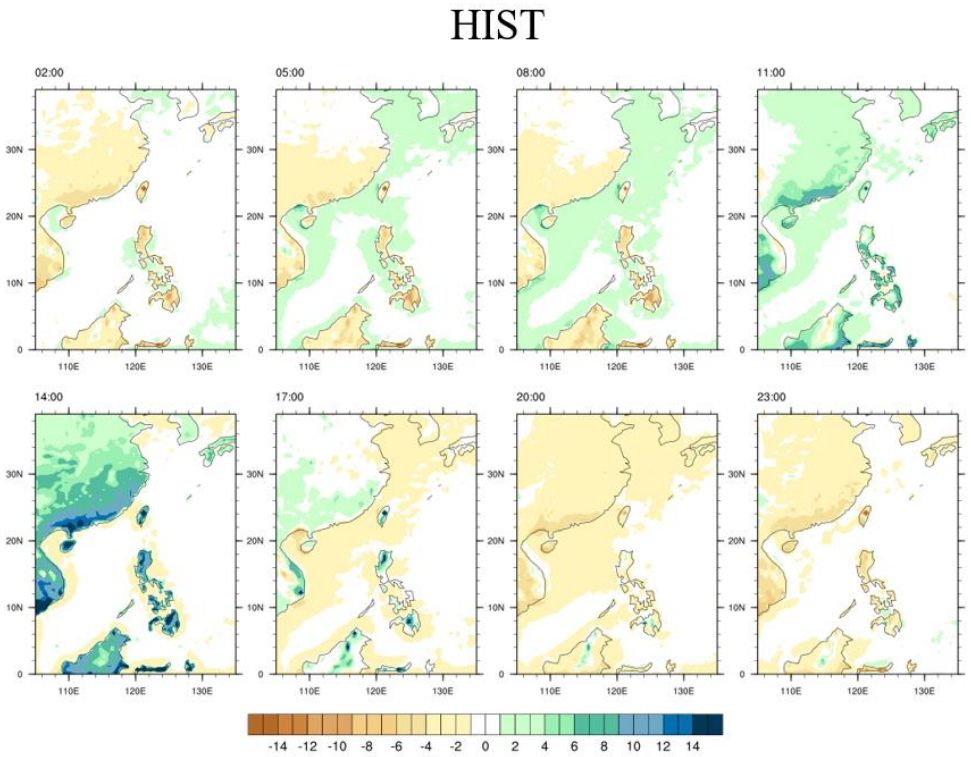


***Figure 6.8*** *3-hourly JJA precipitation deviation from the daily mean (units: mm/day) from MME_HIST. The local time (UTC +8) is labeled on the top-land corner of each plot. RegCM4_GF is excluded.*

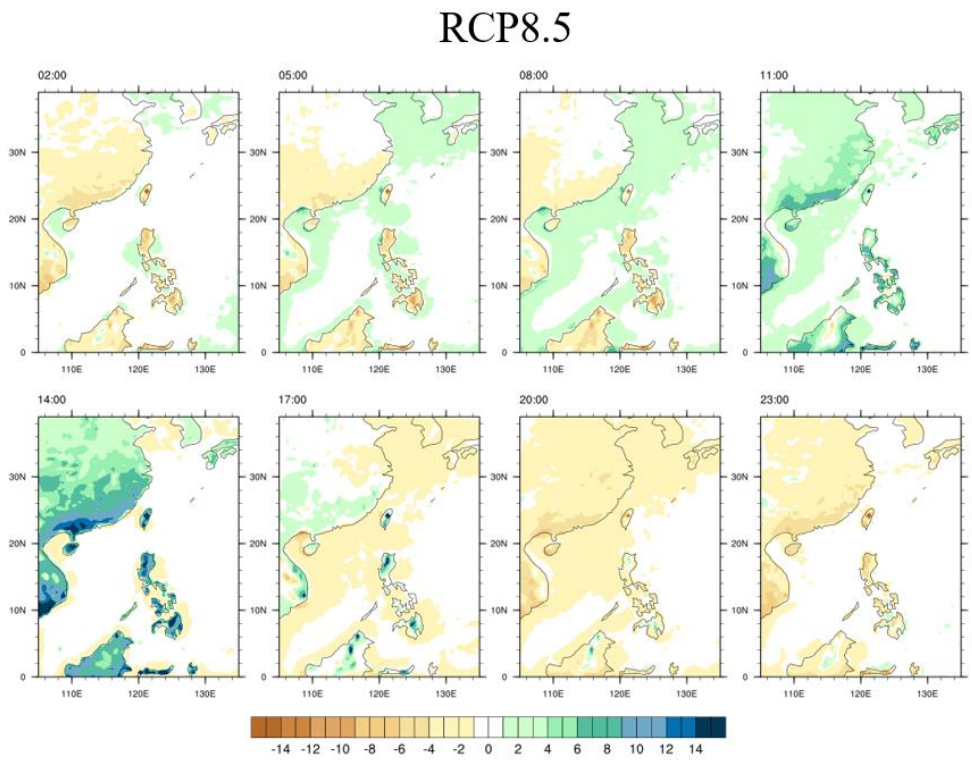


***Figure 6.9*** *Same as* ***Figure 6.8*** *but for MME_RCP8.5.*

DR cycles for MME_HIST and MME_RCP8.5 are shown in ***Figures 6.8*** and ***6.9***. Both have a similar magnitude and pattern compared to RegCM4_EA. The DR cycles are also consistent among all downscaled GCM data (not shown), indicating that RCM controls most features of DR cycles. Note that there is no significant difference between MME_HIST and MME_RCP8.5. To further investigate changes in DR magnitude and spatiotemporal distribution, empirical orthogonal function (EOF) analyses are conducted using hourly mean precipitation from MME_HIST and MME_RCP8.5 respectively. The spatial patterns are multiplied by the standard deviation of the associated principal components (PCs), while the PCs are normalized, to make the magnitude of spatial patterns have a physical meaning in representing the strength of DR. ***Figure 6.10*** shows the first-leading EOF and the corresponding PC for the afternoon rainfall mode. Both PCs in MME_HIST and MME_RCP8.5 have a peak at about 14:00 LT, in agreement with ***Figures 6.8*** and ***6.9***. There is no significant

difference between MME_HIST and MME_RCP8.5; there is no obvious change in the spatiotemporal pattern of the afternoon rainfall under climate change. For the second-leading EOF (***Figure 6.11***), it represents the morning rainfall mode. The PC time series also matches the DR cycles over the ocean. Still, there is not a noticeable difference between MME_HIST and MME_RCP8.5 for this EOF. Note that the two PCs together explain more than 90% of the diurnal variance. From the EOF analyses, we conclude that there is no significant spatiotemporal change in JJA DR cycles over Southern China due to global warming.

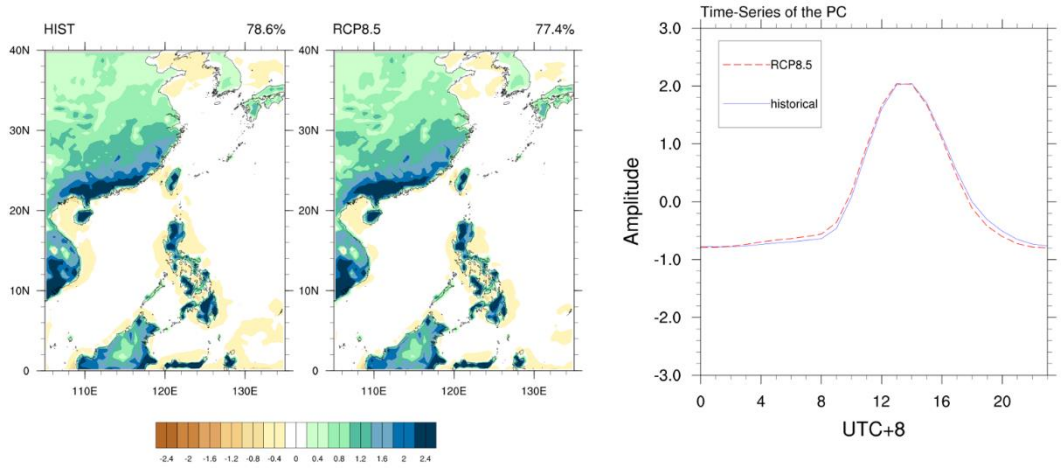


***Figure 6.10*** *The first-leading EOF of JJA climatological hourly precipitation for (left panel) the spatial patterns (units: mm/day) and (right) the associated PCs. The percentages of variance explained by the PC are labeled on the top-right hand corner of the maps. Blue (Red-dotted) curve represents the time-series for MME_HIST (MME_RCP8.5). RegCM4_GF is excluded.*

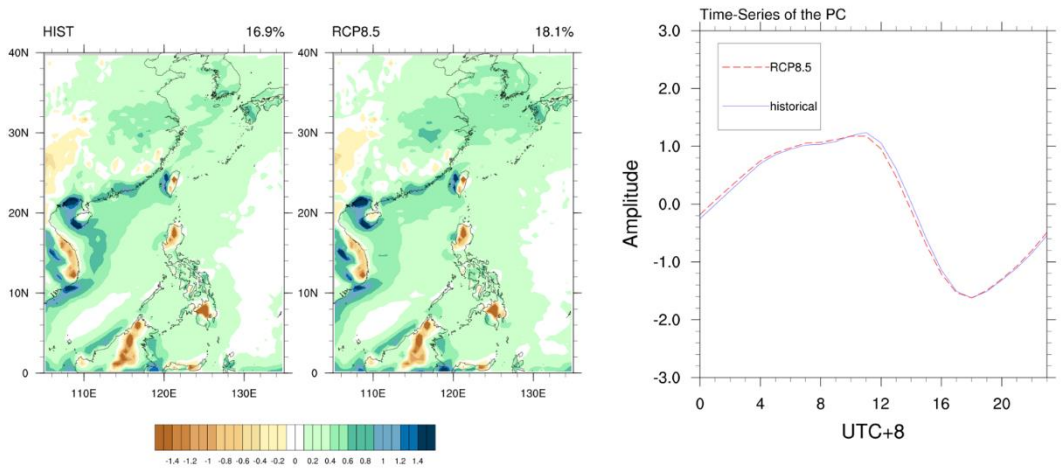


***Figure 6.11*** *Same as* ***Figure 6.10*** *but for the second-leading EOF.*

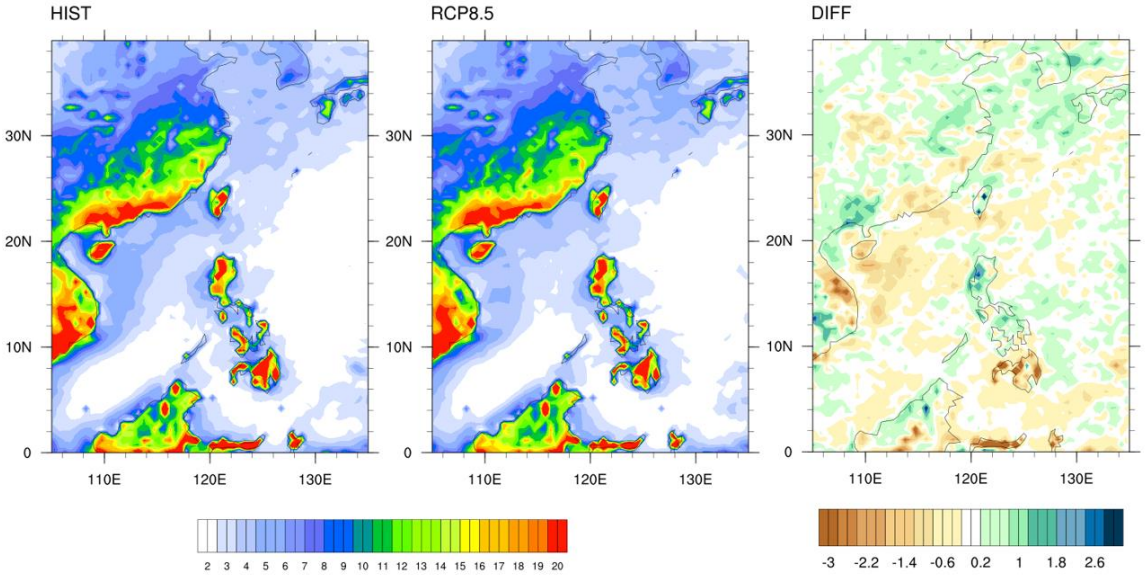


***Figure 6.12*** *The JJA diurnal range (units: mm/day) for (left) MME_HIST, (middle) MME_RCP8.5 and (right) their difference. RegCM4_GF is excluded.*

The diurnal range of DR is shown in ***Figure 6.12***. The major diurnal range pattern resembles that of the afternoon rainfall. The difference between MME_HIST and MME_RCP8.5 is small, with most locations having a difference less than 1 mm/day. The result suggests that changes in the magnitude of DR are not significant.

JJA DR cycle over Southern China is not projected to change significantly under the

warmer climate. It might be due to the fact that, in JJA, under general warming, the change in land-sea temperature contrast is small (see ***Figure 4.1***). Given the importance of land-sea temperature contrast in determining the properties of DR, this could be the reason why change in DR is not significant.

### 6.2.2 3-hourly Precipitation Probability Density Functions

A similar analysis to that in examining the frequency in daily rainfall (section 6.1.1) is carried out to investigate changes in the 3-hourly rainfall occurrence with respect to different intensities (see ***Figure 6.13***). The MME mean PDFs of 3-hourly rainfall obtained from the downscaled models match that for TRMM well, except for SON, which has less frequent 3-hourly rainfalls for intensities larger than 5 mm/day. Projected changes in the frequency of 3-hourly precipitation are similar to those for daily rainfall. MME_RCP8.5 has a comparable or less common occurrence of weak to mild rainfalls to MME_HIST in all seasons. Except for SON, intense 3-hourly rainfalls are becoming more frequent and the difference increase as a function of the rainfall intensity. Rainfall, for all intensities, becomes less frequent in SON, with the probability of intense rainfall in MME_RCP8.5 drops more than 10% compared to MME_HIST.

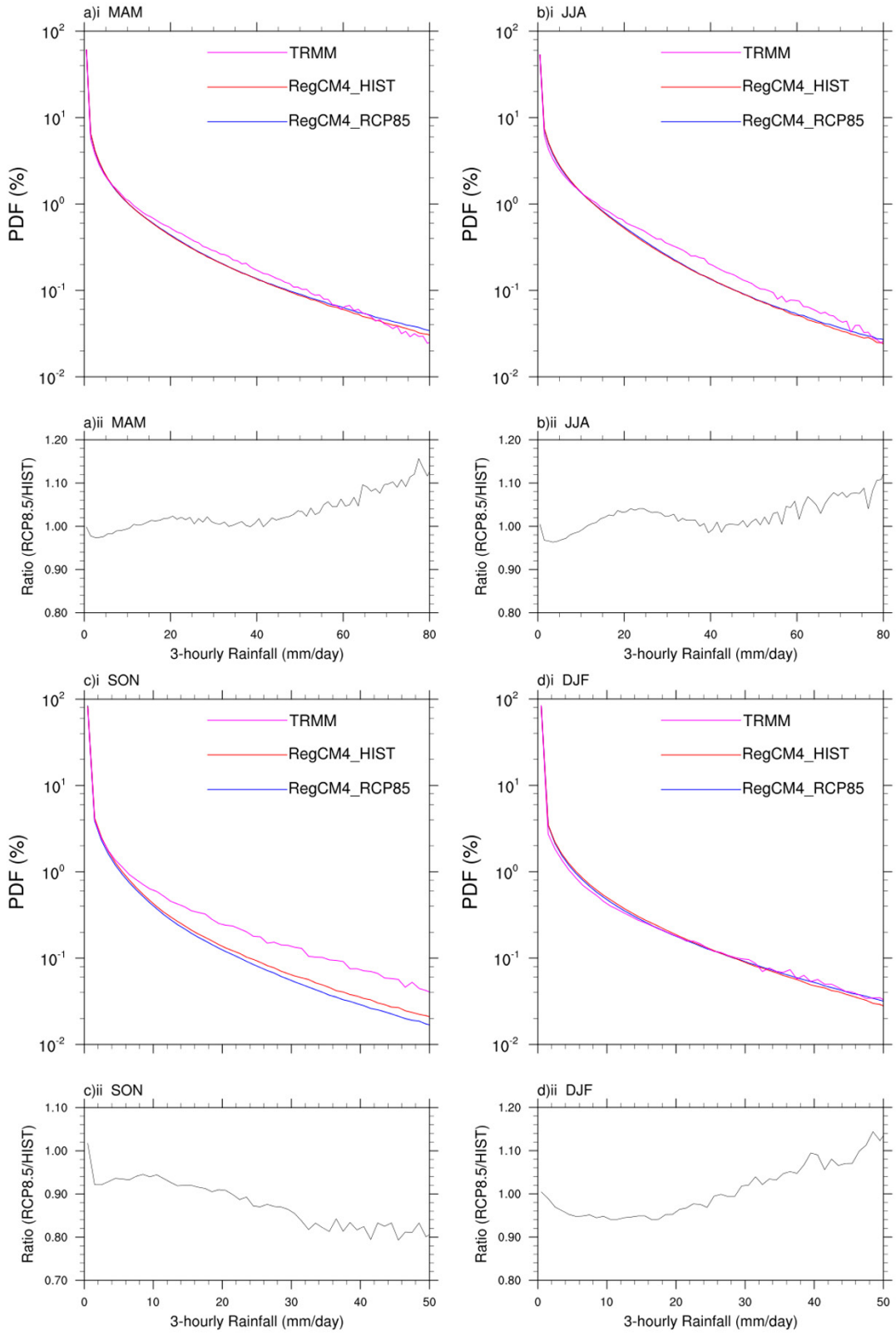


***Figure 6.13*** *Same as* ***Figure 6.1*** *but for 3-hourly rainfalls. RegCM4_GF (RegCM4_AC) is excluded in JJA (SON).*

# 7 Discussions and Conclusion

## 7.1 Discussions

### 7.1.1 Review of GCM selection and dynamical downscaling

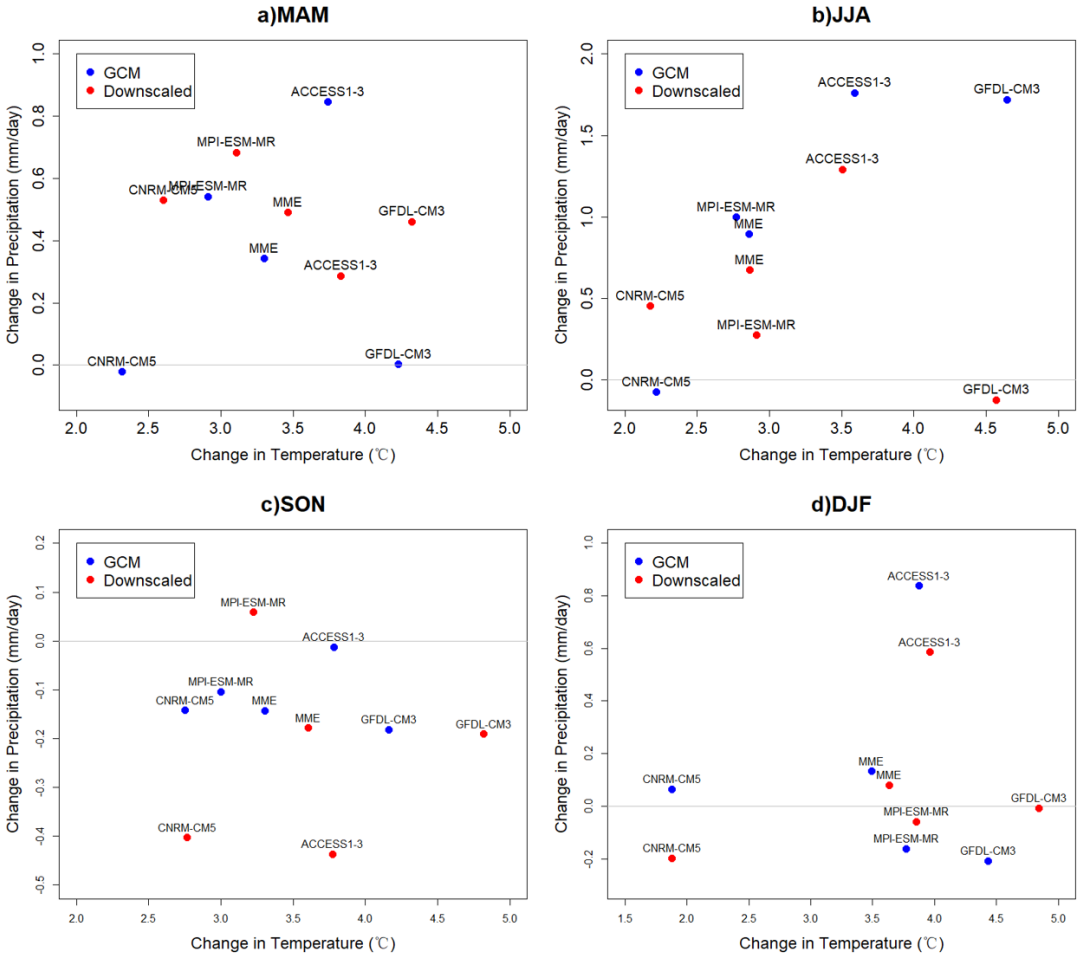


***Figure 7.1*** *Change in seasonal mean 850hPa temperature versus that in precipitation area-averaged over 22 – 30°N, 110 – 120°E between historical and RCP8.5 simulations for (blue dots) the selected GCMs and (red dots) their downscaled products using RegCM4 for (a) MAM, (b) JJA, (c) SON, and (d) DJF. GFDL-CM3 (ACCESS1-3) is excluded from the MME mean for JJA (SON).*

The MME mean of GCMs and their downscaled products provided similar and reasonable projections in temperature and precipitation change for all seasons (***Figure***

***7.1***). The increase in temperature was within the range of about 2 to 4 °C for both GCMs and their downscaled products for all seasons, with the least (most) warming projected by CNRM-CM5 (GFDL-CM3). However, the projected change in precipitation by RegCM4 can deviate quite a bit from the parent GCMs. For example, CNRM-CM5 gives no significant change in precipitation for wet seasons in GCM; while its downscaled product reproduces a rather strong increase (about 0.5 mm/day) instead. For JJA, a positive linear relationship between projected change in precipitation and that in temperature is observed.

Although eight circulation features/variables were examined for selecting GCMs for dynamical downscaling, two (ACCESS1-3 and GFDL-CM3) out of four selected models cannot give reasonable precipitation characteristics in some seasons in their downscaled products. GFDL-CM3 was discarded based on the analysis of the downsclaed JJA climate, because of its poor performance in capturing precipitation and 850hPa zonal wind. The problem seems to be more related to the ability of RegCM4.6 to maintain circulation features in its parent GCM. Note that GFDL-CM3 is the only selected model having poor performance in the JJA mean precipitation (score of 2, see ***Table 2.3***), which is also the only criterion directly related to precipitation. Its ranking would have been lower if more precipitation features had been evaluated or higher weighting had been put into JJA mean precipitation.

For ACCESS1-3, the results were discarded when examining the SON climate because of its strong wet bias. However, none of the selection criteria focuses on SON. Results show that SON is the only season having a robust signal of reduced mean and daily precipitation under the warmer climate. Drought season represented by the CDD is also lengthened in the future. To select models that are capable of reproducing a reasonable trend of the dry season, hydrological characteristics in SON is an important

criterion as well for future investigations.

The independence of GCMs chosen in our study was not evaluated. Potential one-sided bias might be induced if the selected GCMs had correlated bias with each other. Therefore, it is also important to sample uncertainties due to the selected models. A measure quantifying model independence was introduced by Bishop and Abramowitz (2013). GCM selection criteria based on the measure of independence could be included in future studies related to climate model selection.

There are some techniques invoking bias correction of GCMs and RCM. For GCMs used as ICBC of RCM for dynamical downscaling, some bias correction methods were conducted by calibrating GCM outputs based on RCM outputs. For example, Holland et al. (2010) proposed a mean state climate bias correction method by subtracting the difference between the historical mean climate in GCMs and that in RCM from ICBC. As a result, the revised ICBC can retain the climate change signal simulated by GCMs and remove the mean state climate difference between GCMs and RCM. This method is straight forward and was able to achieve better performance on dynamical downscaling the climate over the western North Pacific region. Other bias correction methods focusing on standard deviation (Xu and Yang 2012) and frequency (Rocheta et al. 2017) are also used. For RCM, Teutschbein and Seibert (2012) reduced the bias of RCM by making it resemble observational or reanalysis outputs for hydrological climate change impacts studies. The methods include introducing a threshold for precipitation, statistically modifying the PDF of precipitation, adjusting the time-series of temperature and precipitation, etc. Although bias correction can normally make model simulation results closer to observations and reanalysis data, there is a risk of over-calibration for complex correction methods, leading to results being too ‘artifactual’ and increases uncertainties (Lafon et al. 2013). Nonetheless,

meteorologically consistent and well-justified bias correction methods can be adopted in similar studies because the bias was found to be not negligible over Southern China, especially for GCMs.

7.1.2 Changes in precipitation characteristics in SON

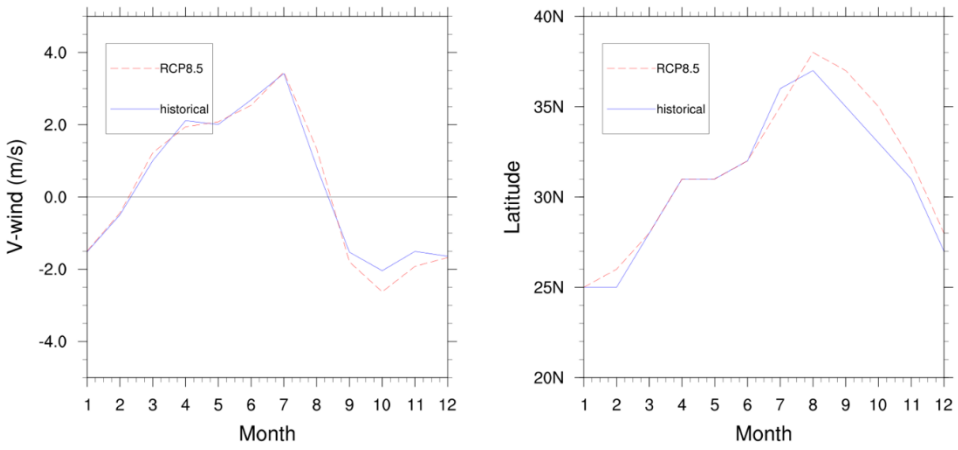


***Figure 7.2*** *Monthly mean of (left) area-averaged 850hPa meridional wind (southerly as positive; units: $ms^{-1}$) over Southern China (20 – 35°N, 115 – 125°E) and (right) latitude with maximum zonally averaged SLP* over the western and central North Pacific (20 – 40°, 150°E – 150°W) from MME mean of GCMs for (solid blue line) historical and (dash red line) RCP8.5.*

SON is projected to be drier over Southern China under RCP8.5. The evidence includes the reduction in mean precipitation rate as well as the suppressed occurrence of rain > 5 mm/day, and also a significantly lengthened CDD. It is found that there is a strengthened northerly over East Asia in RCP8.5 due to a stronger negative SLP* (sea-level pressure deviated from area mean) gradient over there. ***Figure 7.1*** shows the monthly mean area-averaged 850hPa meridional wind over Southern China and latitude with maximum zonally averaged SLP* over the western and central North Pacific from GCMs. Significant strengthened northerly over Southern China is found

in SON only, especially in October and November. In the same period, the maximum SLP*, indicating the position of low-level WPSH, is found at more northern locations in RCP8.5. This result suggests that WPSH tends to stay at a more northern location in SON under a warmer climate before retreating to the southeast in DJF. As a result, anomalous low SLP* will be induced in the future over the southern part of WPSH, consistent with ***Figure 4.13***.

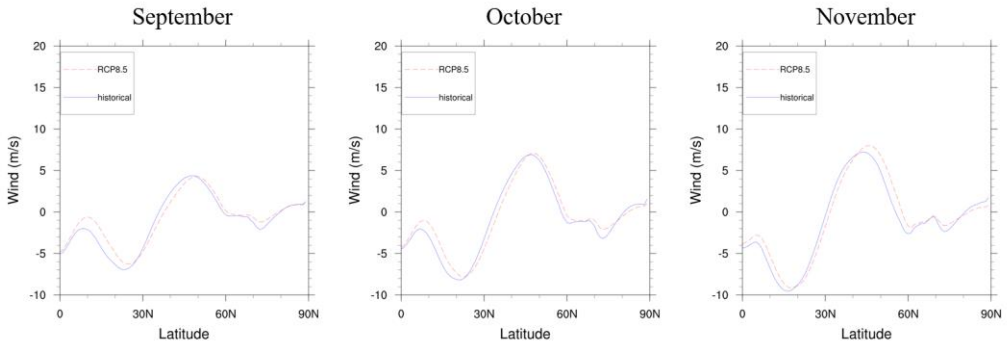


***Figure 7.3*** *Monthly mean longitudinally averaged 1000hPa zonal wind (positive: westerly) over 150°E – 150°W from MME mean of GCMs for (solid blue line) historical and (dash red line) RCP8.5.*

For the northward shift of WPSH in SON, this could be related to the poleward shift of the subtropical jet (Barnes and Polvani 2013). The subtropical jet over the western North Pacific was projected to have a significant poleward displacement under a warmer climate in RCP8.5 based on CMIP5 model outputs, especially in SON. The position of the subtropical jet is correlated to that of the subtropical high. Maher et al. (2020) claimed that the poleward shift of the subtropical jet was also seen in historical observations and was related to the tropical expansion due to global warming. The later is supposed to have the largest effect during summer and autumn over the North Pacific region (Grise et al. 2018). Tropical expansion by about 1 to 2° during SON is also found in our GCM outputs. ***Figure 7.2*** shows the monthly mean longitudinally averaged near-surface zonal wind over the North Pacific (150°E – 150°W), which is

an indicator for the tropical width (Davis and Birner 2017). A similar result is found using the maximum 850hPa zonal wind as the definition of the edge of Hadley cells (Polvani et al. 2011, Davis and Rosenlof 2012). In short, significant tropical expansion during SON is suggested to be the cause of the poleward displacement of the subtropical jet and WPSH. The northward displaced subtropical high and the low-pressure trough in the monsoon area results in the negative SLP* anomaly over the western North Pacific. It induces anomalous northerlies and brings drier climate over Southern China during SON.

### 7.1.3 Issues related to precipitation extremes

95PC was the quantity chosen to represent the magnitude of extreme precipitation in our study. However, 95PC from TRMM and APHRODITE, and also from reference datasets and model outputs are not entirely consistent (see ***Figures 6.2 – 6.5***). From Expert Team on Climate Change Detection and Indices (ETCCDI; http://etccdi.pacificclimate.org/indices.shtml), some other indices including R95pTOT (annual total precipitation amount when rain rate more than 95PC), Rx5day (monthly maximum consecutive 5-day precipitation), R20mm (annual count of days when precipitation amount more than 20mm), etc., can also represent the strength of extreme rainfall. These indices can provide physical information that is not included in 95PC, such as the temporal fraction of heavy rainfall and the strength of consecutive precipitation. On the other hand, RegCM4 was reported to have different performance in simulating different extreme rainfall indices over Southeast Asia (Ngo-Duc et al. 2017). Some indices may give a different or more representative projection of extreme rainfall compared to 95PC. Including more extreme rainfall indices can help provide a more complete picture of extreme rainfall projection in future studies.

The extreme precipitation in SON is also found to be reduced due to global warming.

However, both daily and 3-hourly precipitation from the MME mean outputs are much stronger than both TRMM and APHRODITE for the rain rates > 10 mm/day (see ***Figures 6.1*** and ***6.13***). This overestimation may induce a bias when projecting the changes in the intensity of extreme rainfall. Nonetheless, the signal of a less frequent extreme rainfall over Southern China in SON is still robust.

TC is an important source of extreme rainfall and interannual variability over Southern China. Although RegCM4 can reproduce a reasonable occurrence of heavy rainfall, it should be noticed that TCs in the model would be weaker than reality due to its rather coarse horizontal resolution (25 km × 25 km) and the hydrostatic assumption.

### 7.1.4 Future investigations with improved models

There are several limitations in this study. For example, more than half of the tested GCMs cannot reproduce good climate features over the South China-Western North Pacific region (with the overall score less than 3, see ***Table 2.3***). The performance of GCMs in simulating ENSO and monsoon variability is also generally poor. Datasets of CMIP6, the updated project of CMIP5, have been available since 2019 (https://esgf-node.llnl.gov/projects/cmip6/, Eyring et al. 2016). More realistic simulations of the global climate are expected after the improvement in model physics, such as aerosol, clouds, and land-sea interaction. There are also new future climate scenarios, named shared socioeconomic pathways (SSPs), with societal change included (O'Neill et al. 2016). SSPs combine the possibilities for adaptation of climate change and RCPs to provide a more realistic projection of the future. Future work on the climate projection on the regional climate can be carried out by using CMIP6 models.

In RegCM4, the simulations are limited under a hydrostatic balance assumption, meaning that the horizontal resolution cannot be less than about 10 to 15 km. Some model physics and schemes, developed years ago, in RegCM4 might lead to unrealistic

hydrological features (such as oceanic precipitation over SCS and the diurnal rainfall). RegCM5 will be developed in the near future, with a finer permitted resolution, a non-hydrostatic dynamical core, and a faster running time (http://indico.ictp.it/event/9086/material/poster/0.pdf). RegCM5 is expected to have a better performance in simulating convection and thus improve future research regarding regional precipitation characteristics.

### 7.2 Conclusion

The performance of 22 models from CMIP5 in simulating the circulation elements/features over South China-Western North Pacific region were examined. Among them, four models namely ACCESS1-3, CNRM-CM5, GFDL-CM3, and MPI-ESM-MR were selected for dynamical downscaling using RegCM4.6, for the historical period of 1997 – 2003, and for 2050 – 2099 based on the RCP8.5 over the Southern China domain (see ***Figure 1.1***). The RegCM4 was integrated at the 25km × 25km horizontal resolution and the results were used to investigate future changes in hydrological characteristics in various timescales. RegCM4 was able to reproduce most features in the low-level temperature, wind, and precipitation from observational or reanalysis data; however, the simulated diurnal rainfall cycle was earlier than that in TRMM by about 3 hours. The performance of downscaling was overall acceptable, except ACCESS1-3 (GFDL-CM3) for SON (JJA) climate.

Based on the comparison between the downscaled outputs of models under RCP8.5, the whole domain in the 2050 – 2099 period, according to RCP8.5, was projected to become warmer by 2 to 3 ℃ in MAM and JJA (compared to the 1979 – 2003 era). The warming could exceed 4℃ in the continental area north of 25°N in SON and DJF. Mean precipitation in MAM and JJA (SON) was strengthened (reduced) by 1 to 2

mm/day (about 1 mm/day). Changes in the mean DJF precipitation, under global warming, were negligible. Results from moisture budget analyses suggested that change in vertically integrated moisture flux convergence was responsible for the change in mean precipitation in all seasons. The length of the dry season, as indicated by CDD, showed a robust increase by about 3 to 5 days in the region south of 32°N, covering the whole Southern China. Further investigation on the GCM outputs found that the strengthened dry northerly over East Asia due to the stronger negative pressure gradient was responsible for the drier SON. The anomalous low pressure over the western North Pacific was suggested to be the result of a northward displaced WNPH. Based on the latitudinal profile of the zonally averaged low-level wind from the GCM outputs, there was evidence showing a poleward expansion of tropics in SON over the North Pacific region. The tropical expansion was suggested to be the cause of the northward displaced WNPH and induced the strengthened northerly, which brought a drier SON climate to Southern China.

The interannual seasonal precipitation variability was also investigated using a novel moisture budget analysis method (see **Appendix 4**). The seasonal precipitation variance in MAM (JJA) was found to increase by 15% (30%) under RCP8.5. The projected changes in SON and DJF are rather small. From the moisture budget analysis, the increase in precipitation variance in MAM and JJA were both attributed to dynamical effects. Further breakdown of the dynamical term showed that change in mean background humidity (anomalous wind/moisture flux convergence) was responsible for the increase in the interannual variability in MAM (JJA).

The frequency of daily and 3-hourly precipitation over Southern China did not give a strong difference for light to moderate rainfall. However, the frequency of intense rainfall increased with the rain rate in all seasons, except for SON. The occurrence of

daily and 3-hourly precipitation in SON decreased under RCP8.5 by about 10% to 20% for intense rainfall. On the other hand, the simulated JJA diurnal rainfall showed no significant change under a warmer climate in both the spatiotemporal distribution and strength.

Change in extreme rainfall represented by 95PC was compared with the CC relation. Results show that 95PC has a significant change over Southern China in the wet season (MAM and JJA) only. 95PC in both seasons is projected to increase by 5% per one degree of low-level tropospheric warming, which is consistent with, but slightly less than that given by the CC relation. The change of the 95PC was less regional dependent in JJA than that in MAM.

# Appendix

## 1 CMIP5 model selection details

The classification details of CMIP5 in circulation variables that cannot be merely evaluated by the Taylor diagram is included in this section. In the following, classes of models are represented by four colors, ranging from green (best), yellow, orange to red (worst).

### 1.1 Summer mean precipitation

| Models | Class | Reasons |
|---|---|---|
| ACCESS1-0 | | well simulated features of JJA precipitation over the domain except for the location of ITCZ (125 – 140°E) |
| ACCESS1-3 | | similar to ACCESS1-0, but with biased magnitude and position of the ITCZ |
| bcc-csm1-1 | | unreasonable pattern with an unusual dry zone over Southern China |
| bcc-csm1-1-m | | similar to bcc-csm1-1, but without the “dry zone” |
| CanESM2 | | unreasonable onshore rain magnitude; poorly simulated ITCZ |
| CMCC-CM | | recognizable features, except the local maximum of Southern China |
| CNRM-CM5 | | a similar pattern with the reanalysis, but bias in magnitude |
| CSIRO-Mk3-6-0 | | reasonable pattern and magnitude except over coastal region; ITCZ shifted to the north |
| FGOALS-g2 | | unreasonable pattern over the domain of interest; large “dry zone” in Southern China. |
| GFDL-CM3 | | magnitude too small; unable to simulate local maximum over coastal Southern China. |
| GFDL-ESM2G | | unable to simulate local maximum over the most coastal area |
| GFDL-ESM2M | | similar to GFDL-ESM2G |
| HadGEM2-ES | | pattern and magnitude similar to reference data, except the ITCZ east of 140°E |

| | | |
|---|---|---|
| IPSL-CM5A-LR | | magnitude too small; unable to reproduce a reasonable pattern of rainfall along the coastal area and ITCZ |
| IPSL-CM5A-MR | | a pattern similar to reference data, but with a much smaller magnitude over the coastal area |
| IPSL-CM5B-LR | | similar to GFDL-CM3 |
| MIROC5 | | maximum over Southern China too large; unable to simulate other features properly, especially the ITCZ |
| MIROC-ESM | | unrealistic features nor the pattern compared to reference data |
| MIROC-ESM-CHEM | | similar to MIROC-ESM |
| MPI-ESM-MR | | reasonable magnitude and features; unable to capture local maximum over Southern China. |
| MRI-CGCM3 | | too little overall rainfall; too little rainfall over the continental area. |
| NorESM1-M | | unrealistic features and patterns compared to reference data. |

## 1.2 ENSO-related variability (DJF)

| Models | Class | Reasons |
|---|---|---|
| ACCESS1-0 | | too weak meridional component of the regressed 850hPa wind over Southern China |
| ACCESS1-3 | | similar to ACCESS1-0 |
| bcc-csm1-1 | | similar to ACCESS1-0 |
| bcc-csm1-1-m | | reasonable magnitude and location of the positive stream function |
| CanESM2 | | unable to capture meridional component of regressed 850hPa wind over Southern China |
| CMCC-CM | | too weak regressed wind signal |
| CNRM-CM5 | | similar to bcc-csm1-1-m |
| CSIRO-Mk3-6-0 | | too small magnitude and size of the 850hPa regressed anticyclone |
| FGOALS-g2 | | too strong regressed 850hPa southerly over the coast of Southern China; strong abnormal regressed wind component over Eastern China. |
| GFDL-CM3 | | reasonable magnitude and direction of the regressed 850hPa wind over Southern China |
| GFDL-ESM2G | | similar magnitude of regressed positive stream function compared with reference data but shifted in location |

| | | |
|---|---|---|
| GFDL-ESM2M | | magnitude of 850hPa stream function and wind too strong; pattern of stream function shifted to the southwest |
| HadGEM2-ES | | Unable to reproduce the regressed 850hPa anticyclone |
| IPSL-CM5A-LR | | similar to HadGEM2-ES |
| IPSL-CM5A-MR | | similar to HadGEM2-ES. |
| IPSL-CM5B-LR | | unable to reproduce the regressed 850hPa meridional wind over Southern China. |
| MIROC5 | | unable to obtain any feature due to weak regressed 850hPa wind and anticyclone over the whole domain |
| MIROC-ESM | | too strong regressed 850hPa southwesterly over Southern China, especially on the land area; unexpected regressed 850hPa westerly found over (15 – 30°N) extending from India to central Pacific |
| MIROC-ESM-CHEM | | similar to MIROC-ESM |
| MPI-ESM-MR | | reasonable magnitude and location of the positive stream function, but tilted in a NE-SW fashion |
| MRI-CGCM3 | | similar to IPSL-CM5B-LR |
| NorESM1-M | | reasonable magnitude and location of the positive stream function |

## 1.3 ENSO-related variability (MAM)

| Models | Class | Reasons |
|---|---|---|
| ACCESS1-0 | | regressed 850hPa southwesterly branch over SCS and Southern China shifted to the southeast |
| ACCESS1-3 | | acceptable pattern of the regressed 850hPa wind over Southern China; unable to reproduce regressed 850hPa zonal wind over equatorial Pacific |
| bcc-csm1-1 | | too weak regressed 850hPa wind signal over the domain of interest |
| bcc-csm1-1-m | | reasonable magnitude and location of the positive stream function |
| CanESM2 | | unable to reproduce regressed 850hPa meridional wind over Southern China |
| CMCC-CM | | unexpected regressed 850hPa cyclonic flow shown over Southern China |
| CNRM-CM5 | | regressed 850hPa wind pattern shifted slightly to the south over Southern China; too strong zonal component over SCS |
| CSIRO-Mk3-6-0 | | regressed 850hPa wind pattern shifted slightly to the south over Southern China |

| | | |
|---|---|---|
| FGOALS-g2 | | well simulated pattern of regressed 850hPa wind but with a stronger magnitude |
| GFDL-CM3 | | similar to CSIRO-Mk3-6-0 |
| GFDL-ESM2G | | similar to CNRM-CM5 |
| GFDL-ESM2M | | similar to FGOALS-g2 |
| HadGEM2-ES | | similar to CSIRO-Mk3-6-0 |
| IPSL-CM5A-LR | | unable to generate a reasonable magnitude of regressed 850hPa wind; no expected feature can be observed over the domain of interest |
| IPSL-CM5A-MR | | similar to IPSL-CM5A-LR |
| IPSL-CM5B-LR | | well simulated regressed 850hPa wind over Southern China but with unreasonable pattern south of Japan |
| MIROC5 | | regressed 850hPa stream function over the whole domain shifted slightly to the southeast over Southern China and SCS |
| MIROC-ESM | | too strong regressed 850hPa meridional wind over Southern China, especially over the land area; anticyclone on the same level shifted to the southeast |
| MIROC-ESM-CHEM | | similar to MIROC-ESM |
| MPI-ESM-MR | | magnitude of the regressed 850hPa wind and stream function over SCS too strong |
| MRI-CGCM3 | | reasonable magnitude and location of the positive stream function |
| NorESM1-M | | too strong regressed 850hPa zonal wind |

## 1.4 East Asian summer monsoon variability

| Models | Class | Reasons |
|---|---|---|
| ACCESS1-0 | | magnitude of both regressed 850hPa wind and precipitation over the domain of interest too large |
| ACCESS1-3 | | reasonable magnitude and pattern of regressed 850hPa wind and precipitation |
| bcc-csm1-1 | | similar to ACCESS1-3 |
| bcc-csm1-1-m | | similar to ACCESS1-3 |
| CanESM2 | | regressed maps of circulation variables too weak, especially precipitation; suppressed regressed precipitation over coastal Southern China |

| | | |
|---|---|---|
| CMCC-CM | | magnitude of regressed 850hPa wind too weak; too heavy precipitation |
| CNRM-CM5 | | similar to ACCESS1-3 |
| CSIRO-Mk3-6-0 | | magnitude of regressed 850hPa wind too weak; too heavy precipitation; structure of 850hPa anti-cyclone unable to extend to the north |
| FGOALS-g2 | | well simulated pattern with a slight deformation in the structure |
| GFDL-CM3 | | well simulated pattern; with a smaller magnitude |
| GFDL-ESM2G | | too weak regressed precipitation and 850hPa wind over continent; size of the regressed 850hPa anticyclone too small |
| GFDL-ESM2M | | similar to ACCESS1-3 |
| HadGEM2-ES | | northeast shifted pattern, with a stronger magnitude. |
| IPSL-CM5A-LR | | unable to give the positive regressed precipitation over 20 – 35°N |
| IPSL-CM5A-MR | | slightly deformed and tilted structure of regressed of 850hPa anticyclone and precipitation |
| IPSL-CM5B-LR | | similar to IPSL-CM5A-LR |
| MIROC5 | | too heavy regressed precipitation; unable to reproduce a clear 850hPa regressed anticyclone structure; magnitude of regressed 850hPa wind too weak. |
| MIROC-ESM | | unable to general a reasonable structure of regressed 850hPa wind and precipitation |
| MIROC-ESM-CHEM | | similar to MIROC-ESM |
| MPI-ESM-MR | | similar to ACCESS1-3 |
| MRI-CGCM3 | | similar to ACCESS1-3 |
| NorESM1-M | | similar to ACCESS1-3 |

## 1.5 East Asian winter monsoon variability

| Models | Class | Reasons |
|---|---|---|
| ACCESS1-0 | | reasonable pattern and magnitude of regressed 850hPa temperature and wind |
| ACCESS1-3 | | similar to ACCESS1-0 |
| bcc-csm1-1 | | too strong regressed 850hPa northeasterly over southeastern China; unable to reproduce the northwesterly branch over northwestern Pacific |

| | | |
|---|---|---|
| bcc-csm1-1-m | | similar to ACCESS1-0 |
| CanESM2 | | too weak regressed 850hPa wind; northwesterly branch over Korea and Japan shifted to the northeast. |
| CMCC-CM | | unable to generate the regressed 850hPa northeasterly over southeastern China, an important component for winter monsoon variability |
| CNRM-CM5 | | far too strong regressed 850hPa wind with reasonable patterns |
| CSIRO-Mk3-6-0 | | similar to CMCC-CM |
| FGOALS-g2 | | well simulated pattern of regressed 850hPa wind and temperature; the whole pattern shifted towards the inland area |
| GFDL-CM3 | | too low regressed 850hPa temperature |
| GFDL-ESM2G | | similar to CMCC-CM |
| GFDL-ESM2M | | similar to CMCC-CM |
| HadGEM2-ES | | regressed 850hPa northeasterly only found over the continental area over southeastern China; too low regressed 850hPa temperature over the continent |
| IPSL-CM5A-LR | | too low regressed 850hPa temperature over the continent |
| IPSL-CM5A-MR | | regressed 850hPa northeasterly branch over Southern China shifted far northern; too low regressed temperature over the continent |
| IPSL-CM5B-LR | | too low regressed 850hPa temperature over the continent |
| MIROC5 | | unable to simulate the 850hPa northwesterly branch over mid-latitude east Asia; regressed 850hPa cold signal over the mid-latitude Asian continent too weak and small in size |
| MIROC-ESM | | similar to MIROC5; able to simulate a weak 850hPa northeasterly branch |
| MIROC-ESM-CHEM | | magnitude of regressed 850hPa temperature too weak; too strong meridional component of regressed 850hPa northeasterly |
| MPI-ESM-MR | | similar to ACCESS1-0 |
| MRI-CGCM3 | | similar to ACCESS1-0 |
| NorESM1-M | | magnitude of regressed 850hPa wind too strong |

## 2 Results of simulated variables in multi-model ensemble averages

### 2.1 Mean 850hPa temperature and wind

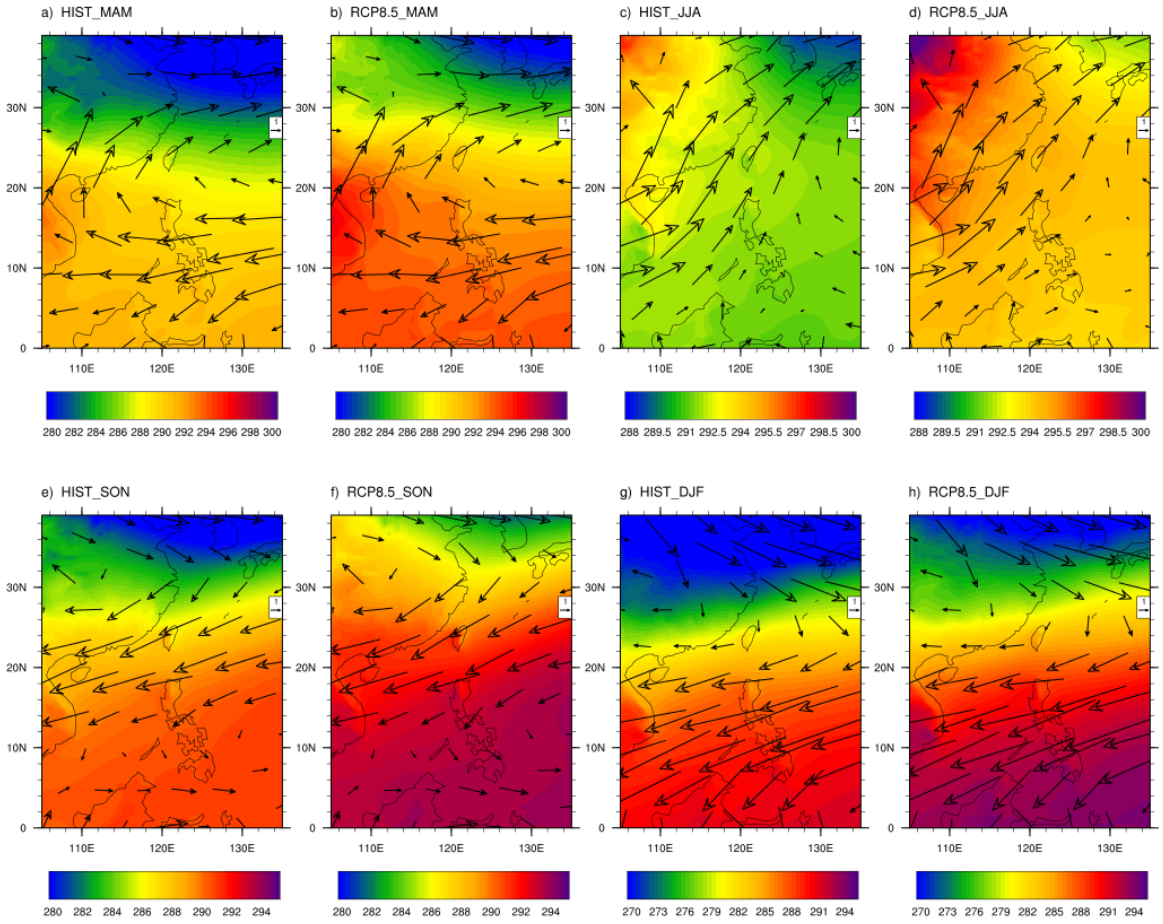


***Figure A1*** *850hPa temperature (shading, units: K) and wind (arrows, units:ms$^{-1}$) for (a, c, e, g) MME_HIST and (b, d, f, h) MME_RCP8.5 in (a, b) MAM, (c, d) JJA, (e, f) SON, and (g, h) DJF. RegCM4_GF(RegCM4_AC) is excluded for JJA(SON).*

MME_HIST gives results with both patterns and magnitudes similar to those from RegCM4_EA in all four seasons, which indicates MME can effectively reduce the bias from GCMs (***Figure A1***).

2.2 Mean precipitation, evaporation and vertically integrated moisture flux convergence

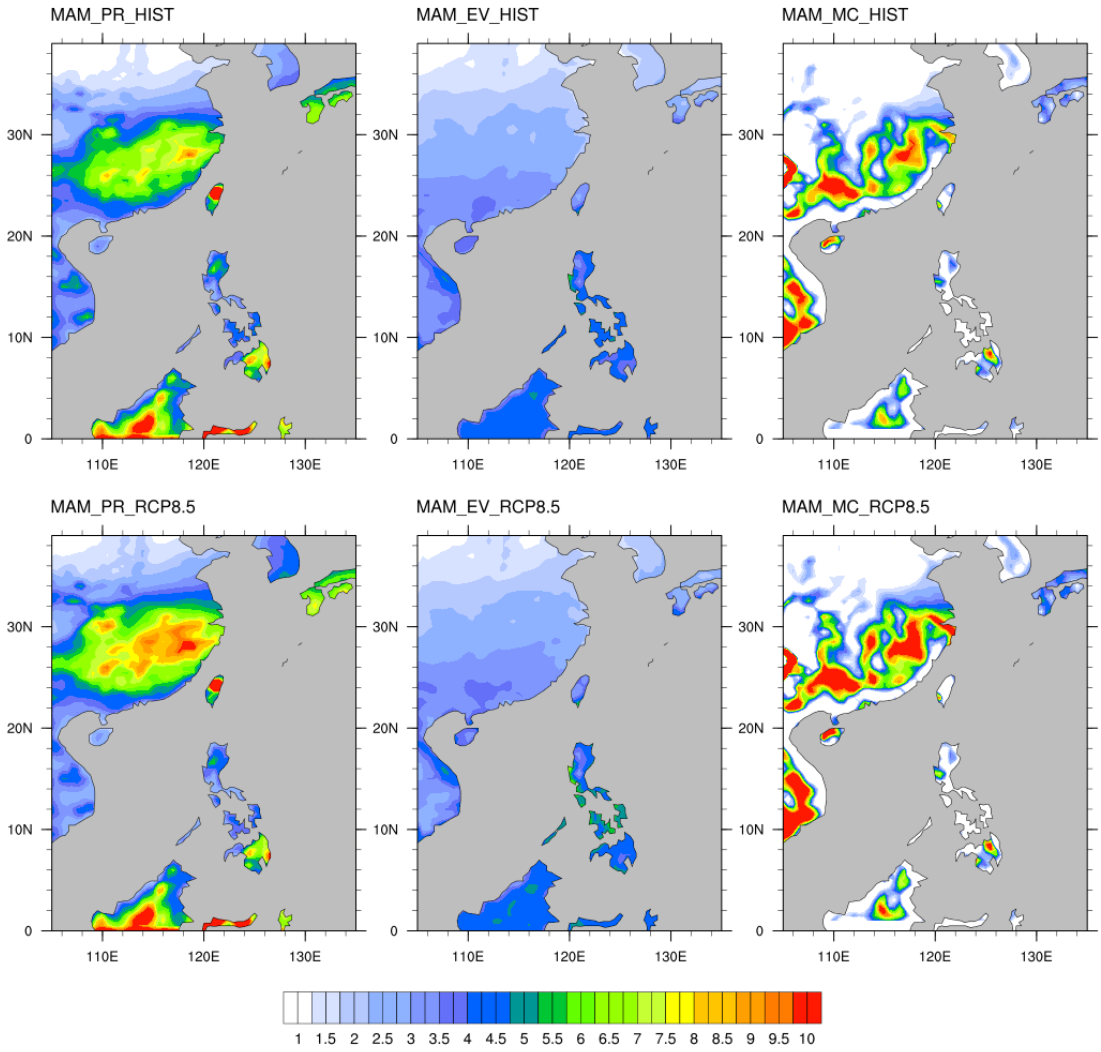


***Figure A2*** *MAM mean (left column) precipitation* $\bar{P}$*, (middle column) evaporation* $\bar{E}$ *and (right column) vertically integrated moisture flux convergence for (top) MME_HIST and (bottom) MME_RCP8.5, with all units converted into mm/day.*

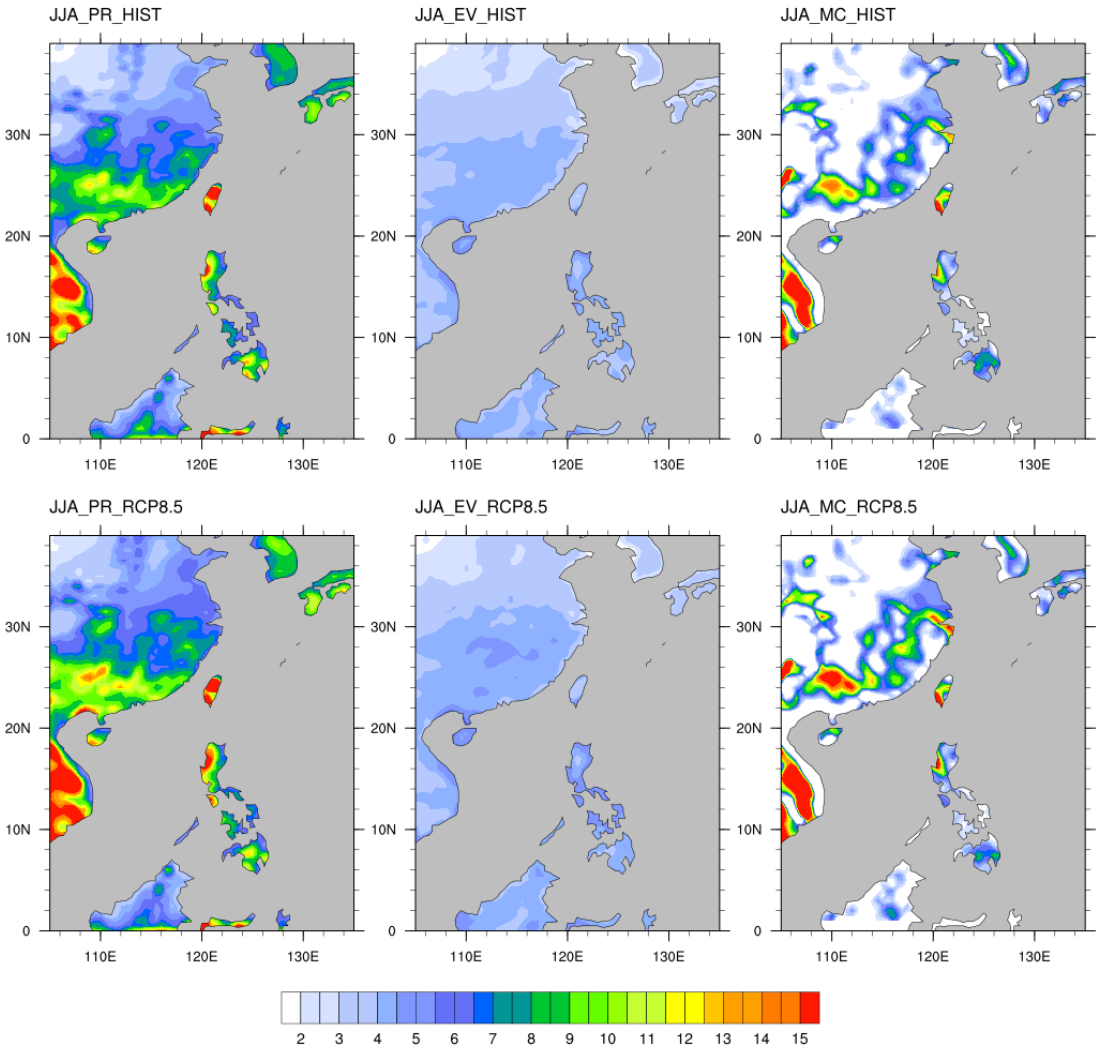


***Figure A3*** *Same as* ***Figure A4*** *but for JJA. RegCM4_GF is excluded.*

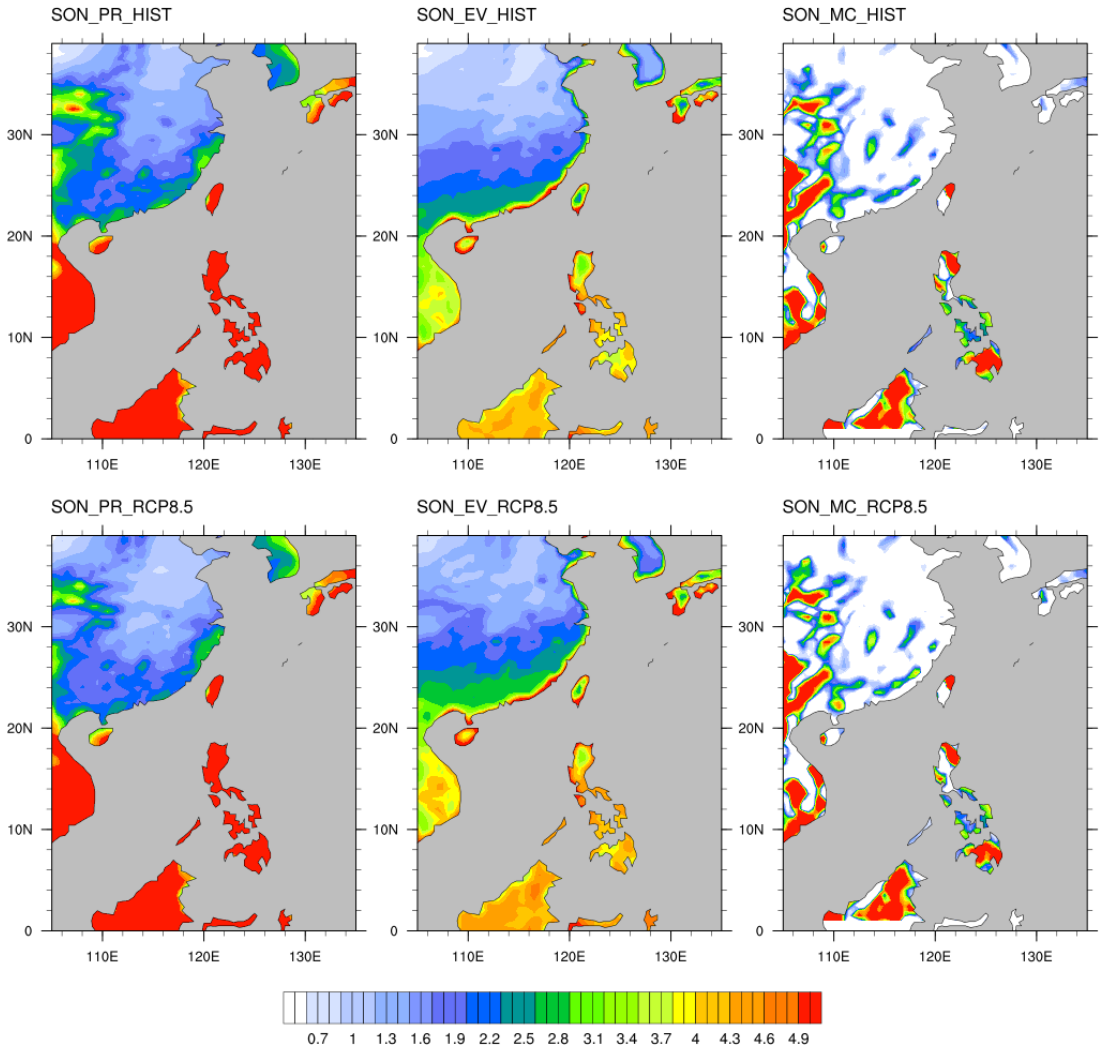


***Figure A4*** *Same as* ***Figure A4*** *but for SON. RegCM4_AC is excluded.*

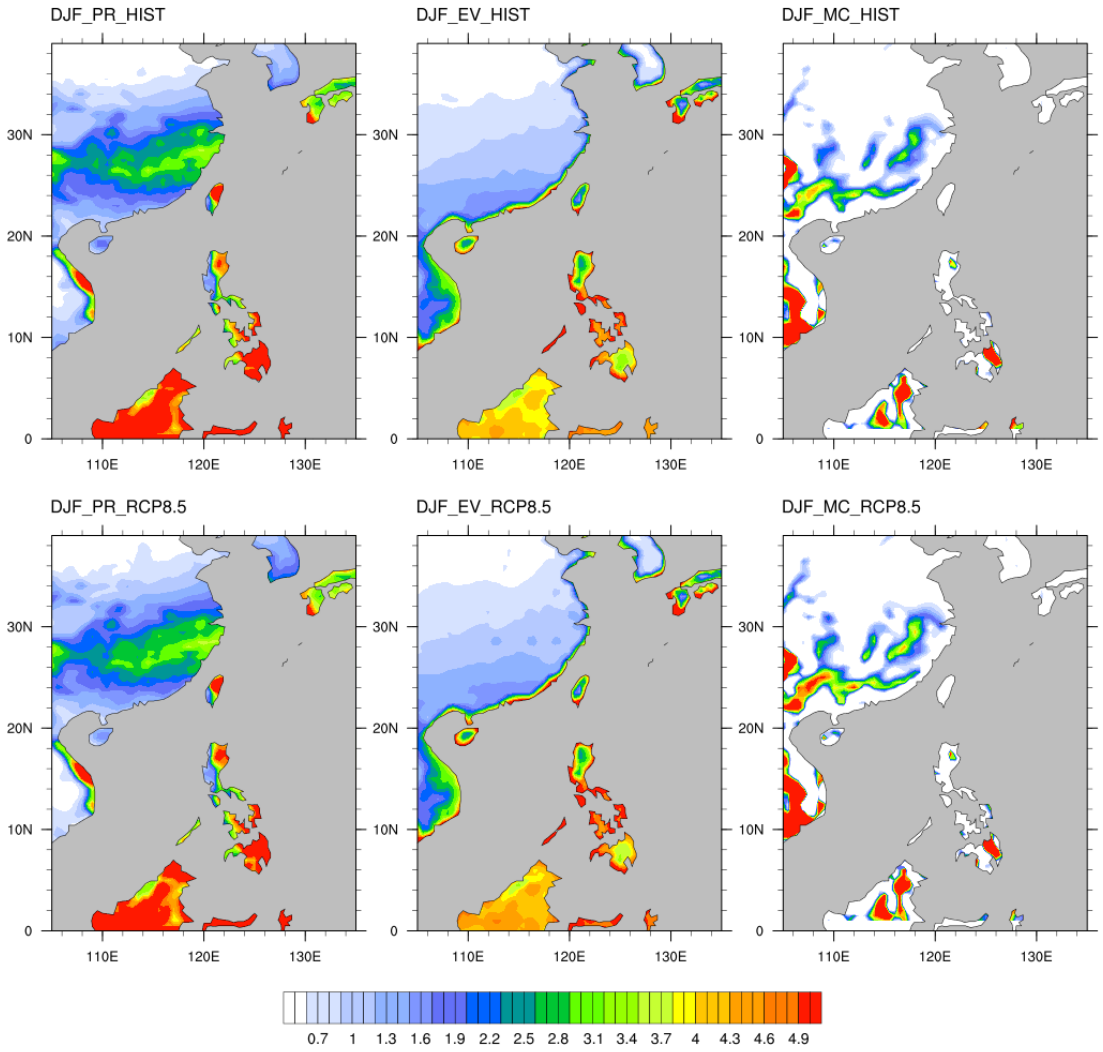


***Figure A5*** *Same as* ***Figure A4*** *but for DJF.*

Seasonal mean precipitation simulated in MME_HIST has patterns and magnitudes comparable to RegCM4_EA. Mean precipitation in MAM (***Figure A2***) has a smaller magnitude in MME_HIST than RegCM4_EA, which is closer to that in TRMM. In JJA (***Figure A3***), the rain belt over Southern China has a clear feature in MME_HIST. The rain belt can extend to the coast with a similar magnitude to TRMM. Precipitation in SON (***Figure A4***) and DJF (***Figure A5***) from MME_HIST resembles that from RegCM4_EA. The wet bias remains in MME_HIST compared to the reference data. Evaporation is rather small except for SON. Vertically integrated moisture flux

convergence contributes to most of the seasonal mean precipitation except for SON.

## 3 Consecutive dry days in GCMs

The maps of MME average CDD calculated from the four selected raw GCMs with its mean start date and end date are shown in ***Figure A6*** – ***A8***. A lengthened CDD over Southern China is also projected by the raw GCMs. However, changes in the start date and the end date of CDD south of 30°N are opposite to those in downscaled products: in GCMs both the start date and the end date postpone in the future simulations with a stronger delay in the end date.

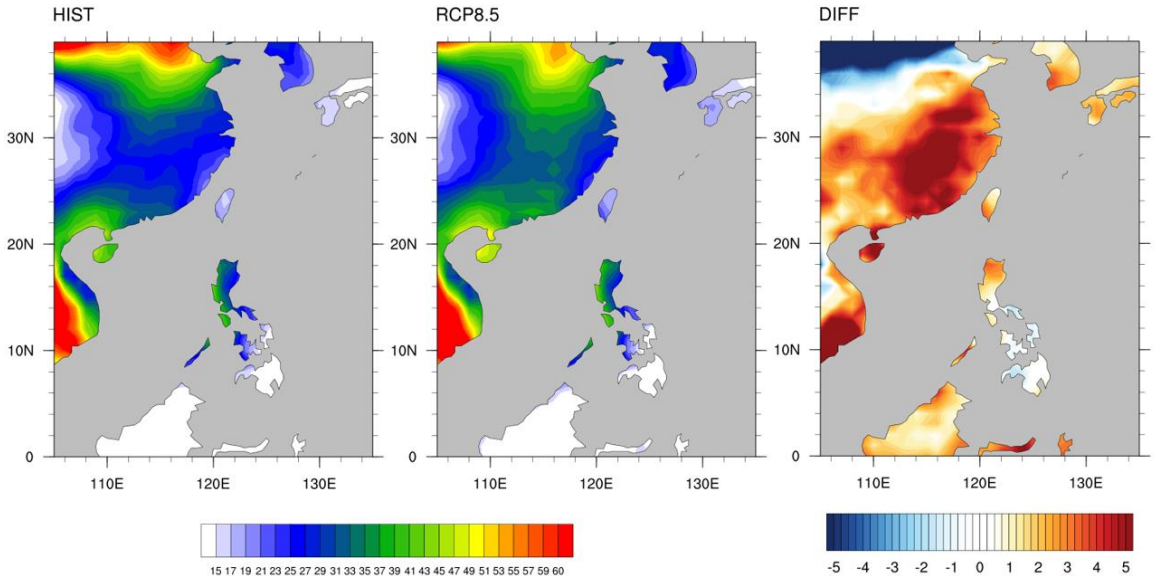


***Figure A6*** *MME mean annual maximum consecutive dry days (units: days) calculated from the four selected GCMs for (left) historical, (middle) RCP8.5 simulations and (right) their difference.*

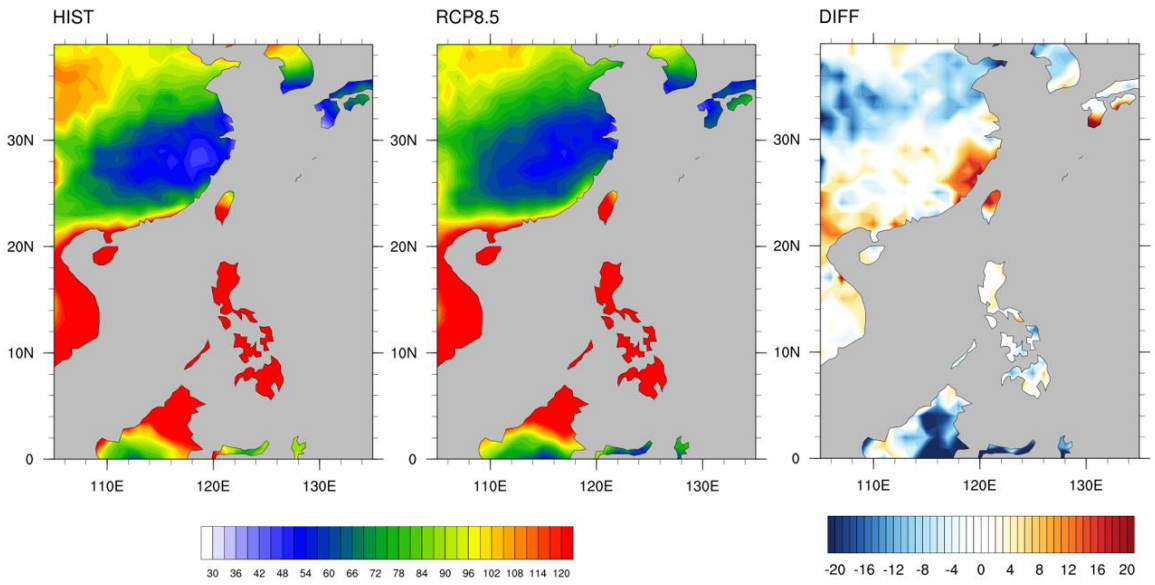


***Figure A7*** *MME mean annual start date of the maximum consecutive dry days (units: days after 1st September) calculated from the four selected GCMs for (left) historical, (middle) RCP8.5 simulations, and (right) their difference.*

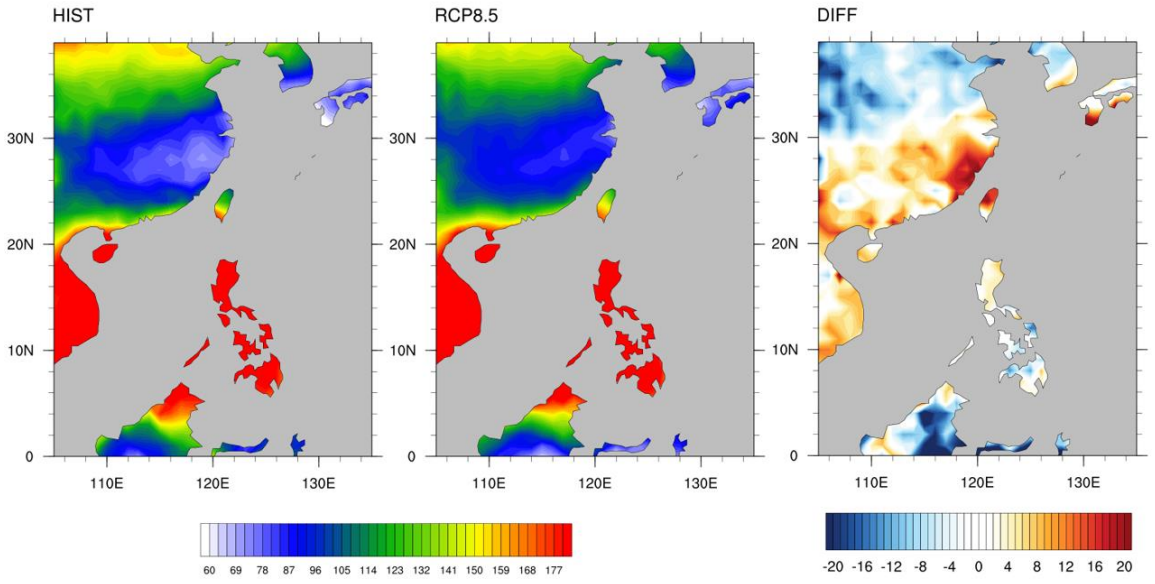


***Figure A8*** *Similar* ***Figure A7*** *but for the end date.*

## 4 Calculation of vertically integrated moisture flux convergence for interannual precipitation variability

From equation 5.2:

$$\overline{|P'|} = \overline{\hat{P}'E'} - \overline{\hat{P}'\left(\frac{1}{g}\nabla\cdot\int_0^{p_s} q\boldsymbol{V}dp\right)'}$$

$$\left(\int_0^{p_s} q\boldsymbol{V}\,dp\right)' = \int_0^{p_s}(\bar{q}\boldsymbol{V}' + q'\overline{\boldsymbol{V}} + q'\boldsymbol{V}' - \overline{q'\boldsymbol{V}'})dp$$

The last two terms are in higher orders, after rejecting them we get

$$\overline{|P'|} \approx \overline{\hat{P}'E'} - \overline{\hat{P}'\frac{1}{g}\nabla\cdot\int_0^{p_s}(\bar{q}\boldsymbol{V}' + q'\overline{\boldsymbol{V}})dp},$$

where $\bar{q}\boldsymbol{V}'$ and $q'\overline{\boldsymbol{V}}$ are two terms related to the deviation in velocity and specific humidity respectively. One can interpret $\bar{q}\boldsymbol{V}'$ as the dynamical effect while $q'\overline{\boldsymbol{V}}$ as the thermodynamic effect contributing to the interannual variability of seasonal precipitation. The change in the dynamical term $-\overline{\hat{P}'\frac{1}{g}\nabla\cdot\int_0^{p_s}\bar{q}\boldsymbol{V}'dp}$ from historical simulations to future simulations can be further decomposed through:

$$\delta\left(-\overline{\hat{P}'\times\left(\frac{1}{g}\nabla\cdot\int_0^{p_s}(\bar{q}\boldsymbol{V}')\,dp\right)}\right)$$

$$\approx -\delta\left(\frac{1}{g}\int_0^{\overline{p_{s_H}}}\overline{\hat{P}'\nabla\cdot(\bar{q}\boldsymbol{V}')}\,dp\right)$$

$$= -\left(\frac{1}{g}\delta\int_0^{\overline{p_{s_H}}}\left(\overline{\hat{P}'\boldsymbol{V}'\cdot\nabla(\bar{q})} + \overline{\hat{P}'\bar{q}\nabla\cdot\boldsymbol{V}'}\right)dp\right)$$

$$\approx -\frac{1}{g}\int_0^{\overline{p_{s_H}}}\left(\overline{\hat{P}'_H\nabla\cdot(\delta\bar{q}\boldsymbol{V}'_H)} + \delta\left(\overline{\hat{P}'\boldsymbol{V}'}\right)\cdot\nabla(\overline{q_H}) + q_H\delta\left(\overline{\hat{P}'\nabla\cdot\boldsymbol{V}'}\right)\right)dp,$$

where $\delta(\cdot) = (\cdot)_F - (\cdot)_H$ indicates the change in quantities under the warmer climate, with subscripts $H$ and $F$ denote the quantities from historical and future simulations.

The three terms in the integral, $\overline{\widehat{P}'_H \nabla \cdot (\delta \bar{q} \boldsymbol{V}'_H)}$, $\delta\left(\overline{\widehat{P}' \boldsymbol{V}'}\right) \cdot \nabla(\overline{q_H})$ and $q_H \delta\left(\overline{\widehat{P}' \nabla \cdot \boldsymbol{V}'}\right)$, represent the contributions from changing background specific humidity, wind deviation correlated with precipitation parallel to the specific humidity gradient (i.e. moisture advection), and anomalous wind divergence correlated with precipitation respectively.

# Bibliography


Annamalai, H., & Sperber, K. R. (2016). South Asian summer monsoon variability in a changing climate. *The Monsoons and Climate Change* (pp. 25-46). Springer, Cham.

Anthes, R. A. (1977). A cumulus parameterization scheme utilizing a one-dimensional cloud model. *Monthly Weather Review*, *105*(3), 270-286.

Bamston, A. G., Chelliah, M., & Goldenberg, S. B. (1997). Documentation of a highly ENSO-related SST region in the equatorial Pacific: Research note. *Atmosphere-ocean*, *35*(3), 367-383.

Barnes, E. A., & Polvani, L. (2013). Response of the midlatitude jets, and of their variability, to increased greenhouse gases in the CMIP5 models. *Journal of Climate, 26*(18), 7117-7135.

Beniston, M., Stephenson, D. B., Christensen, O. B., Ferro, C. A., Frei, C., Goyette, S., ... & Palutikof, J. (2007). Future extreme events in European climate: an exploration of regional climate model projections. *Climatic change*, *81*(1), 71-95.

Bishop, C. H., & Abramowitz, G. (2013). Climate model dependence and the replicate Earth paradigm. *Climate dynamics, 41*(3-4), 885-900.

Bjerknes, J. (1966). A possible response of the atmospheric Hadley circulation to equatorial anomalies of ocean temperature. *Tellus*, 18(4), 820-829.

Cai, W., Santoso, A., Wang, G., Yeh, S. W., An, S. I., Cobb, K. M., ... & Lengaigne, M. (2015). ENSO and greenhouse warming. *Nature Climate Change*, *5*(9), 849-859.

Camargo, S. J., & Sobel, A. H. (2005). Western North Pacific tropical cyclone intensity and ENSO. *Journal of Climate, 18*(15), 2996-3006.

Camp, J., Roberts, M. J., Comer, R. E., Wu, P., MacLachlan, C., Bett, P. E., ... & Chan, J. C. (2019). The western Pacific subtropical high and tropical cyclone landfall: Seasonal forecasts using the Met Office GloSea5 system. *Quarterly Journal of the Royal Meteorological Society, 145*(718), 105-116.

Collins, M., An, S. I., Cai, W., Ganachaud, A., Guilyardi, E., Jin, F. F., ... & Vecchi, G. (2010). The impact of global warming on the tropical Pacific Ocean and El

Niño. *Nature Geoscience*, *3*(6), 391-397.

Chang, C. P., Zhang, Y., & Li, T. (2000). Interannual and interdecadal variations of the East Asian summer monsoon and tropical Pacific SSTs. Part I: Roles of the subtropical ridge. *Journal of Climate, 13*(24), 4310-4325.

Chen, G., Sha, W., & Iwasaki, T. (2009). Diurnal variation of precipitation over southeastern China: Spatial distribution and its seasonality. *Journal of Geophysical Research: Atmospheres*, *114*(D13).

Chen, X., Zhang, F., & Zhao, K. (2016). Diurnal variations of the land–sea breeze and its related precipitation over South China. *Journal of the Atmospheric Sciences*, *73*(12), 4793-4815.

Christensen, J. H., Kanikicharla, K. K., Aldrian, E., An, S. I., Cavalcanti, I. F. A., De Castro, M., ... & Kitoh, A. (2013). Climate phenomena and their relevance for future regional climate change. In *Climate Change 2013 the Physical Science Basis: Working Group I Contribution to the Fifth Assessment Report of the Intergovernmental Panel on Climate Change* (pp. 1217-1308). Cambridge University Press.

Dai, A. (2001). Global precipitation and thunderstorm frequencies. Part II: Diurnal variations. *Journal of Climate, 14*(6), 1112-1128.

Davis, N., & Birner, T. (2017). On the discrepancies in tropical belt expansion between reanalyses and climate models and among tropical belt width metrics. *Journal of Climate, 30*(4), 1211-1231.

Davis, S. M., & Rosenlof, K. H. (2012). A multidiagnostic intercomparison of tropical-width time series using reanalyses and satellite observations. *Journal of Climate, 25*(4), 1061-1078.

Easterling, D. R., Meehl, G. A., Parmesan, C., Changnon, S. A., Karl, T. R., & Mearns, L. O. (2000). Climate extremes: observations, modeling, and impacts. *science*, *289*(5487), 2068-2074.

Emanuel, K. A. (1991). A scheme for representing cumulus convection in large-scale models. *Journal of the Atmospheric Sciences*, *48*(21), 2313-2329.

Eyring, V., Bony, S., Meehl, G. A., Senior, C. A., Stevens, B., Stouffer, R. J., & Taylor, K. E. (2016). Overview of the Coupled Model Intercomparison Project Phase 6 (CMIP6) experimental design and organization. *Geoscientific Model Development*, 9(5), 1937-1958.

——, & Živković-Rothman, M. (1999). Development and evaluation of a convection scheme for use in climate models. *Journal of the Atmospheric Sciences*, *56*(11), 1766-1782.

Giorgi, F. (2019). Thirty years of regional climate modeling: where are we and where are we going next?. *Journal of Geophysical Research: Atmospheres*, *124*(11), 5696-5723.

——, Coppola, E., Solmon, F., Mariotti, L., Sylla, M. B., Bi, X., ... & Turuncoglu, U. U. (2012). RegCM4: model description and preliminary tests over multiple CORDEX domains. *Climate Research*, *52*, 7-29.

——, Jones, C., & Asrar, G. R. (2009). Addressing climate information needs at the regional level: the CORDEX framework. *World Meteorological Organization (WMO) Bulletin*, *58*(3), 175.

Gebremichael, M., Vivoni, E. R., Watts, C. J., & Rodríguez, J. C. (2007). Submesoscale spatiotemporal variability of North American monsoon rainfall over complex terrain. *Journal of climate, 20*(9), 1751-1773.

Grell, G. A. (1993). Prognostic evaluation of assumptions used by cumulus parameterizations. *Monthly Weather Review*, *121*(3), 764-787.

Grise, K. M., Davis, S. M., Staten, P. W., & Adam, O. (2018). Regional and seasonal characteristics of the recent expansion of the tropics. *Journal of Climate, 31*(17), 6839-6856.

Gu, H., Wang, G., Yu, Z., & Mei, R. (2012). Assessing future climate changes and extreme indicators in east and south Asia using the RegCM4 regional climate model. *Climatic Change*, *114*(2), 301-317.

Hirose, M., & Nakamura, K. (2005). Spatial and diurnal variation of precipitation systems over Asia observed by the TRMM Precipitation Radar. *Journal of Geophysical Research: Atmospheres*, *110*(D5).

Holtslag, A. A. M., De Bruijn, E. I. F., & Pan, H. L. (1990). A high resolution air mass transformation model for short-range weather forecasting. *Monthly Weather Review*, *118*(8), 1561-1575.

Hong Kong Observatory (HKO). (2019, December 6). Frequency and Total Duration of Display of Tropical Cyclone Warning Signals :1956 – 2018. Retrieved from https://www.hko.gov.hk/en/informtc/historical_tc/fttcw.htm. [accessed 2 June 2020]

Hong, J. Y., Ahn, J. B., & Jhun, J. G. (2017). Winter climate changes over East Asian region under RCP scenarios using East Asian winter monsoon indices. *Climate Dynamics, 48*(1-2), 577-595.

Huang, W. R., & Chen, K. C. (2015). Trends in pre-summer frontal and diurnal rainfall activities during 1982–2012 over Taiwan and Southeast China: characteristics and possible causes. *International Journal of Climatology*, *35*(9), 2608-2619.

——, & Chan, J. C. (2012). Seasonal variation of diurnal and semidiurnal rainfall over Southeast China. *Climate dynamics*, 39(7-8), 1913-1927.

Huang, X., Tan, H., Zhou, J., Yang, T., Benjamin, A., Wen, S. W., ... & Li, X. (2008). Flood hazard in Hunan province of China: an economic loss analysis. *Natural Hazards, 47*(1), 65-73.

Huang, X., Wang, D., Liu, Y., Feng, Z., & Wang, D. (2018). Evaluation of extreme precipitation based on satellite retrievals over China. *Frontiers of Earth Science*, *12*(4), 846-861.

Huffman, G. J., Adler, R. F., Bolvin, D. T., & Nelkin, E. J. (2010). The TRMM multi-satellite precipitation analysis (TMPA). *In Satellite rainfall applications for surface hydrology* (pp. 3-22). Springer, Dordrecht.

Ichikawa, H., & Yasunari, T. (2006). Time–space characteristics of diurnal rainfall over Borneo and surrounding oceans as observed by TRMM-PR. *Journal of Climate, 19*(7), 1238-1260

**IPCC**. (2014): *Climate Change 2014: Impacts, Adaptation, and Vulnerability. Part A: Global and Sectoral Aspects. Contribution of Working Group II to the Fifth Assessment Report of the Intergovernmental Panel on Climate Change* [Field, C.B., V.R. Barros, D.J. Dokken, K.J. Mach, M.D. Mastrandrea, T.E. Bilir, M. Chatterjee, K.L. Ebi, Y.O. Estrada, R.C. Genova, B. Girma, E.S. Kissel, A.N. Levy, S. MacCracken, P.R. Mastrandrea, and L.L. White (eds.)]. Cambridge University Press, Cambridge, United Kingdom and New York, NY, USA, 1132 pp.

Jiang, H., & Zipser, E. J. (2010). Contribution of tropical cyclones to the global precipitation from eight seasons of TRMM data: Regional, seasonal, and interannual variations. *Journal of Climate*, *23*(6), 1526-1543.

Lam, H., Kok, M. H., & Shum, K. K. Y. (2012). Benefits from typhoons–the Hong Kong perspective. *Weather*, 67(1), 16-21.

Laprise, R., Hernández-Díaz, L., Tete, K., Sushama, L., Šeparović, L., Martynov, A., ... & Valin, M. (2013). Climate projections over CORDEX Africa domain using the fifth-generation Canadian Regional Climate Model (CRCM5). *Climate Dynamics, 41*(11-12), 3219-3246.

Lau, K. M., & Yang, S. (1997). Climatology and interannual variability of the Southeast Asian summer monsoon. *Advances in Atmospheric Sciences, 14*(2), 141-162.

Li, C., & Yanai, M. (1996). The onset and interannual variability of the Asian summer monsoon in relation to land–sea thermal contrast. *Journal of Climate, 9*(2), 358-375.

Li, J., Wu, Z., Jiang, Z., & He, J. (2010). Can global warming strengthen the East Asian summer monsoon?. *Journal of Climate*, *23*(24), 6696-6705.

Li, K., Wu, S., Dai, E., & Xu, Z. (2012). Flood loss analysis and quantitative risk assessment in China. *Natural Hazards, 63*(2), 737-760.

Li, Y. B., Tam, C. Y., Huang, W. R., Cheung, K. K., & Gao, Z. (2016). Evaluating the impacts of cumulus, land surface and ocean surface schemes on summertime rainfall simulations over East-to-southeast Asia and the western north Pacific by RegCM4. *Climate dynamics*, *46*(7-8), 2487-2505.

Liang, X. Z., Li, L., Dai, A., & Kunkel, K. E. (2004). Regional climate model simulation of summer precipitation diurnal cycle over the United States. *Geophysical Research Letters*, *31*(24).

Liu, C. M., Wu, M. C., Paul, S., Chen, Y. C., Lin, S. H., Lin, W. S., ... & Chen, C. T. (2011). Super-ensemble of three RCMs for climate projection over East Asia and Taiwan. *Theoretical and applied climatology, 103*(1-2), 265-278.

Lui, Y. S., Tam, C. Y., Au-Yeung, Y. M., & Lau, N. C. (2019a). Role of cumulus parameterization on the seasonal and diurnal precipitation over Southeast Asia in RegCM4. *Climate Dynamics*, *52*(11), 6357-6375.

——, ——, & Lau, N. C. (2019b). Future changes in Asian summer monsoon precipitation extremes as inferred from 20-km AGCM simulations. *Climate Dynamics*, *52*(3-4), 1443-1459.

Lyu, H. M., Xu, Y. S., Cheng, W. C., & Arulrajah, A. (2018). Flooding hazards across southern China and prospective sustainability measures. *Sustainability, 10*(5), 1682.

Maher, P., Kelleher, M. E., Sansom, P. G., & Methven, J. (2020). Is the subtropical jet shifting poleward?. *Climate Dynamics, 54*(3), 1741-1759.

Murakami, H. (2012). Future changes in tropical cyclone activity projected by the new high-resolution MRI-AGCM. *Journal of Climate, 25*(9), 3237-3260.

Ngo-Duc, T., Tangang, F. T., Santisirisomboon, J., Cruz, F., Trinh-Tuan, L., Nguyen-Xuan, T., ... & Gunawan, D. (2017). Performance evaluation of RegCM4 in simulating extreme rainfall and temperature indices over the CORDEX-Southeast Asia region. *International Journal of Climatology*, *37*(3), 1634-1647.

O'Neill, B. C., Tebaldi, C., Van Vuuren, D. P., Eyring, V., Friedlingstein, P., Hurtt, G., ... & Meehl, G. A. (2016). The scenario model intercomparison project (ScenarioMIP) for CMIP6.

Oh, S. G., Park, J. H., Lee, S. H., & Suh, M. S. (2014). Assessment of the RegCM4 over East Asia and future precipitation change adapted to the RCP scenarios. *Journal of Geophysical Research: Atmospheres*, *119*(6), 2913-2927.

Ono, K., & Kazama, S. (2011). Analysis of extreme daily rainfall in Southeast Asia with a gridded daily rainfall data set. *IAHS Publication*, *344*, 169-175.

Gan, B., Wu, L., Jia, F., Li, S., Cai, W., Nakamura, H., ... & Miller, A. J. (2017). On the response of the Aleutian low to greenhouse warming. *Journal of Climate*, *30*(10), 3907-3925.

Pall, P., Allen, M. R., & Stone, D. A. (2007). Testing the Clausius–Clapeyron constraint on changes in extreme precipitation under CO 2 warming. *Climate Dynamics*, *28*(4), 351-363.

Ploshay, J. J., & Lau, N. C. (2010). Simulation of the diurnal cycle in tropical rainfall and circulation during boreal summer with a high-resolution GCM. *Monthly Weather Review*, *138*(9), 3434-3453.

Polvani, L. M., D. W.Waugh, G. J. P.Correa, and S. W.Son, 2011: Stratospheric ozone depletion: The main driver of twentieth-century atmospheric circulation changes in the Southern Hemisphere. *J. Climate, 24*, 795–812

Rodwell, M. J., & Hoskins, B. J. (2001). Subtropical anticyclones and summer monsoons. *Journal of Climate, 14*(15), 3192-32

Rocheta, E., Evans, J. P., & Sharma, A. (2017). Can bias correction of regional

climate model lateral boundary conditions improve low-frequency rainfall variability?. *Journal of Climate, 30*(24), 9785-9806.

Ropelewski, C. F., & Halpert, M. S. (1987). Global and regional scale precipitation patterns associated with the El Niño/Southern Oscillation. *Monthly weather review*, *115*(8), 1606-1626.

Schroeer, K., & Kirchengast, G. (2018). Sensitivity of extreme precipitation to temperature: the variability of scaling factors from a regional to local perspective. *Climate dynamics*, *50*(11-12), 3981-3994.

Sooraj, K. P., Terray, P., & Mujumdar, M. (2015). Global warming and the weakening of the Asian summer monsoon circulation: assessments from the CMIP5 models. *Climate Dynamics*, *45*(1-2), 233-252.

Sui, C. H., Chung, P. H., & Li, T. (2007). Interannual and interdecadal variability of the summertime western North Pacific subtropical high. *Geophysical research letters, 34*(11).

Sutton, R. T., Dong, B., & Gregory, J. M. (2007). Land/sea warming ratio in response to climate change: IPCC AR4 model results and comparison with observations. *Geophysical Research Letters*, *34*(2).

Taylor, K. E. (2001). Summarizing multiple aspects of model performance in a single diagram. *Journal of Geophysical Research: Atmospheres*, *106*(D7), 7183-7192.

——, Stouffer, R. J., & Meehl, G. A. (2012). An overview of CMIP5 and the experiment design. *Bulletin of the American Meteorological Society*, *93*(4), 485-498.

Tao, F., Yokozawa, M., Zhang, Z., Hayashi, Y., Grassl, H., & Fu, C. (2004). Variability in climatology and agricultural production in China in association with the East Asian summer monsoon and El Niño Southern Oscillation. *Climate Research, 28*(1), 23-30.

Tebaldi, C., & Knutti, R. (2007). The use of the multi-model ensemble in probabilistic climate projections. *Philosophical transactions of the royal society A: mathematical, physical and engineering sciences*, *365*(1857), 2053-2075.

Trenberth, K. E. (2011). Changes in precipitation with climate change. *Climate Research*, *47*(1-2), 123-138.

Teutschbein, C., & Seibert, J. (2012). Bias correction of regional climate model

simulations for hydrological climate-change impact studies: Review and evaluation of different methods. *Journal of hydrology, 456*, 12-29.

Huffman, G. J., Bolvin, D. T., Nelkin, E. J., Wolff, D. B., Adler, R. F., Gu, G., ... & Stocker, E. F. (2007). The TRMM multisatellite precipitation analysis (TMPA): Quasi-global, multiyear, combined-sensor precipitation estimates at fine scales. *Journal of hydrometeorology*, *8*(1), 38-55.

Van Vuuren, D. P., Edmonds, J., Kainuma, M., Riahi, K., Thomson, A., Hibbard, K., ... & Masui, T. (2011). The representative concentration pathways: an overview. *Climatic change, 109*(1-2), 5.

Wai, M. M. K., Welsh, P. T., & Ma, W. M. (1996). Interaction of secondary circulations with the summer monsoon and diurnal rainfall over Hong Kong. *Boundary-Layer Meteorology*, *81*(2), 123-146.

Wang, B., & Fan, Z. (1999). Choice of South Asian summer monsoon indices. *Bulletin of the American Meteorological Society*, *80*(4), 629-638.

——, Wu, R., & Fu, X. (2000). Pacific–East Asian teleconnection: how does ENSO affect East Asian climate?. *Journal of Climate*, *13*(9), 1517-1536.

——, Wu, R., & Lau, K. M. (2001). Interannual variability of the Asian summer monsoon: Contrasts between the Indian and the western North Pacific–East Asian monsoons. *Journal of Climate, 14*(20), 4073-4090.

——, & LinHo (2002). Rainy season of the Asian–Pacific summer monsoon. *Journal of Climate*, *15*(4), 386-398.

——, Xiang, B., & Lee, J. Y. (2013). Subtropical high predictability establishes a promising way for monsoon and tropical storm predictions. *Proceedings of the National Academy of Sciences, 110*(8), 2718-2722.

Wang, L., & Chen, W. (2014). An intensity index for the East Asian winter monsoon. *Journal of Climate*, *27*(6), 2361-2374.

Wang, P., Tam, C. Y., & Xu, K. (2019). El Niño–East Asian monsoon teleconnection and its diversity in CMIP5 models. *Climate Dynamics*, *53*(9-10), 6417-6435.

Wang, Y., & Zhou, L. (2005). Observed trends in extreme precipitation events in China during 1961–2001 and the associated changes in large-scale circulation. *Geophysical Research Letters*, *32*(9).

Wilby, R. L., & Wigley, T. M. L. (1997). Downscaling general circulation model

output: a review of methods and limitations. *Progress in physical geography*, *21*(4), 530-548.

Wu, H., Zhai, P., & Chen, Y. (2016). A comprehensive classification of anomalous circulation patterns responsible for persistent precipitation extremes in South China. *Journal of Meteorological Research, 30*(4), 483-495.

Wu, R., Hu, Z. Z., & Kirtman, B. P. (2003). Evolution of ENSO-related rainfall anomalies in East Asia. *Journal of Climate*, *16*(22), 3742-3758.

Gao, X., Zhao, Z., & Giorgi, F. (2002). Changes of extreme events in regional climate simulations over East Asia. *Advances in atmospheric sciences*, *19*(5), 927-942.

Xu, M., Xu, H., & Ma, J. (2016). Responses of the East Asian winter monsoon to global warming in CMIP5 models. *International Journal of Climatology, 36*(5), 2139-2155.

Xu, Z., & Yang, Z. L. (2012). An improved dynamical downscaling method with GCM bias corrections and its validation with 30 years of climate simulations. *Journal of Climate, 25*(18), 6271-6286.

Xue, F., Dong, X., & Fan, F. (2018). Anomalous western Pacific subtropical high during El Niño developing summer in comparison with decaying summer. *Advances in Atmospheric Sciences, 35*(3), 360-367.

Yatagai, A., Kamiguchi, K., Arakawa, O., Hamada, A., Yasutomi, N., & Kitoh, A. (2012). APHRODITE: Constructing a long-term daily gridded precipitation dataset for Asia based on a dense network of rain gauges. *Bulletin of the American Meteorological Society*, *93*(9), 1401-1415.

Ying, M., Knutson, T. R., Kamahori, H., & Lee, T. C. (2012). Impacts of climate change on tropical cyclones in the western North Pacific basin. Part II: Late twenty-first century projections. *Tropical Cyclone Research and Review, 1*(2), 231-241.

Yuan, W. (2013). Diurnal cycles of precipitation over subtropical China in IPCC AR5 AMIP simulations. *Advances in Atmospheric Sciences*, *30*(6), 1679-1694.

Zeng, X., Zhao, M., & Dickinson, R. E. (1998). Intercomparison of bulk aerodynamic algorithms for the computation of sea surface fluxes using TOGA COARE and TAO data. *Journal of Climate*, *11*(10), 2628-2644.

Zhai, P., Zhang, X., Wan, H., & Pan, X. (2005). Trends in total precipitation and

frequency of daily precipitation extremes over China. *Journal of climate*, *18*(7), 1096-1108.

Zhang, L., Sielmann, F., Fraedrich, K., Zhu, X., & Zhi, X. (2015). Variability of winter extreme precipitation in Southeast China: contributions of SST anomalies. *Climate dynamics, 45*(9-10), 2557-2570.

Zhang, Q., Sun, P., Singh, V. P., & Chen, X. (2012). Spatial-temporal precipitation changes (1956–2000) and their implications for agriculture in China. *Global and Planetary Change*, *82*, 86-95.

Zhang, R., Li, T., Wen, M., & Liu, L. (2015). Role of intraseasonal oscillation in asymmetric impacts of El Niño and La Niña on the rainfall over southern China in boreal winter. *Climate dynamics, 45*(3-4), 559-567.

Zhang, X., & Cong, Z. (2014). Trends of precipitation intensity and frequency in hydrological regions of China from 1956 to 2005. *Global and Planetary Change*, *117*, 40-51.

Zhang, W., Jin, F. F., Zhao, J. X., Qi, L., & Ren, H. L. (2013). The possible influence of a nonconventional El Niño on the severe autumn drought of 2009 in Southwest China. *Journal of Climate, 26*(21), 8392-8405.

Zhao, T., & Yatagai, A. (2014). Evaluation of TRMM 3B42 product using a new gauge-based analysis of daily precipitation over China. *International Journal of Climatology, 34*(8), 2749-2762.

Zhou, T. J., & Yu, R. C. (2005). Atmospheric water vapor transport associated with typical anomalous summer rainfall patterns in China. *Journal of Geophysical Research: Atmospheres*, *110*(D8).